Development of crash box for automotive application

Mario Boreanaz

Supervisor:

Giovanni Belingardi

A Giulia, ai miei genitori e ai miei fratelli.

ACKNOWLEDGEMENTS

I would first like to thank my thesis advisors, Professor Belingardi Giovanni of Politecnico di Torino and Professor Luis Carlos Monteiro Sales of PUC-MG for helping me in the research and accompanying me in writing.

To all the colleagues in Fiat, in particular Eng. Ciro, Eng. Daniel and Eng. Evandro.

To all my friends, my girlfriend and my family for the support and understanding letting me finish this job.

ABSTRACT

With the continued growth in the number of cars in circulation, an increase in road accidents is inevitable. The discipline of automotive safety is concerned with the improvement of components design, equipment and all that is needed to increase the vehicle reliability and safety in order to minimize the consequences of traffic impacts. All the improvements in the crashworthiness can be done working on new geometric design or using innovative material for safety components and in this paper the first choice is carried out. In this work, in fact, is developed a new idea in the construction of the crash boxes that is a fundamental component in a car energy absorption. The usefulness of this component is appreciated in the low speed crashes, because it limits the breakage of other more expensive components. The target of this work is to find a new crash box geometry that guarantee a higher energy absorption with the same size of a traditional component. The new design is inspired by the origami theory in which the Japanese art is applied in the following engineering field building collapsible structures that allow to absorb more energy in a low speed impact.

Keywords: Automotive safety, vehicle frontal crash, crash absorption.

CONTENTS

NOMENCLATURE

AEB – Autonomous emergency breaking

AZT – Allianz Zentrum für Technik

CAD – Computer aided design

CAE – Computer aided engineering

CESVI – Centro de experimentação e segurança viária

CFE – crush force efficiency

DOF – Degree of freedom

DP – Dual phase

FEM – Finite element method

FMVSS – Federal Motor Vehicle Safety Standards

HSLA – High strength low alloy

IIHS – Insurance Institute for Highway Safety

ISTAT – Istituto Nazionale di Statistica

LSTC – Livermore Software Technology Corp

NCAP – New Car Assessment Program

NHTSA – National Highway Traffic Safety Administration

NIP – Number of integration point

NURBS – Non-uniform rational basis splines

OBD – Offset Deformable Barrier

RCAR – Research council for automobile repairs

SEA – specific energy absorption

LIST OF SYMBOLS

P_{cr} – Critical load

E – Young´s modulus or Elasticy modulus

I – Moment of inertia

P_m – Mean crushing force

σ_0 – Average flow stress

σ_u – Ultimate tensile strength

t – Thickness

$P_{\max}$ – Maximum crippling force

k_{p} – Crippling coefficient

v – Poisson´s ratio

R – Mean radius

θ – Initialization parameter or Rotation angle or dihedral angle

φ – Oblique hill angle

D – Diameter

l – Height

L – Total height

ε – Strain

σ – Stress

G – Shear modulus

τ – Shear stress

γ – Shear strain

J_2 – Second principal invariant

σ_e – Effective stress

$d\lambda$ – Proportional constant value

$\dot{\varepsilon}$ – Strain rate

m – Strain rate sensitivity

$D,\ q$ – Cowper and Symonds parameters

$v_1, v_2 -$ Particles velocity

$C_B -$ Wave propagation

$A_B, A_S -$ Bar and specimen cross section area

$\varepsilon_I,\ \varepsilon_R,\ \varepsilon_T -$ Incident, reflected and transmitted strain

$a -$ Acceleration

$m -$ Mass

$F -$ Force

$E_K -$ Kinetic energy

$E_P -$ Potential energy

$g -$ Gravity force

$\eta -$ Structural efficiency

$LU -$ Load uniformity coefficient

$x_p -$ Penetration

LIST OF FIGURES

LIST OF TABLES

1 – INTRODUCTION

Impact and crash events occur very often in daily life and when it comes to car, customers prefer to purchase a safe vehicle. Recently crashworthiness has received considerable public attention in fact it is usual to hear at the television fatal road accident between cars, buses, trains and so on. According to ISTAT data, in Italian roads last year 73836 accidents occurred where only 1507 were lethal, so only about 0,2% thanks to improvement of crashworthiness and internal and external security systems like airbag or autonomous emergency breaking (AEB).

Another study says that 75% of car accident happen at low speed so the goal of crashworthiness is of course to obtain an optimized vehicle structure that can absorb the crash energy by controlled vehicle deformations while maintaining adequate space; so the residual crash energy can be managed by the restraint systems to minimize crash loads transfer to the vehicle occupants but also to reduce repair costs.

With the development of information and the possibility to read articles about safety in every specialist car magazine, everyone knows what the Euro NCAP are and why their own auto should have 5 stars. NCAP stands for The New Car Assessment Program and was instituted in 1979 by the U.S. National Highway Traffic Safety Administration and nowadays it's a standard on vehicle safety ratings. There isn't a single NCAP, but through the years many programs were developed around the world according with the *globalncap.org*: Europe (EuroNCAP), Australia (ANCAP), Japan (JNCAP), China (CNCAP), Korea (KNCAP) and most recently Latin America (LatinNCAP) and Southeast Asia (AseanNCAP). In the United States of America, Federal Motor Vehicle Safety Standards (FMVSS) requires a minimum value on IIHS (Insurance Institute for Highway Safety) and NHTSA (National Highway Traffic Safety Administration) tests. By now every car must undergo to a lot of safety tests and then can be suitable for the circulation and these tests are slightly different according to the state in question.

It need to analyze the LatinNCAP that has a vehicle rating scale of six levels (zero to five) both for child and adult protection; all these data are taken from the LatinNCAP website. The most important test is the Offset Deformable Barrier (ODB) because frontal impacts are the main responsible for death and serious injury than any other accident.

The car is driven at 64 km/h and crash against a deformable barrier with a 40% of overlap

because the most common type of accident involves just a part of the vehicle. This test represents a crash between two cars of the same weight at a constant speed of 50 km/h. As can be seen in the following figure, this crash test is done with two frontal impact dummies that represent the average adult male and with two children of 18 months and 3 years old on the rear seats.

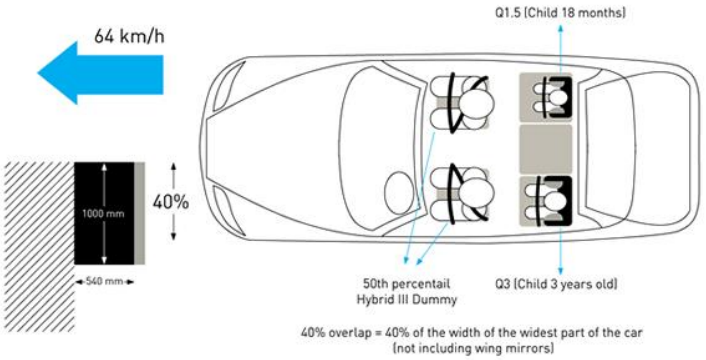

Figure 1 – ODB test

Source: latinncap.com.

The second highest frequency of serious accidents it's caused by side impact and there are two kinds of test. First there is a test with a Side Mobile Barrier that crashes at a velocity of 50 km/h into the side of a stationary car and second there is another side impact with the vehicle collision at 29 km/h against a rigid pole. According to the Research council for automobile repairs (RCAR), an important test to evaluate the vehicle damageability and reparability is the so called AZT test or Cesvi in Latin America. The test consists of a car impact against a rigid barrier with an inclination of 10 degrees and an offset (U in *Figure 2*) of 40 % and a low speed impact of 16 km/h. In this test, it's appreciate the crash box ability to absorb energy avoiding the deformation of more expensive parts like rails and so on.

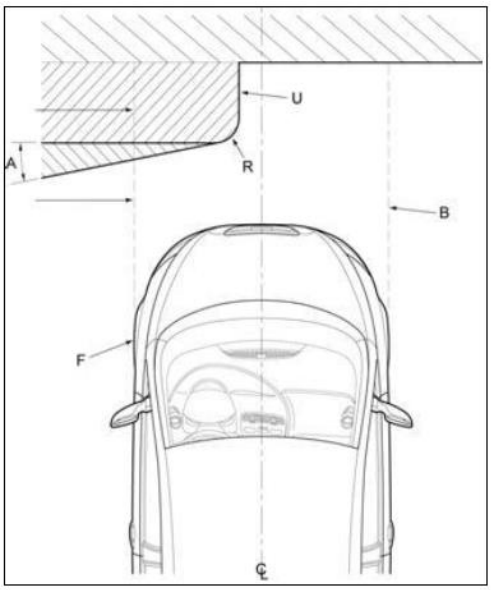

Figure 2 – AZT test

Source: Rcar.org, 2011.

There are a lot of other safety tests for example as pedestrian protection, child occupant protection and safety assist but, since it should improve the crash box energy absorption, the most appropriate and interesting test for this thesis is the AZT test.

According to this brief summary of the Latin NCAP and knowing the importance of the result and the rating of these tests, all the automotive companies have paid close attention to the safety of their cars. On the other hand, the market demands to the companies to do cars smaller and smaller, with a front end shorter and more attractive. To connect these two requests, always maintaining high security standards, companies are forced to use new technologies for maximize energy absorption in case of crash.

In this thesis, a new methodology of doing the crash box, that is one of the main drivers of shock absorption as will be seen later, will be explained. First of all, it has to be known what the crash box is: it's a thin-walled structure attached between the vehicle bumper structure and the side rail. The side rail is connected to the vehicle body and cannot be deformed too much for maintaining the passengers' safety. The determination of the crash box geometry is quite important to absorb the impact energy, since the installation space of the crash box is not very large. As written before, to reduce repair costs, an energy absorbing device such as the crash box is usually installed.

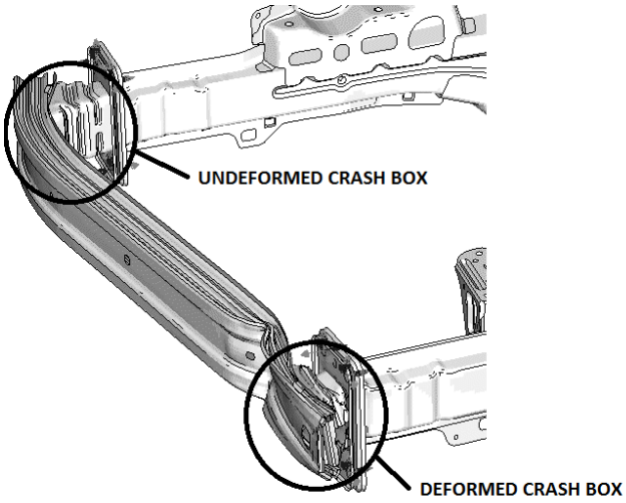

Figure 3 – Crash box structures

Source: Morello, Rossini, Pia and Tonoli, 2011.

Recently, it has been strictly required to satisfy both reduction of body weight and improvement of crash worthiness and so, regarding crash box, it is required to guarantee high energy absorption using sheet as thin as possible.

Belingardi and Avalle (2004) talked about that most of crash box structures are made of deep-drawing steels that don't have high characteristics. In the future, companies will probably use steels with high-strength or aluminum alloys, magnesium alloys or polymeric and composite materials. The introduction of these new materials has many problems like: their properties are not fully known, sometimes don't behave as expected because there is not a great experimentation of these materials and finally the cost that is not yet sustainable for mass production. So, considering that working on materials is a long process, it is thought to modify the geometry of crash box to increase the energy absorption with a common material.

1.1 Origami theory

Anyone when hear the word "origami", thinks about the ancient Japanese art of paper folding, but there are a lot of mathematic studies behind the origami's fold. This technique is used in different fields like aerospace, medicine and in automotive engineering. Conventional crash boxes are made of square tubes, as can been seen from *Figure 4*, instead of an origami beam that has a series of pre-folded used to modify the surface.

The basic idea of Origami Theory is to obtain super folding element during a crash that give

better energy absorption to conventional square tube. As will be seen in the next chapters, it is difficult to obtain the same collapse mode of the specimen.

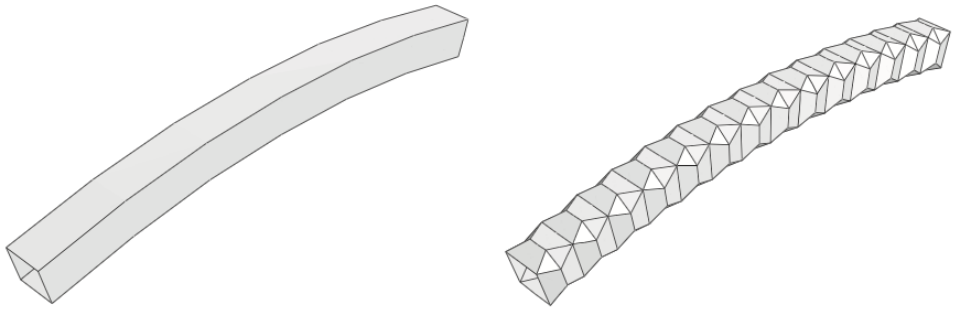

Figure 4 – Difference between conventional and origami beam

Source: Ma and You, 2013.

The reason of this innovative study is that origami patterns applied on thin-walled tubes offer two big advantages: the initial peak force can be reduced and may be controlled and these tubes present less fluctuation in the force during crushing.

1.2 Target

The aim of this thesis is to clarify the advantages and the limitations of the innovative origami theory. To do this, will be done a study of different shapes changing the geometrical parameters, different modules of crash boxes. The study will be first virtual with a finite element method that can give a performance comparison with the different geometry of the crash boxes and then the results will be validated with experimental analysis. A finite element method (FEM) is very useful because allows to do fast simulations and is much cheaper than the realization of the physical specimen.

At the end of this thesis project, will be known the design features of the origami crash can like an optimal element geometry, the manufacturing process to build these particular crash boxes and the best behaviour in case of crash.

1.3 State of the art

In this section are presented a list of book and publications which led to a development of the crashworthiness.

First studies on rectangular tubes were made by Wierzbicki and Abramowicz (1983) and they analyzed the crushing of thin-walled determining an expression for the mean crushing force but the model underestimates this force.

Abramowicz and Jones (1984) revisited the theory and they focused the attention on the effective crushing distance that led to higher mean crushing force.

Abramowicz and Jones (1986) investigated the extensional crushing mode of the rectangular tube with a study on the mixed crushing modes of a square tube. They presented a series of over 120 axial crushing tests under static and dynamic load.

Norman Jones (1989) published a milestone in books about the crash, Structural Impact, that sums up the theory and experimental trials made until that period. Then Abramowicz and Wierzbicki considered tubes with other cross-sectional shapes. They did static crush tests on square, hexagonal, and rhomboidal thin-walled columns and tried to predict the mean crushing force and collapse mode of these multi-corner prismatic structures.

Belingardi, Avalle, Vadori, Drazetic and Markiewicz (1994) analyzed the multi-cell section of crash box. The researchers made many software simulation and then experimental crash tests, obtaining a big increase in the structural efficiency compared to the traditional crash boxes.

Langseth (1996) studied the dynamic response of the square tube under different impact mass and velocity. He did tests on square aluminum extrusions in alloy AA6060 tempers T4 and T6 and used a numerical model (LS-DYNA).

Singace and El-Sobky (1997) introduced pattern on thin-walled tube in order to alter the crushing mode. They used corrugations on the PVC tubes to force the plastic deformation so that can take place at predetermined intervals along the tube generator. The aims are to predict and control the collapse mode in each fold to maximize the energy absorption.

Avalle, Chiandussi and Belingardi (2002) used a multipoint optimization called OPTISTAT in order to find the best configuration of corrugated tube.

Rossi (2005) made a numerical comparison in the crushing behavior among square, hexagonal and octagonal tubes subject to dynamic impact.

Belingardi, Goglio and Rossetto (2005) studied the influence of structural adhesives instead of

using spot welding technique for the production of built-up beams. They proposed an experimental analysis of four cross sections with different joint design and the result is that, using simpler designs than those used for the spot welding, adhesives are a good option also in term of energy absorption.

Tasdemirci (2008) investigated the effect of end constraining condition on the crushing behavior of circular tube. His study determines experimentally and numerically the effects of various end-conditions on the deformation mode, load displacement and average load displacement curves of short aluminum tubes deforming in concertina mode of deformation in free-constraint condition.

DiPaolo and Tom (2006) did quasi-static test using width grooves for collapse initiators; the materials have been used are ASTM A36 and A513 plain low-carbon steel and AISI 304 and 316 austenitic stainless steel. The results demonstrate the ability to limit symmetric axial crush mode response to a specific configuration and ensure repeatable load magnitudes.

Zhang (2007) proposed crushing of square tubes with two patterns constructed using the pyramid elements, whose absorbed energy increased by 15–33% and 54–93%, respectively.

Zhang and Huh (2009) investigated the axial crushing of square tubes longitudinally grooved. Their results showed that the energy absorption increased by up to 92% and the peak force was reduced by up to 22%, compared with the conventional square tubes.

Tarlochan (2013) studied thin walled under oblique loads; these conditions may cause bending mode and so can led to a lower energy absorption capability.

Zhou, Wang Ma and You (2016) did many tests on origami crash box and they achieved that complete diamond collapse mode has high performance than the collapse of conventional square tube. Unfortunately, the study showed that complete diamond mode occurred in few tests because the right collapse is high sensitive to geometric imperfections.

2 – LITERATURE REVIEW

In this chapter are presented a series of books, previous work and publication that made possible the development of this thesis. In the first paragraph, there is the explanation of the key point in the mechanical behaviour of materials, then is presented an introduction of the axial crash of circular and square tube because mainly all the crash boxes have these sections and after that are shown most common improvements on the thin walled geometry. After that, is proposed a description of the front structure configuration in order to understand why the crash box is so important for the crashworthiness. In the last paragraph, there is the definition of the origami theory with the most common use in engineering until now and a series of work of thin walled origami that describe the potential of these innovative structure.

2.1 Mechanical properties

The main topic behind an axial impact is the deformation of the specimens which can be elastic or much more interesting to absorb shocks, can occur a plastic deformation.

2.1.1 Elastic deformation

Starting from the basics of elasticity, Hosford (2005) explain that the elastic deformation is reversible and so applying a force on a body, this body may deform temporarily but when the force is removed, the body returns to its original shape.
Considering an isotropic material, that means having the same properties on the three directions, the stress-strain behavior is proportional through this relationship:

$$\varepsilon_x = \frac{\sigma_x}{E} \tag{1}$$

where ε_x is the strain in x direction, σ_x is the tension in x direction and E is the Young's modulus; the formula is also known as Hooke's law. The uniaxial load causes a deformation in the other two directions equal to:

$$\varepsilon_y = \varepsilon_z = -v\varepsilon_x \tag{2}$$

where v is the Poisson's ratio. Combining the equations (1) and (2) is obtained the general Hooke's law that considers the Poisson shrinkage:

$$\varepsilon_x = \frac{1}{E}[\sigma_x - v(\sigma_y + \sigma_z)] \tag{3}$$

The equation (3) is also written for the y and z direction. Another elastic behavior is obtained with the shear or torsional stress:

$$\tau = G\gamma \tag{4}$$

where τ and γ are shear stress and strain respectively and G is the shear modulus.

It is possible to get this proportional behavior of the material only if the proportional limit is not exceeded. As can be seen in *Figure 5(a)*, before the point P the material remains in the elastic section of the curve.

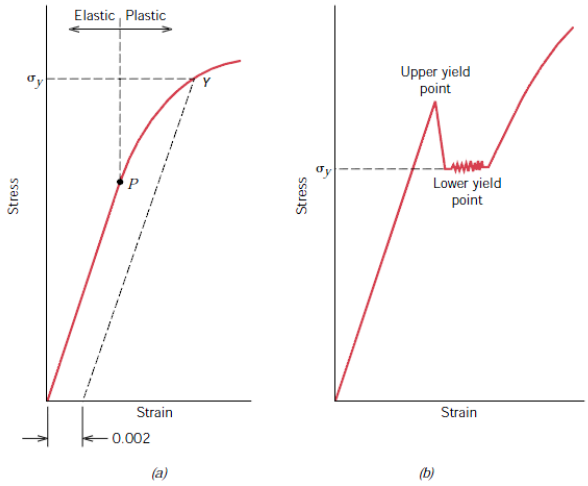

Figure 5 – Stress and strain curve

Source: Callister, 2001.

Unfortunately, it's quite difficult to find a precise value of the proportional limit and there is not a drastic shift between the elastic and plastic behavior, so the experience has led to use a point Y in which for most of the materials the yield phenomenon occurs. Introducing an offset on the abscissa usually of 0.002, drawing a parallel line to the elastic curve, is possible to obtain the yield point in the intersection of the stress-strain curve and this line. The value corresponding to the ordinate of the point is the yield stress in which is presented a small amount of plastic deformation but for engineering purpose is widely used. There are many materials with a stress-strain curve *(b)* in which there is a clear transition between elastic and plastic behavior.

2.1.2 Plastic deformation

In a crash simulation, where it is studied the yield under complex load and in which there are many nonlinearities and the elastic theory is no longer valid, every software uses the plasticity theory to predict the deformation of the materials.

Before starting with the description of the theory, is useful to know the difference between the true stress-strain curve instead of the engineering curve and why is more meaningful for this kind of study. According to Deiter (1988), the engineering stress-strain curve doesn't consider the changing of the specimens' dimension in fact as presented in the equation (5) and (6), consider only the initial dimensions.

$$\varepsilon_{eng} = \frac{\Delta L}{L_0} \tag{5}$$

$$\sigma_{eng} = \frac{F}{A_0} \tag{6}$$

Where L_0 is the original length and A_0 is the initial area.

$$\varepsilon_t = ln\frac{L}{L_0} = \ln(\varepsilon_{eng} + 1) \tag{7}$$

$$\sigma_t = \frac{F}{A} = \sigma_{eng}(\varepsilon_{eng} + 1) \tag{8}$$

In the formulas (7) and (8) are considered the load and the area in each instant and so the specimen reduction during the plastic deformation and there is also the link between the true and

the engineering value both for stress and strain. In *Figure 6* there is the comparison between the curves.

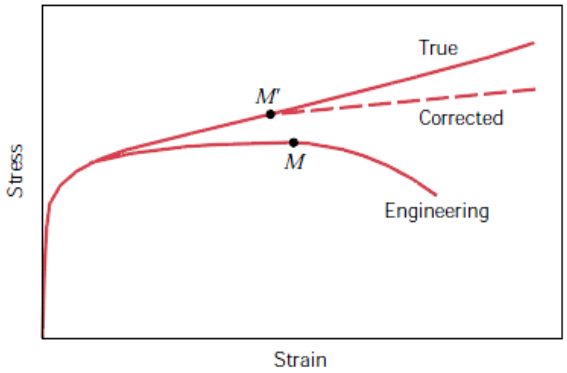

Figure 6 – Engineering vs true curve

Source: Callister, 2001.

There is also a new curve called "corrected" that present a different plot after the *M* point to consider the necking phenomenon. This true curve is useful also because when it's necessary to import a material curve on the software, LS-DYNA needs the true stress and strain. The true stress-strain curve is commonly called flow curve and the expression (9) called also Hollomon law, gives the mathematic equation on the plasticity curve that is applicable from the beginning of plastic deformation until the maximum load the produce necking on the specimen.

$$\sigma = K\varepsilon^n \tag{9}$$

Where K is the stress at the unit deformation and n is the so-called strain-hardening coefficient; these two coefficients vary for every alloy. To obtain the flow curve, some simplifications have been made like neglecting the Bauschinger effect and the initial elastic deformation. The Bauschinger effect describe the material hysteresis behavior but usually it's admitted an equal yield stress for tension and compression; the other simplifications are to consider the material behavior like perfectly rigid without the elastic deformation below the yield stress and then during the plasticity the stress cannot be higher than the yield stress, this is called a perfectly rigid-plastic material.

The base of plasticity theory is the yield criterion which is the mathematical formulation that summarized the stress states that generate the plastic flow. According to Hosford (2005), the general expression of the yield criterion is shown in the (10):

$$f(\sigma_x, \sigma_y, \sigma_z, \tau_{yz}, \tau_{zx}, \tau_{xy}) = C \tag{10}$$

$$f(\sigma_1, \sigma_2, \sigma_3) = C \tag{11}$$

where C is a material constant. The equation (11) is the simplified expression for isotropic material in which can be used only the principal stresses and the *Figure 7* presents the yield surface in the stress plane.

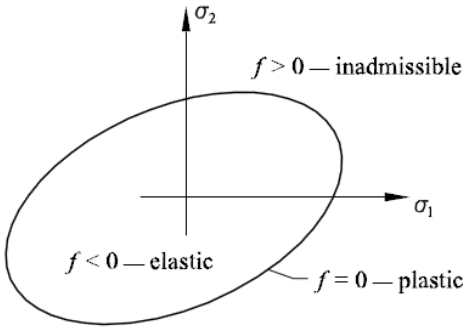

Figure 7 – Yield surface

Source: Krabbenhøft, 2002.

It is easy to understand that the plastic flow can occur only when a material stands on the curve f=0, otherwise inside the curve there is an elastic deformation. In *Figure 8*, are proposed two modifications on the curves to take into account the strain-hardening and in the paragraph 2.1.3 will be proposed other variations.

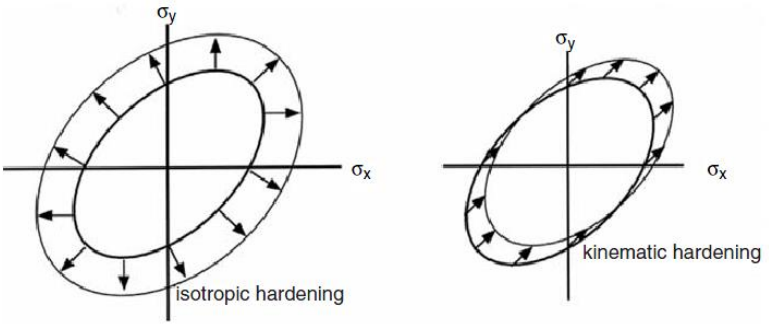

Figure 8 – Hardening rules

Source: Hosford, 2005.

The left-hand image presents an isotropic hardening that expand the curve on the same amount in every direction that is not realistic and the kinematic hardening criterion on the right apply a translation of the curve in the loading direction. The most famous criteria have been proposed by Tresca and Von Mises. Starting with Tresca, the plastic deformation occurs when the shear stress reaches a maximum value:

$$\tau_{max} = \max\left(\left|\frac{\sigma_1-\sigma_2}{2}\right|, \left|\frac{\sigma_2-\sigma_3}{2}\right|, \left|\frac{\sigma_3-\sigma_1}{2}\right|\right) = k \tag{12}$$

$$\frac{1}{2}\,\sigma_1 = k \tag{13}$$

The equation 13, represent the limit condition AB (*Figure 9*) for the Tresca criterion in the stress plane with a null value of σ_3. The same limit can be found for the other tension σ_2 and with the negative values and finally the yield criterion became a sort of hexagon.

Von Mises criterion is more often used both because is more accurate and Tresca criterion is a too cautelative method. The Yield function is:

$$f(J_2) = \sqrt{J_2} - \sigma_e \tag{14}$$

where J_2 is the second principal invariant that plays an important role in continuum mechanics and the σ_e is the effective stress that is calculated by this equation:

$$\sigma_e = (\tau_{12}^2 + \tau_{23}^2 + \tau_{31}^2)^{\frac{1}{2}}$$
$$= \left[\frac{1}{2}(\sigma_1 - \sigma_2)^2 + \frac{1}{2}(\sigma_2 - \sigma_3)^2 + \frac{1}{2}(\sigma_3 - \sigma_1)^2\right]^{\frac{1}{2}} \quad (15)$$

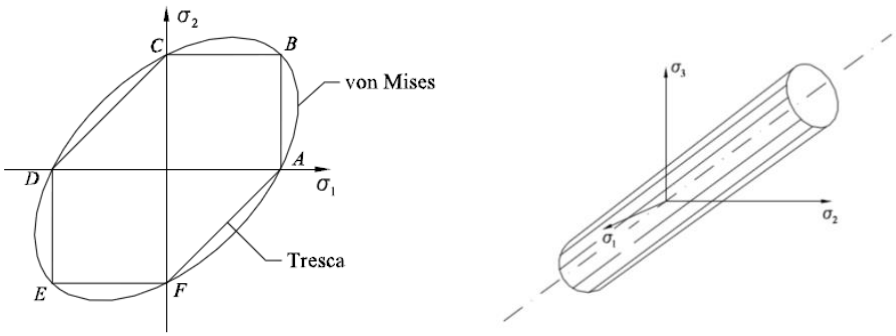

Figure 9 – Yield surface for Tresca and Von Mises and Von Mises criterion in the stress space

Source: Krabbenhøft, 2002.

The results of this theory are summarized in *Figure 9* where are presented the difference between the Tresca and the Von Mises surface and, on the right, there is also plotted the Yield surface for Von Mises theory in the principal stress space.

After the stress description, it has to consider the total strain with a famous law called Prand-Reuss proposed in these equations:

$$d\varepsilon^{tot} = d\varepsilon^e + d\varepsilon^p \quad (16)$$

$$d\varepsilon^p = d\lambda \frac{dg}{d\sigma} = d\lambda \nabla g \quad (17)$$

where in the equation (25) is presented the increment of total strain like a sum of elastic strain already seen with the Hooke's law and plastic strain. The Plastic strain as shown in *Figure 10*, is proportional to a scalar constant value $d\lambda$ that is a function of the stress-strain curve and g is the yield function chosen according to the criterion.

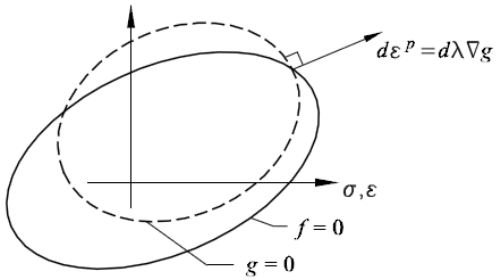

Figure 10 – Strain increment

Source: Krabbenhøft, 2002.

This law states that the plastic deformation will be proportional to the normal vector of the yield surface and therefore is proportional to the deviatoric stress.

2.1.3 Strain rate sensitivity

An important factor to consider is the effect of the strain rate and temperature on the material's mechanical behavior. The strain rate is defined by the equation:

$$\dot{\varepsilon} = \frac{d\varepsilon}{dt} = \frac{d\left[\ln\frac{(L - L_0)}{L_0}\right]}{dt} = \frac{1}{L}\frac{dL}{dt} = \frac{v}{L} \tag{18}$$

where v is the crosshead velocity of the testing machine and usually the strain rate is expressed in unit s^{-1}. The general law that links the flow stress and the strain rate is:

$$\sigma = C(\dot{\varepsilon})^m|_{\varepsilon,T} \tag{19}$$

where C is a constant and m is the strain rate sensitivity coefficient that changes for every material. The law is valid for a certain strain and a certain temperature. The exponent m is calculated by:

$$m = \frac{\ln\left(\frac{\sigma_2}{\sigma_1}\right)}{\ln\left(\frac{\dot{\varepsilon}_2}{\dot{\varepsilon}_1}\right)} \tag{20}$$

The effect of the rate sensitivity is not so accentuated at room temperature, but most of metals have a high increase of the *m* exponent, raising the temperature (*Figure 11)*.

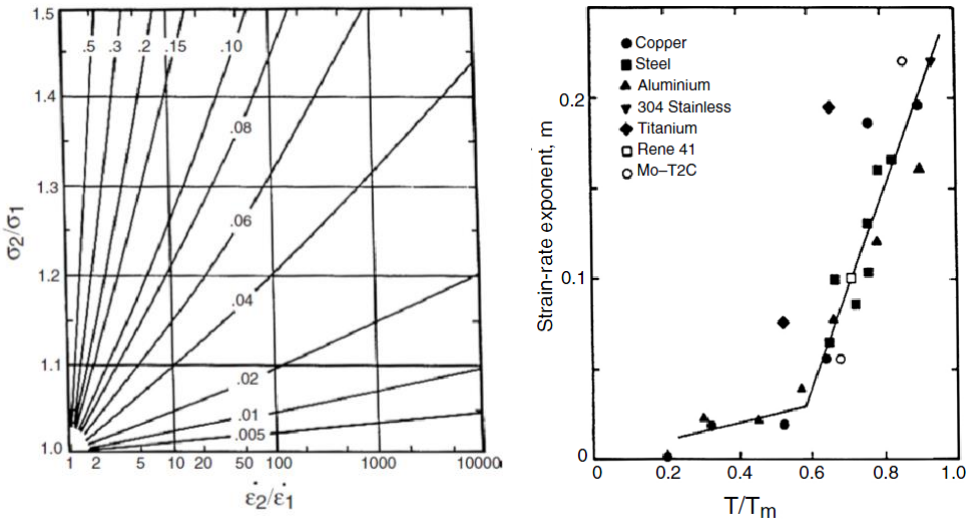

Figure 11 – Strain rate sensitivity and temperature effect

Source: Hosford, 2005.

Hosford (2005), presents how much the plastic flow of mild steel is dependent of the strain rate with different value of *m*. In the right-hand side, there is the correlation between the temperature and the strain rate exponent and is possible to underline the high increase of *m* when the half of melting point T_m value is reached. According to Jones [31], many researchers proposed constitutive equations in order to describe the strain rate sensitivity behavior but considering different references the results are quite contrasting. Cowper and Symonds (1957) suggested the constitutive equation:

$$\dot{\varepsilon} = D\left(\frac{\sigma_0'}{\sigma_0} - 1\right)^q, \qquad \sigma_0' \geq \sigma_0 \tag{21}$$

where σ_0' is the dynamic flow stress and D and q are constant that change for all the materials; Cowpers and Symonds made many tests in order to classify these constants for mild steel, aluminum alloy, stainless steel high tensile steel and titanium alloys. According to the Cowper and Symonds constitutive equation, for a mild steel D and q coefficients should have a value of

6844 s^{-1} and 3,91 respectively but, with some experimental tests, Abramowicz and Jones (1986) for a square tube with a mild steel found these results: D=802 s^{-1} and q=3,585.

2.1.4 Tests for material characterization

In every engineering application is very important to know the material properties to predict the behavior under load and, in the case of this thesis, to guarantee safety following the deformation expected by the designer. The most common analysis is called tensile test and is carried out with a standard specimen as in *Figure 12.*

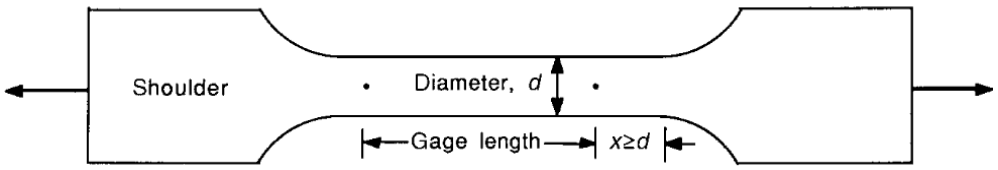

Figure 12 – Tensile test specimen

Source: www.asminternational.org, 2004.

In the image is possible to see the specimen's shape with two shoulders on the side and a gage with a lower cross section compared to that of the shoulders; this is done in order to obtain the deformation in the gage section and also to facilitate the gripping operations. The gage should have a longer length than diameter, usually x is four times d. Mounting a specimen like that on a machine that measure the variation of force during the model deformation, it's obtained the engineering stress-strain curve presented before in *Figure 6.* There are also other tests like compression test to avoid the necking that occur in the tensile test; compression tests are also used to obtain a better flow curve at high strains. With these tests is possible to obtain also a true stress-strain curve using the (7) and (8) equations, but the big limitation of the tensile test is the strain rate. As seen before, for common steels the strain rate is a very important factor and with today's machine and technology the maximum strain rate achievable is 10^2 s^{-1}. For impact event like a crash vehicle and the other applications that involve the deformation under high velocity, the tensile test cannot give accurate results. Chen and Song (2010) state that for high strain rate like from 10^2 s^{-1} until 10^4 s^{-1} can be performed a hummer-blowing condition with a common

machine but there are two main problems: with a hummer impact, it is difficult to obtain detailed and reliable data and it's not possible to control the specimen's condition.
In the 1949, Kolsky proposed an innovative method to overcome these problems, the test is called Hopkinson bar and is schematized in *Figure 13*.

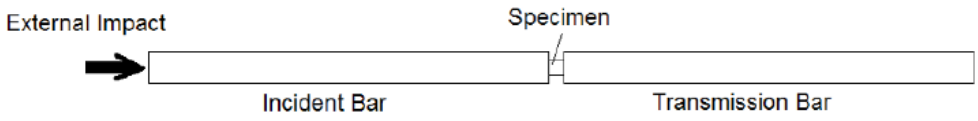

Figure 13 – Hopkinson bar

Source: Chen, Song, 2010.

The basic idea is to avoid the direct impact on the specimen using two elastic rods called incident bar and transmission bar or input and output bar. The incident bar is hit by an explosion like a hummer stroke that produces a compressive stress wave that propagates in the incident bar and comes to the specimen. In *Figure 14* is possible to underline the stress wave reflected by the specimen and the other part transmitted to the specimen and to the output bar.

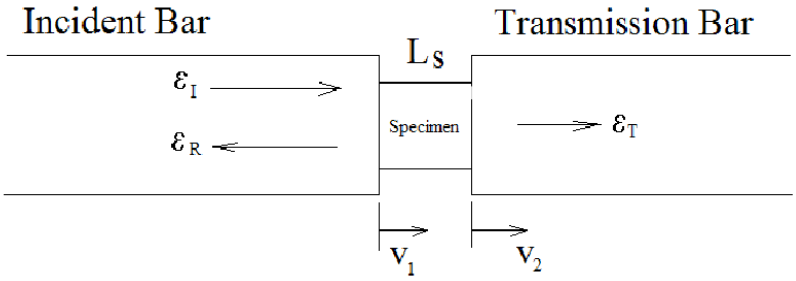

Figure 14 – Strain subdivision

Source: Chen, Song, 2010.

Assuming a perfect wave propagation without dissipation in both bars, is possible to evaluate the particle velocity on the specimen's side:

$$v_1 = C_B\,(\varepsilon_I - \varepsilon_R) \tag{22}$$

$$v_2 = C_B\,\varepsilon_T \tag{23}$$

where C_B is the wave propagation speed on the bar and *I*, *R* and *T* stand for incident, reflected and transmitted respectively. With the following equation it's possible to evaluate the engineering strain on the specimen subtracting the reflected and the transmitted part to the total incident strain:

$$\varepsilon = \frac{v_1 - v_2}{L_S} = \frac{C_B}{L_S}(\varepsilon_I - \varepsilon_R - \varepsilon_T) \tag{24}$$

where L_S is the initial length of the specimen. The engineering stresses are calculated with:

$$\sigma_1 = \frac{A_B}{A_S} E_B(\varepsilon_I + \varepsilon_R) \tag{25}$$

$$\sigma_2 = \frac{A_B}{A_S} E_B \varepsilon_T \tag{26}$$

where E_B is the Young's modulus of the bar, A_B is the bar cross section area and A_S is the specimen cross section area. In a laboratory with this instrumentation it's possible to change the impact velocity and the specimen's size in order to obtain the stress-strain curves at different strain rates and so is widely used in the material engineering characterization.

2.2 Axial crushing of thin walled tubes

First the study is focused on thin walled structure because of the high capability to absorb the kinetic energy in an impact event and to convert this energy in strain energy by irreversible plastic deformation described in the previous paragraph. A very important analysis in axial crash consists of determining the maximum load a column can support before it collapses. For long columns, the collapse is not a function of material yield, but it is instead governed by the column's stiffness, both material and geometric.

$$P_{cr} = \frac{\pi^2 EI}{L^2} \tag{27}$$

The equation (27) is the classical Euler buckling theory result where E is the Young's modulus, I is the moment of inertia of the cross section and L is the length of the column. It gives the critical value of load, called P_{cr}, above which the column will buckle.

So initially a compression tube undergoes collapse that can be elastic due to geometric instability (buckling) or plastic due to the material and a maximum collapse force is developed. After that, in a stable deformation mode, there is the mostly part of energy absorption because the tube will continue to deform axially, creating lobes that deform according to the mechanisms that will be discussed later. At this stage, called the permanent regime, the force developed by the tube is a function of the formation of a new lobe followed by the compaction of these. This force tends to vary less and the average of the peaks of force, between the formation and compaction of a new lobe, is called mean force.

The researchers began by modeling the mechanics and kinematics of the folding process and they tried to find a crush characteristic that involved simple relationships between component geometry and material properties. Wierzbicki and Abramowicz, using kinematics plasticity, developed a theory of crushing behavior of thin wall and found the expression for the mean crush load (28) solving an energy balance for a square tube. They equated the external work done by the crush load with energies dissipated in different types of deformation mechanisms as they occur in a folding process.

$$P_m = 9.56\sigma_0 t^{\frac{5}{3}} b^{\frac{1}{3}} \tag{28}$$

Where σ_0 is the average flow stress that is $(0.9–0.95)\sigma_u$ and σ_u is the ultimate tensile strength of material, t is the thickness and b is the width of the tube.

Then another two researches, Mahmood and Paluszny, understood that collapse strength of the section is related to thickness/width (t/b) ratio and material properties. For small t/b ratio, they found the so called *non-compact* sections that are large irregular folds, which create a bending instability that is induced by fold irregularities. For larger t/b ratio, the influence of geometry is less predominant and the material strength property governs the collapse mode and so they obtained the post-buckling stability.

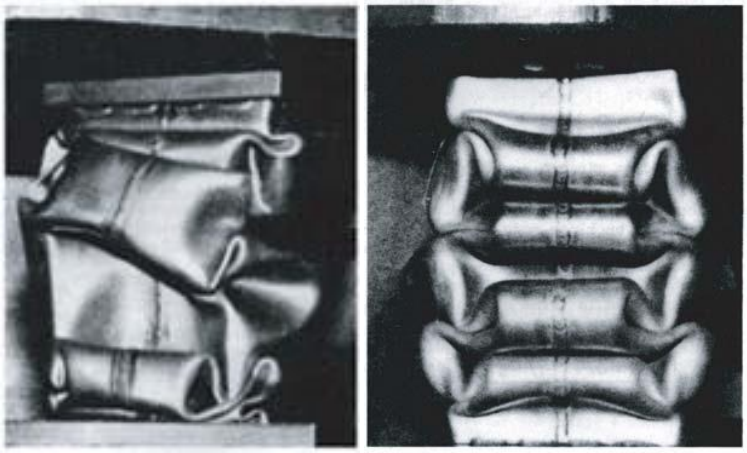

Figure 15 – Compact vs non-compact sections

Source: Du Bois et al., 2000.

The threshold of stability collapse mode is given by the equation (29):

$$\frac{t}{b} < 0.48\left[\frac{\sigma_y(1-v^2)}{E}\right]^{\frac{1}{2}} \tag{29}$$

where *E* is the Young's modulus as seen before and *v* is the Poisson's ratio.

Starting for example with a thin walled of $t/b<0.08$ they achieved the formulation of the maximum crippling force of a rectangular tube (30):

$$P_{max} = 2\left[\frac{k_p E}{\beta(1-v^2)}\right]^{0.43} t^{1.86} b^{0.14}(1-\alpha)\sigma_y^{0.57} \tag{30}$$

where $k_p$is the crippling coefficient that is a function of aspect ratio $\alpha=d/b$ (*Figure 16*) where *d* is the smaller and *b* is the larger side of the cross section. As can be seen in *Figure 17, β* is factor that depends on the thickness ratio and the ultimate stress of the material.

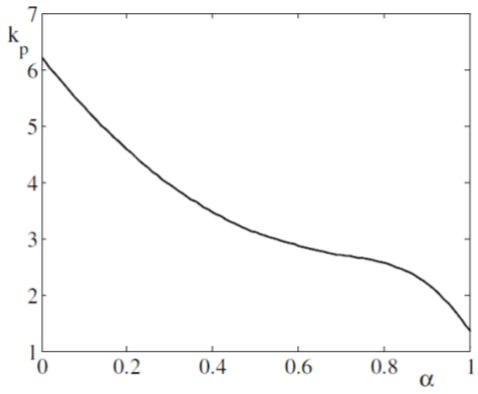

Figure 16 – Crippling coefficient

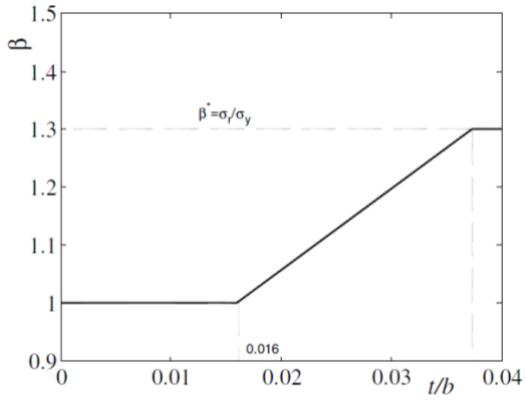

Figure 17 – The factor β

Source: Morello, Rossini, Pia and Tonoli, 2011.

A very common representation of the axial crushing history, is the force-displacement characteristic that highlights the most important points like maximum load capacity and mean crushing force. The *Figure 17*, presents also a comparison between a stable crushing deformation that obviously is idealized and an instable deformation if the $P_{\max\_stable}$ is exceeded.

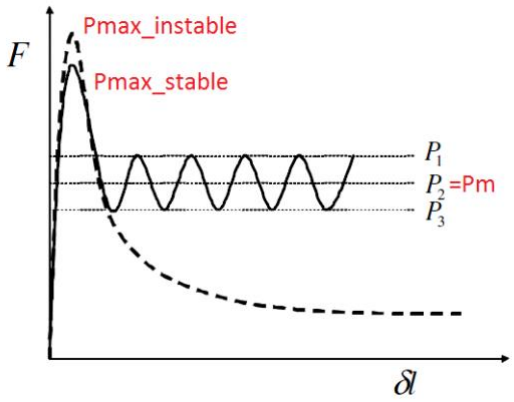

Figure 18 – Force-displacement curve

Source: Morello, Rossini, Pia and Tonoli, 2011.

The area below the curve is the energy absorbed that is easy to calculate doing the integral of the curve and so it is a useful and quick tool for structural designers.

Another two important parameters for a crash box design are the crush force efficiency (*CFE*) that is the ratio between the maximum initial force and the mean crushing force that in an ideal case the ratio is one and the specific energy absorption (*SEA*) that is the value of energy absorbed divided by the mass of the crushed material. According to Belingardi et al. [14], other useful

parameters to describe the crashing behavior introducing the yield are η, θ and LU. The first parameter is called structural efficiency and represents the ratio between the mean force and the yield force. The second is the initialization parameter that represents the effort to initialize the collapse and is defined with the ratio of the maximum force over the yield force. The LU parameter has the same definition of *CFE* in fact compares the maximum and the mean force but it's often used this formulation because it comes directly from the ratio of θ over η. This load uniformity parameter expresses the regularity of the energy absorption and more this ratio approaches to unit value, better is the energy absorption.

Jones [31] presented the progressive buckling of thin walled square tube and says that there are basically two possible collapse modes. In *Figure 19*, the case *a* represent the so called inextensional deformation mode in fact when the segment AC decreases, the other segment CD increases and so the length ACD remains a constant value during the crushing event.

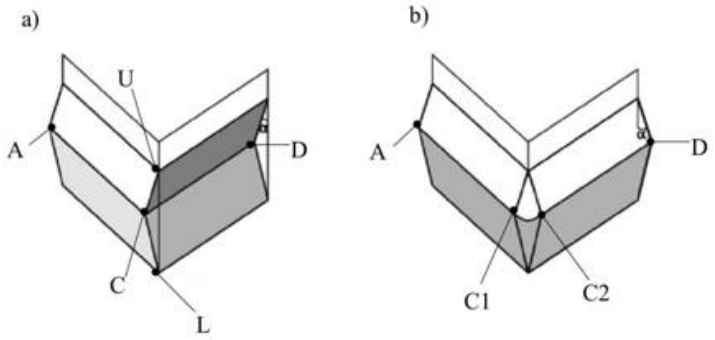

Figure 19 – Collapse mode

Source: Morello, Rossini, Pia and Tonoli, 2011.

The other case is the extensional mode because the surface AC1C2D during the plastic deformation. In the inextensional mode, the plastic deformation is caused by the movement to the left of the plastic hinge UCL. This movement generates a high bending on the plate that is bended first in a direction and then in the opposite direction and so each portion of the material is submitted to a plastic extension and then a compression.

The model presented before considers the deformation of a surface at mid thickness as negligible, but a more accurate analysis is showed in *Figure 20* where the layer ACD is deformed like the toroidal surface on the left-hand side of the image. So, there is an extensional deformation in the inextensional mode if it's take into account the thickness of the plate. This deformation of a

corner line is called super folding element and represents a piece of the prismatic beam which originates a single plastic fold as it shown in the right-hand side.

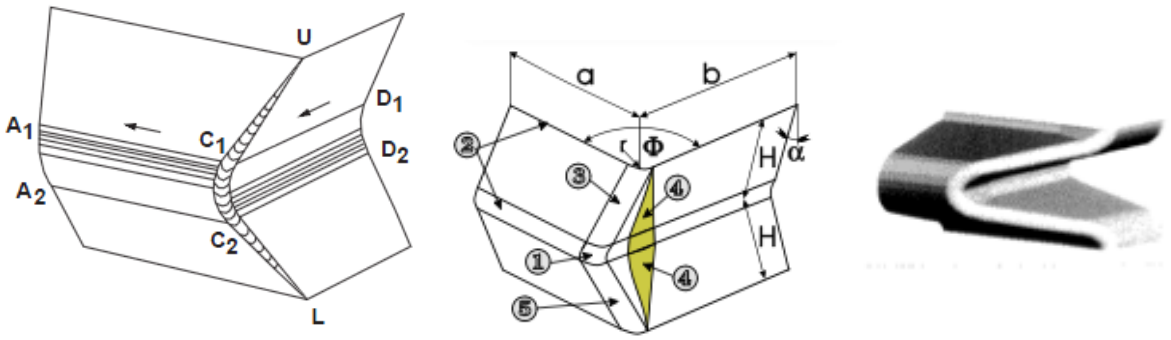

Figure 20 – Collapse mode with thickness consideration (super folding element)

Source: Du Bois et al., 2000.

All these deformations take place if the *L/b* is below a certain value otherwise Euler instability described in the beginning of the paragraph can occur and consequently the beam can't absorb the right energy *Figure 21*.

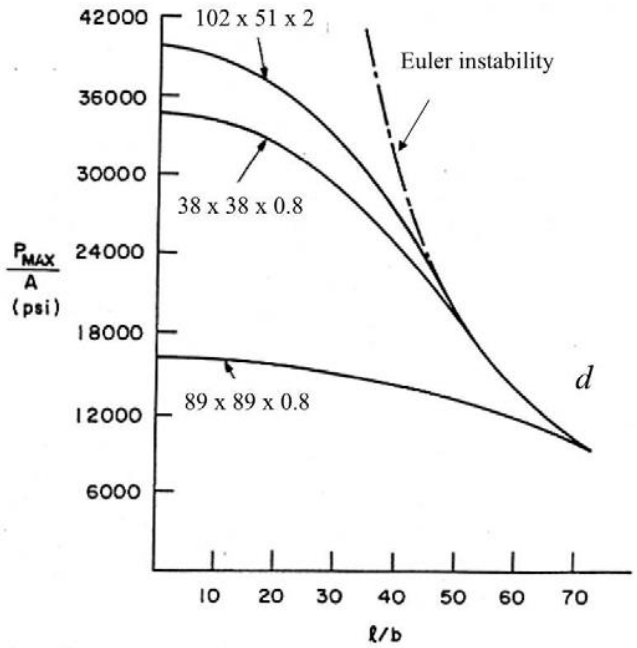

Figure 21 – Instability limit

Source: Morello, Rossini, Pia and Tonoli, 2011.

In the literature of axial crash, the other common geometry that the has been studied a lot is the cylindrical one, in *Figure 22* are proposed some experimental tests.

Figure 22 – Left to right: concertina mode, diamond mode and mix mode deformation

Al Galib and Limam, 2004.

As can be seen in the three figures above, for a circular tube there are also some principal collapse mode that are concertina (or axisymmetric) mode, diamond mode or a mix of them. The way of deformation for these circular tubes depend on the ratio *R/t* where *R* is the mean radius and *t* is again the thickness. With some investigations was approximately found that if *R/t* is lower than 40-45 the tube deforms axisymmetrically otherwise with bigger value of the ratio, the tube buckle in a diamond mode.

The pioneer of this theory was Alexander (1960) that assumed a circular tube made of an ideal plastic material that has a simplified axisymmetric deformation along plastic hinges as it shown in *Figure 23*.

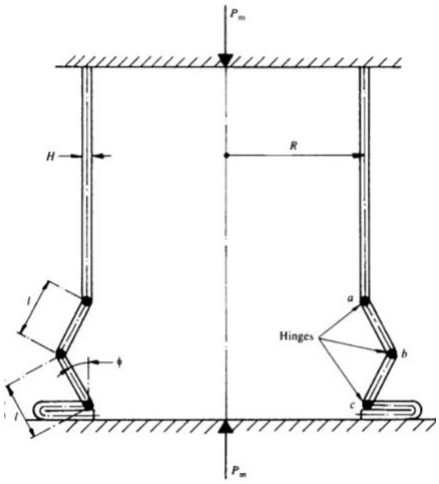

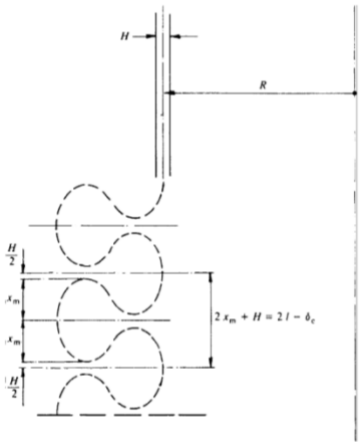

Figure 23 – Idealized concertina mode

Figure 24 – Effective crushing distance

Source: Jones, 1989.

This is a theoretical approximation and not realistic in fact the behavior of a concertina collapse mode is with curve profiles of the wrinkles instead of straight. Best approximation for mean axial

force with this idealized theory was by the equation (31):

$$P_m = 2(\pi t)^{\frac{3}{2}} R^{\frac{1}{2}} \sigma_0 / 3^{\frac{1}{4}} \tag{31}$$

After the years, this theory was modified to consider the folding radius and so Abramowicz (1983) introduced the effective crushing distance circular and so the tube collapses axially through a distance δ_e (*Figure 24*). After this modify of the theory, also the mean axial force changes in (32):

$$P_m = 2(\pi t)^{\frac{3}{2}} R^{\frac{1}{2}} \sigma_0 / \left[3^{\frac{1}{4}} \left\{ 0.86 - 0.37 \left(\frac{t}{R} \right)^{\frac{1}{2}} \right\} \right] \tag{32}$$

2.3 Improvement of thin walled geometry

After this briefly introduction on the classical square and circular tube, during the years many researchers tried to improve the energy absorption of the thin walled changing the geometry and especially introducing geometric imperfections. The main point is that, to have an optimal crash box, the *CFE* introduced before must be closest as possible to the unit value. For these reasons, there were a lot of crash boxes with trigger initiators that reduce the value of the peak force and to obtain a more constant amplitude of the load oscillation. In *Figure 25*, are presented some of classic crush initiators but every automotive company has its own design with different position of hole, beads or a combination of them.

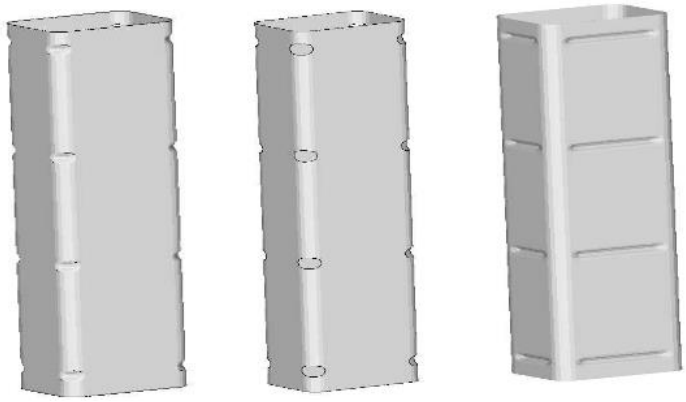

Figure 25 – Left to right: bird beaks, corner holes and surface beads

Source: Kumar, 2008.

Sanjeev Kumar [33] made a numerical study on the influence of these triggers in the overall crush response and found that peak force decreases in every configuration whereas the energy absorption increases only for the bird beak initiators. The results are a reduction of peak force respectively of 7%, 12% and 37% and for bird beak the energy absorption increase of 6% but with the other two geometries was noticed a decrease of 9%.

Another configuration was proposed by Zhang [57] with many numerical tests on grooved tube as in *Figure 26*.

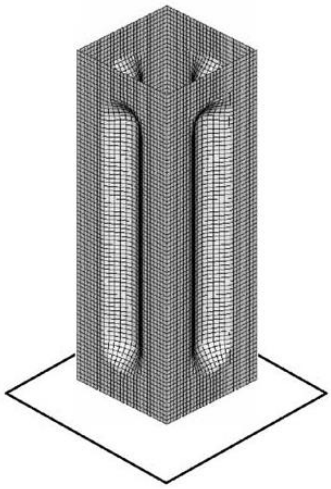

Figure 26 – Grooved tube

Source: Zhang, 2009.

The numerical results presented a significantly increase of *SEA* in comparison with conventional square tubes and the peak force is also reduced with some configurations. The aim of these tests is to have more information and knowledge on the influence of groove or holes or beads' number in each sidewall or only in two opposite sidewalls, different size and so on.

Mamalis [37] made a significant study that analyzed theoretically and experimentally the effect of circular holes on the surface of thin walled (*Figure 27*). After several tests of the position and of the holes' geometry, Mamalis found that the influence of the holes' location on the side wall is more significant than the holes' size.

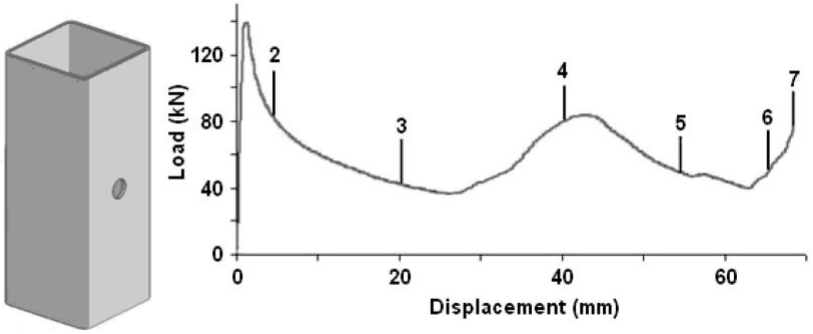

Figure 27 – Hole tube

Source: Mamalis, 2009.

Furthermore, this analysis has highlighted that specimens with a hole at middle height had better crashworthiness because they had the most energy absorption and a good decrease of peak force. Again, as can be seen in the load-displacement curve, the mean crush load remains almost constant and at high level.

Avalle, Chiandussi and Belingardi [11], proposed a different crush initiator for a cylindrical tube that is shown in *Figure 28* with the most important geometry parameters.

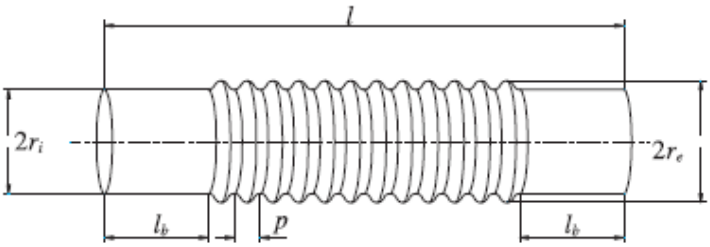

Figure 28 – Corrugated tube

Source: Avalle, Chiandussi and Belingardi, 2002.

The reserchers tried to optimized the energy absorption of this corrugated crash box, changing the bulges geometry, in particular the length p and the external radius r_e. The result of this study has allowed to obtain an optimal configuration with a LU reduction approximately of 40% compared to a reference design without an ideal bulges profile.

Another improvement of thin-walled design is represented by tapered crash box, in which the side walls have a certain inclination. This tapered thin-walled represent a new form of initiators that led to a decrease of the maximum force without compromising the energy absorption, in fact

the mean crushing force doesn't decrease too much. These specimens are recently considered for the more constant load-displacement curve compared to straight tubes and for the ability resistance under oblique impact loads.

As presented in *Figure 29,* one more technique of crash box design consists in an improvement of *SEA* using a foam filled inside a thin walled structure, instead of changing the tube geometry.

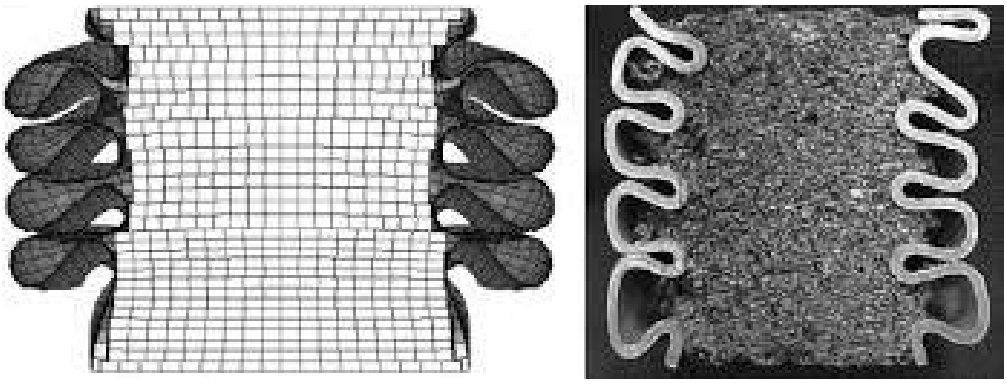

Figure 29 – Foam filled tube

Source: Attia et al., 2012.

This topic was studied a lot in the literature, Reid and Reddy (1986) conducted a study of axial crushing of thin walled filled with polyurethane and focused his attention on the influence of different densities; also Abramowicz and Wierzbicki (1988) tried to explain and quantify the interaction between a low density polyurethane foam with the sheet metal tube.

Hanssen (1999) made a lot of experiments on aluminum extrusion with aluminum foam filler and found an empirical formula for the mean crushing load that considers three factors: mean crushing load for the thin walled, uniaxial resistance of the foam core and the interactive effect by foam filling. Unfortunately, foam filled tubes have many problems, first the effective crushing distance described in the paragraph 2.2 is reduced, then they are more subjective to undesirable failure mode and also the material cost and the manufacturing process are expensive.

2.4 Crash box in the vehicle

All these improvements presented before, introducing geometry imperfection on the crash box and so trying to keep the *CFE* or *LU* as near as possible to the unit, are done for maintaining repair costs low. In fact, during an impact with a velocity less than 16 km/h that is considered low

speed, it's obvious that the cockpit must remain undeformable and so the aim is to deform only the crash box and keep the rail intact. To do this, it's necessary that the crash box absorbs all the crush energy and instead the rail must not be subjected to a plastic deformation. After a car accident at low speed is mandatory to deform only the crash box because can be changed saving a lot of money compared to the complete restore of the front frame. In *Figure 30* is presented the vehicle front structure configuration.

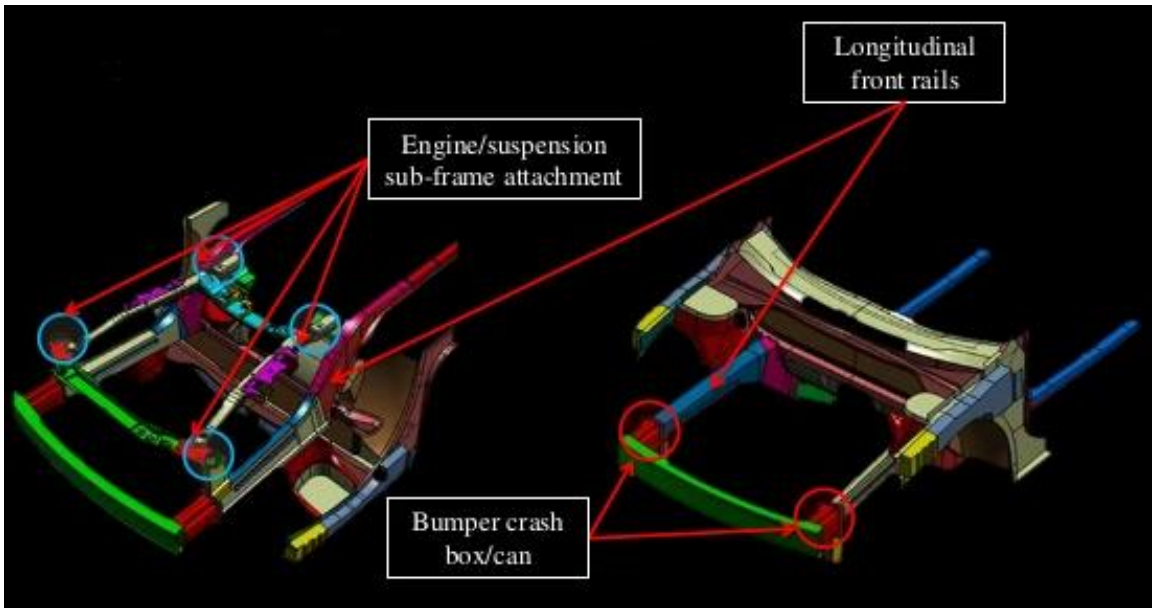

Figure 30 – Front frame

Source: Hesami, 2001

In the illustration is possible to see the position of the crash box in the front frame that is between the bumper and the longitudinal front rails. The longitudinal front rails and the engine compartment provide protection in frontal crash but allow also attachment for engine compartment components, support the engine, front suspensions and steering gear. So, it's easy to understand why in an impact is better to deform only the bumper and the crash boxes. In the paragraph 4.2 will be presented some empirical rules in the comparison between the maximum crushing force on the crash box with the crushing force of the rail and these limitations are the reasons why no crash box on the market has a straight geometry tube without buckling initiators.
Another interesting result is presented in *Figure 31* where there is the subdivision of energy absorption between the various elements.

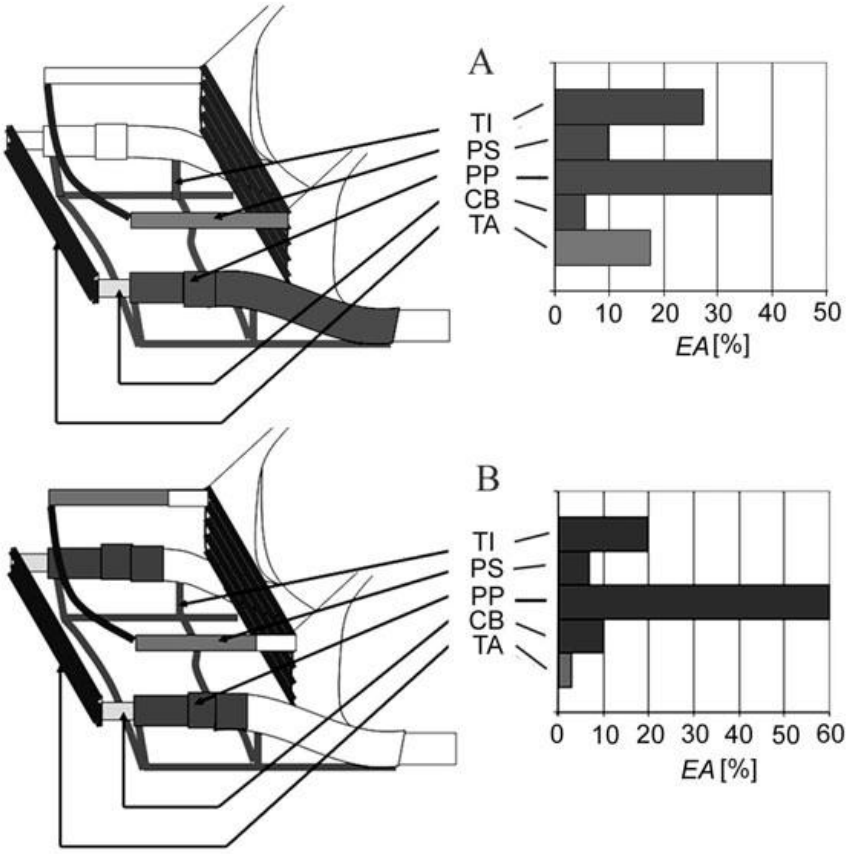

Figure 31 – Subdivision of absorbed energy

Source: Optibody project, 2012.

These two diagrams represent a front energy absorption due to an impact at 56 km/h against an offset rigid barrier (A) and against a rigid barrier (B). The acronyms mean TI=lower frame, PS=upper rail, PP=longitudinal rail, CB=crash box and TA=bumper. In these dynamic tests is shown that the crash box absorbs almost the 10% of the total kinetic energy.

2.5 Origami Engineering

The word *Origami* comes from two Japanese words that are *ori* that means folded and *kami* that means paper, but in the engineering applications proposed in the following paragraph paper is not used. However, it's very useful to utilize paper model in order to understand the way of folding and then apply these results in engineering purposes.

First, it's necessary to introduce some fundamental parameters like a crease that is a fold and can be convex or concave and it's called respectively mountain and valley. Where two or more creases join each other, a vertex is generated and all the creases make up a pattern.

There are two important theorems to obtain a foldable single vertex:

- Kawasaki's theorem says that in a sequential numeration of angles surrounding a vertex the sum of the odd angles must be equal to the sum of even ones.
- Maekawa's theorem states that looking a single angle of a flat origami crease pattern, the difference between the number of mountain (M) and valley (V) crease must be always with the 2 value. This equation that summarize the theorem is: $|M - V| = 2$.

The key concept of origami engineering is understanding how the folding crease involves rigidity to the structure. The three most common type of origami structure are: Miura-ori pattern, waterbomb base and Yoshimura pattern.

Miura-ori pattern take the name from the Koryo Miura that in 1970 devised this kind of folding; these patterns have a negative Poisson's ratio and so when the sheet is pulled in a direction, it expands in the orthogonal direction. The first application of Miura-ori was for foldable solar panel proposed in *Figure 32*.

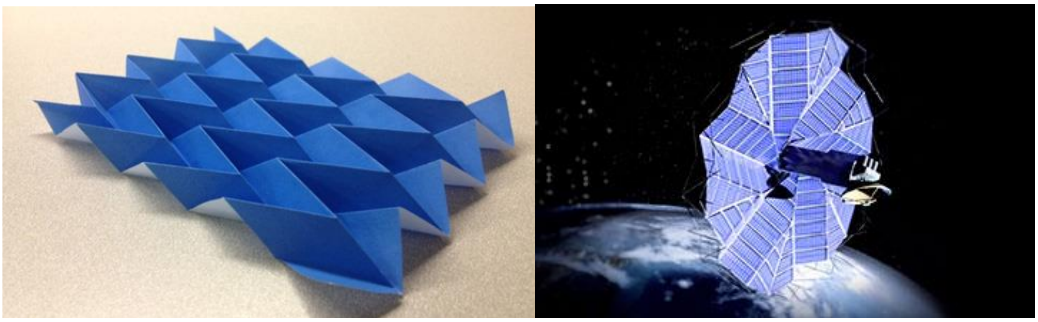

Figure 32 – Miura-ori pattern

Source: Tolman, 2014.

Another common use of origami engineering is for medic purpose, for example using the waterbomb base to make an innovative stent.

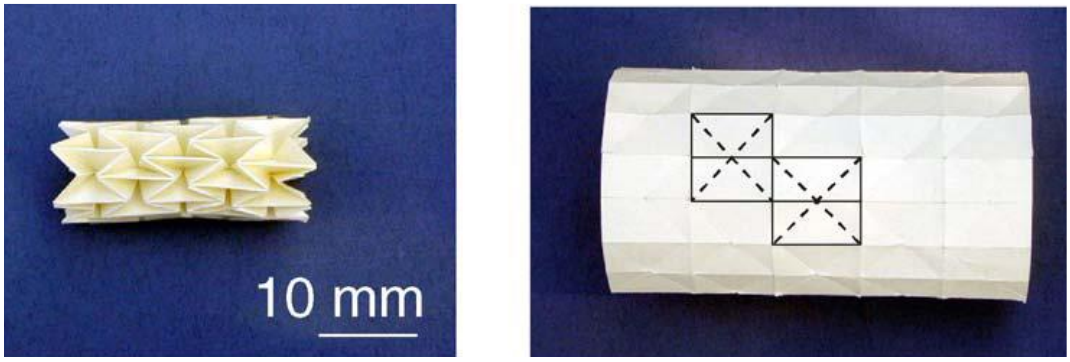

Figure 33 – Origami stent graft in fully folded (left) and deployed configurations (right)

Source: Kuribayashi et al., 2006.

In the image is presented an origami stent that is used to enlarge arteries and veins obstructed. The biggest advantage of this tecnique is to minimize invasive surgery.

Yoshimura patterns (*Figure 34*) are also a classic engineering folding and were extremely studied in the local post-buckling of thin walled cylinders.

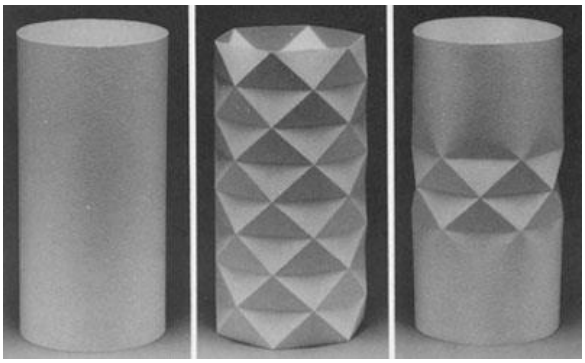

Figure 34 – Yoshimura pattern

Source: Tarnay, 1994.

The main application of Yoshimura pattern is design of collapsible cylinders or the construction of inflatable booms in space structures. The high packaging efficiency of these structures have some applications also in automotive engineering like for the storage of an airbag. In this kind of problems, the aim is to maximize the difference in area between the folded and the inflated airbag, so origami technique can be very useful.

Another application due to the packaging capacity was proposed by Zhong You and Weina Wu that created a foldable grocery bag (*Figure 35*) made of steel.

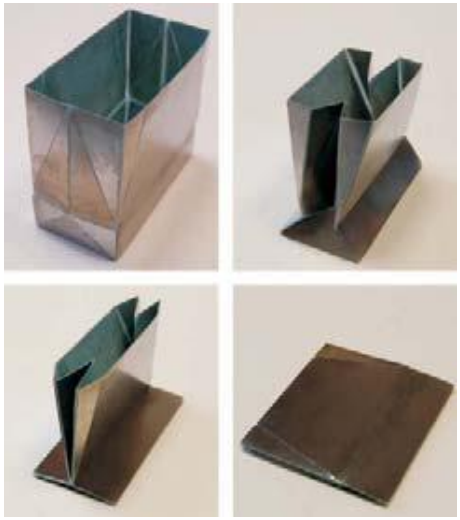

Figure 35 – Grocery bag

Source: You and Wu, 2011.

This solution allows a rigid bottom of the bag and can be used as a shopping bag or maybe in the future with some improvement on the automated folding can be used for packaging processes or for foldable shipping containers.

Origami has also an application in optics where there is the necessity of folding long focal length into small spaces. This technique creates high resolution using small mirrors that reflect light many times and find some application for the telescopes or for cell phones construction.

Recently some researchers tried to use the potentialities of this theory applying on the design of crash box or other structures responsible for the energy absorption in automotive applications. Zhao, Hu and Hagiwara (2011) built front side member with a rotation of a rectangular as it shown in the left-hand side of the *Figure 36*.

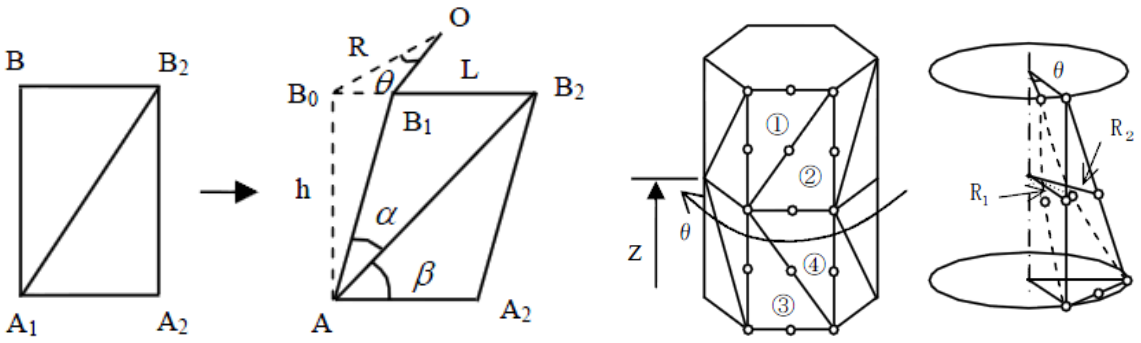

Figure 36 – Trapezoid pattern

Source: Zhao et al., 2011.

The rotation angle θ is related to the other two angles β and α with the equation (33):

$$h^2 + \left(2R \sin\frac{\theta}{2}\right)^2 = \left(\frac{L \sin\beta}{\sin\alpha}\right)^2 \tag{33}$$

where L is the edge length, R is the radius that appear due to the rotation and h is the height of the rectangular unit. After an analysis of these geometry parameters with LS-DYNA simulations, the researchers developed the best solution for energy absorption, peak force and weight that can be seen in *Figure 37* (c).

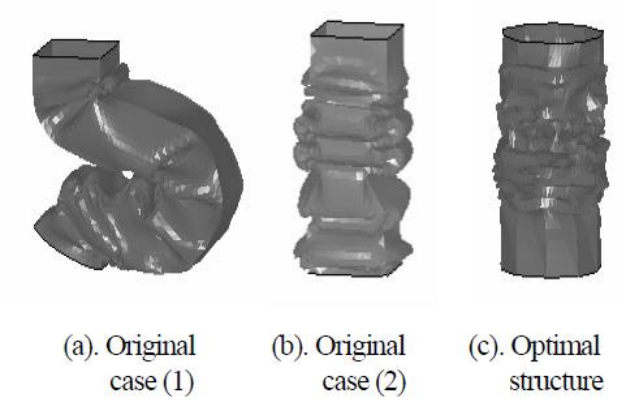

Figure 37 – Tube vs Origami beam comparison

Source: Zhao et al., 2011.

To evaluate the results and the potential of the origami beam, Zhao et al. made a comparison with two straight tube, (1) that bends during the crash and another tube (2) that deforms correctly in axial direction. In the *Table 1* is possible to see the high increase of energy absorption and also a small decrease of first peak load.

	Original case (1)	Original case (2)	Optimal structure
Absorbed energy (Nmm)	4450601	6176092	8484763
First peak load (N)	53661.11	53652.85	52450.43
Structure mass (kg)	0.532575	0.532575	0.532575

Table 1 – Energy and load comparison

Source: Zhao et al., 2011.

They founded that the origami beam absorbed almost twice energy than the tube (1) and 1,37 times more than the tube (2) and another important result is that with the origami design is more difficult to engage in an undesirable bending.

Song, Chen and Lu (2012) proposed a study on origami pattern with equilateral trapezoid as can be seen in *Figure 38*.

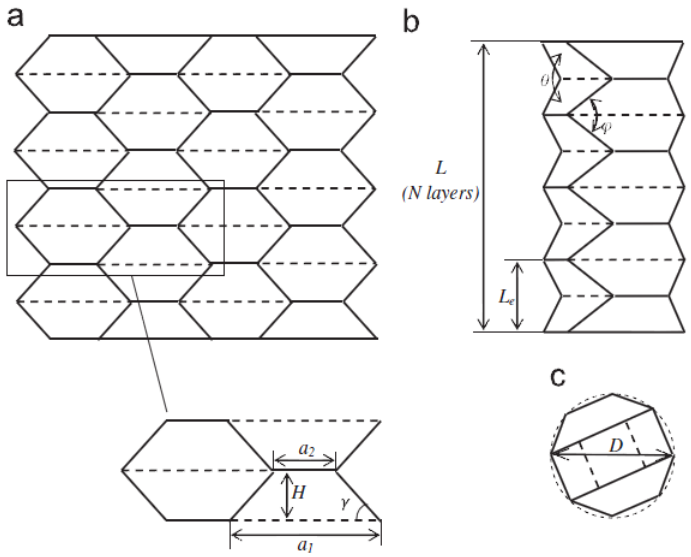

Figure 38 – Equilateral trapezoid pattern

Source: Song et al., 2012.

On the left is proposed the flat pattern with the folding line that is represented with solid line for mountain fold and dashed line for valley one. Also in this pattern, there are some fundamental parameters like the two side a_1 and a_2, the total height L, the height of each layer L_e, the base angle γ, the dihedral angle between two valley θ, the number of trapezoid place horizontally M (M=4 in the image on the left), the oblique hill angle φ and the diameter of the tube D.

The researchers found some geometric formulas to obtain a closure of the pattern and then they made many experiments changing the parameters to find the optimal solution. In *Figure 39* is proposed the result of the experimental test on the origami tube.

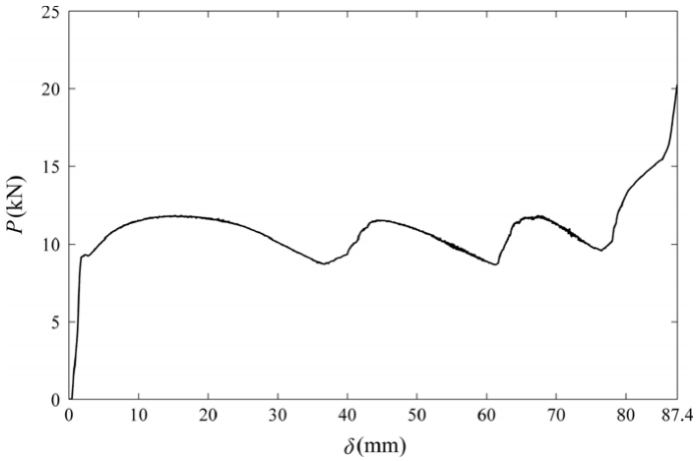

Figure 39 – Origami force-displacement

Source: Song et al., 2012

In the force-displacement curve it's easy to see a very low value of peak force, compared to a simple square tube and a smooth curve that doesn't present collapse and so the area below the curve remain wide and this guarantee a high-energy absorption.

Zhou, Wang, Ma and You (2016) designed a new module of origami crash box that has a folded lobe in every corner. In *Figure 40*, is possible to see the fundamental parameters on the flat geometry that are the side *b*, the height *l* and the length of every dashed line called *c* (*Figure 41*) that also in this case represents the valley fold.

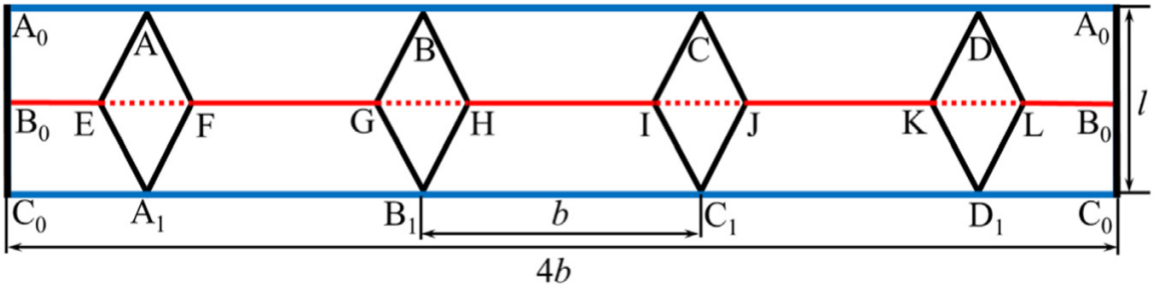

Figure 40 – Flat geometry

Source: Zhou et al., 2016

The closed geometry of a module is obtained connecting the outer side A_0 and C_0 and consequently there are other parameters like the height of module *h* that is obviously shorter than *l* and the angle θ.

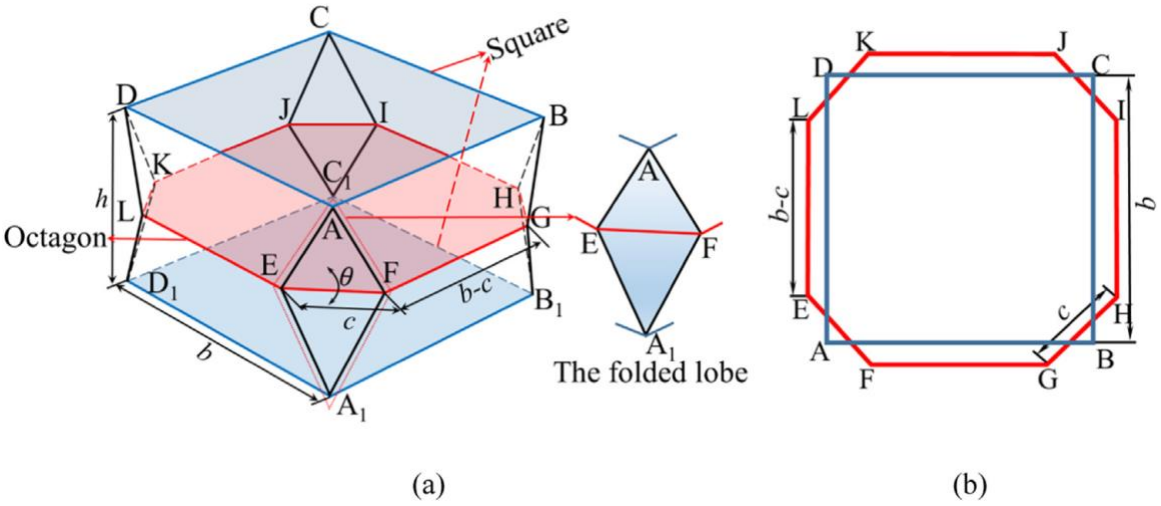

Figure 41 – Origami module and top view

Source: Zhou et al., 2016

In *Figure 41* (b), it's possible to see that the upper and the lower geometry of the module is a square with a side length of *b* and instead in the mean surface there is an octagon with the valley and the mountain folds. After many dynamic experimental tests, the researchers found that all specimens collapse in one of these three modes: complete diamond, local buckling or symmetric mode. In the first collapse mode, each lobe has a right failure but sometimes, due to manufacturing imperfections, some specimen has a certain amount of buckling points that cause the other two collapse modes. Analyzing the force displacement curve and the *CFE*, Zhou et al. understood that highest value of energy absorption is obtained with the complete diamond mode and then the symmetric collapse has better performance than the buckling mode. Another important result is that origami tube with long modules, that means a ratio between length over thickness equal to 60 performs better than shorter one with l/t=40. The paper present also the correlation between the number of buckling points with the mean crushing force and the result is that increasing the number of these point the crash boxes performance fall down. However, with the right collapse, these origami tubes allow much higher performance compared to traditional crash boxes.

3 – THEORETICAL ANALYSIS

In this thesis are presented many quasi-static impact tests on crash box structures and in the following chapter there is a summary on the theory useful to understand the physical phenomenon. The physical subject that encloses crushing events is mechanics which, through its formulas, describe the motion and the deformations of bodies subjected to forces. The four mainstay elements of this science are force, mass, time and length respectively F, m, t and L. Force is a vector quantity and has three characteristics: magnitude that allows to understand how big the intensity of the force is, the direction that represent the sense of the force and the point of application. When a body is subjected to a force can occur an external effect if the body remains rigid and so the body can change its motion with the famous Newton's second law:

$$F = ma \tag{34}$$

where a is the body acceleration and m is the mass. This happens if the body is not constrained, otherwise the body generates reaction forces. The internal effect takes place when the force is high enough to deform the body. The mass is a scalar quantity that stands for the amount of matter in a body and it's very important because represent also the energy contained in a body. Other two significant concepts that govern movement are energy and work. Energy measure the ability of something that can be a body or a system to do work and it's measured and stored in many forms. Energy is an abstract concept and can be in the form of heat and it's called thermal energy or can be electrical, mechanical energy and so on. The most useful types of energy in the field of safety are kinetic and potential energies. The kinetic energy is described by this equation:

$$E_K = \frac{mv^2}{2} \tag{35}$$

where v is the body velocity and m is the body mass. With this formula is easy to understand why the kinetic energy is related to the motion of a body. The potential energy can be described like the ability of an object to storage energy because of its position.

$$E_P = mgh \tag{36}$$

where h is the height at which the object is placed, m the object's mass and g the gravity force. Energy is also the ability of a body or a system to do work and the work is done when the energy is transferred from a body to another. When an object moves due to a force application, it is said that work is done on the object.

$$W = Fs \tag{37}$$

Where F is the applied force and s is the displacement. Considering a system in which the conservation of energy is valid, the energy cannot be created or destroyed but can only change to a form into another or transferred from a body to another. In a mechanical system, the work of external forces on the system (equation 37) is equal to the energy transmitted.

In a crash event, it must be analyzed the energy balance that represents a graph (*Figure 41*) with the different types of energy as a function of time. The most important energy in this crash analysis are kinetic, internal, sliding and total energy. The internal energy represents the part absorbed in the crash and is directly related to the force and deformation product; the kinetic as seen before is the energy of the car or the object that owns before a crash due to the velocity. The sliding interface energy represent the sum of all the energy involved in the contact and finally the total energy is the sum of all the energy involved in the crush event. The graph must follow the law of conservation energy described before and so the kinetic energy of the vehicle must be converted in internal energy, that is basically the plastic deformation.

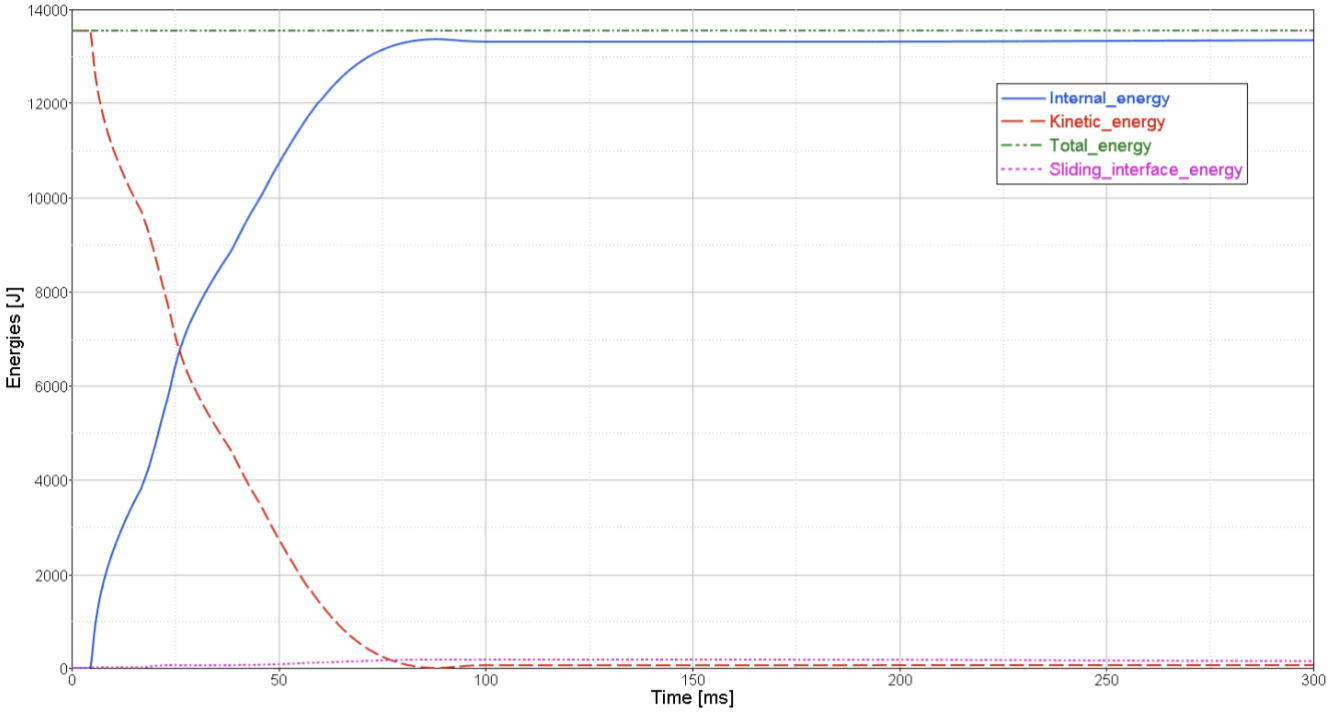

Figure 42 – Energy balance

Source: Author's own work, 2017

The image represents an energy balance of a dynamic test on a crash box and it can be noted that as the kinetic energy decrease, the internal energy increases as expected from the theory. The other important things to consider are that the total energy has to remain constant and the sliding interface must remain low, according to the LS-DYNA theory manual the peak of contact energy has to be lower than the 10% of internal energy peak.

4 – METHODOLOGY

In this section are shown the numerical apparatus that allowed to make simulations and the numerical analysis that has brought the results presented subsequently. First there is a software description, then there is a focus on the parameters imposed in this work like materials, boundary condition and so on, then in the paragraph 4.2 are presented the numerical analysis and at the end the experimental apparatus for carrying out the tests is presented.

4.1 Numerical methodology

The numerical analysis is divided in four parts: the first it's the CAD design with NX, then the geometry is imported in a pre-processing software called ANSA that allowed to make the mesh and impose the boundary condition. Then the general-purpose finite element program used to solve the differential equations is LS-DYNA and at the end HYPERVIEW is used to show the results with animation or graphs.

4.1.1 Numerical devices

The different geometries are obtained with the last version of the CAD (computer aided design) NX11. This software has the first release in the 1973 and in the 2007 was purchase by Siemens PLM software. For the pre-processing it's used the ANSA 16.2.4 version form the BETA CAE systems. CAE stands for computer aided engineering and ANSA is a tool for finite element analysis. This software is able to import many CAD files and then is very simple to make the pre-processing operation because ANSA has interoperable decks for all the most common software solvers like RADIOSS, NASTRAN, Abaqus and LS-DYNA. The solver LS-DYNA is developed by Livermore Software Technology Corp (LSTC) and was created by John O. Hallquist in the 1976 to simulate the impact of a nuclear bomb but became a public domain software in the 1978 and then year after year, material and contact model are implemented until the today's stable release R8.0. LS-DYNA is widely used in automotive and aerospace and manufacturing

industries and especially in the crash and impact analysis due to the high ability of work with nonlinear problems and transient dynamic finite element analysis. The nonlinearity can be in the variation of boundary condition, large deformation or material nonlinearity whereas the transient dynamic analysis take place where high speed is involved and the inertial forces have great influence like in the automotive crash, manufacturing processes and so on.

4.1.2 FEM method

The finite element term was born around the 1960 when the first researchers tried to simplify and approximate problems in many subjects like stress analysis, heat transfer and many others. The first book on this topic was "The finite element method in structural and continuum mechanics" and was published by Zienkiewicz and Cheung in the 1967. Nowadays this is an indispensable tool in order to reduce time to market, the product development, increasing the number of data compared to physical test and so on. This method is used after the geometry definition with a CAD software which consider continuous all the surfaces (NURBS). After that, it's mandatory to discretize the continuous geometry because complex problems have not an analytical solution and so the domain is divided in simple elements in which it's easy to calculate the differential equations; assembling these equations of every finite element, a system of equation that describe all the model is obtained. These elements are connected by points called nodes and depending on the element choice, the discretization can be made with one-dimension (1D) element like truss, beam etc, 2D element like the most common shell and plate and also 3D element for solid. The set of all the elements and nodes in the model represent the mesh.

4.1.3 Implicit vs Explicit methods

The FEM analysis, in order to evaluate the stress and strain in each finite element, the nodal displacement is the most important variable. Every CAE software can study this kind of problems with two approaches: implicit and explicit. These two methods are briefly described with the classical truss problem which can be seen in *Figure 43*.

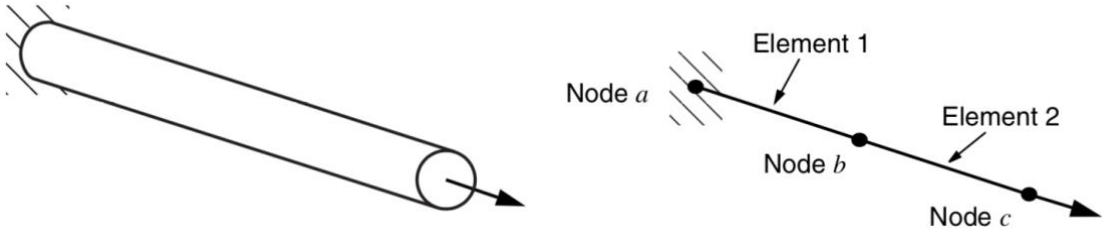

Figure 43 – Truss problem

Source: Getting Started with Abaqus, 2011

In the left-hand side it's proposed a simple truss element and, in the side, there is the discretization with three nodes and two rod elements. The aim is to calculate the displacement of the truss element in the end side where there is a force application. To do this, the implicit method wants to guarantee the static equilibrium and so it's possible to draw a free body diagram (*Figure 44*) in each node.

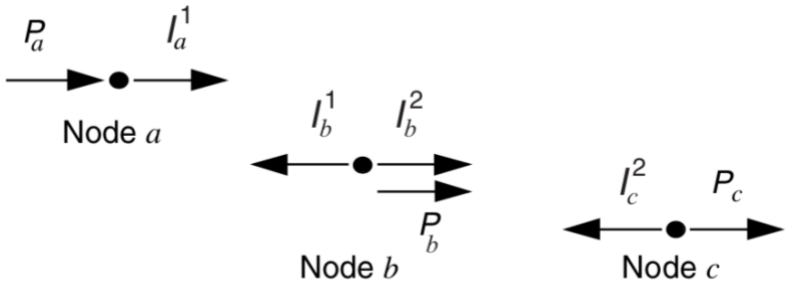

Figure 44 – Free body diagram

Source: Getting Started with Abaqus, 2011

Where P_a, P_b and P_c are the subdivision in each node of the external load P and I are the internal stresses generate to guarantee the null net value in each node and so the static equilibrium. After this diagram, it's possible to calculate the strain in the first element:

$$\varepsilon_{11} = \frac{u^b - u^a}{L} \tag{38}$$

where u^b and u^a are the nodal displacements and L is the element's initial length. Assuming an elastic material for the rod, the stress is simply calculated like:

$$\sigma_{11} = E * \varepsilon_{11} \tag{39}$$

where E is again the Young's modulus. Knowing that the internal forces are the multiplication of stress per the cross-sectional area (A), it's possible to combine the equations (38) and (39) to obtain:

$$I_a^1 = \sigma_{11} * A = \frac{EA}{L}(u^b - u^a) \tag{40}$$

And so, the equilibrium at node a is:

$$P_a - \frac{EA}{L}(u^b - u^a) = 0 \tag{41}$$

The implicit method solves for each node this equations system, obtaining this matrix formulation:

$$\begin{Bmatrix} P_a \\ P_b \\ P_c \end{Bmatrix} - \left(\frac{EA}{L}\right)\begin{bmatrix} 1 & -1 & 0 \\ -1 & 2 & -1 \\ 0 & -1 & 1 \end{bmatrix}\begin{Bmatrix} u^a \\ u^b \\ u^c \end{Bmatrix} = 0 \tag{42}$$

where the matrix multiplied by the term EA/L is the famous stiffness matrix.

The explicit method has a completely different logic, doesn't need to solve this general system equilibrium equations that led to a stiffness formulation, but the solution is obtained from the previous increment through a stress wave propagation proposed in *Figure 45*.

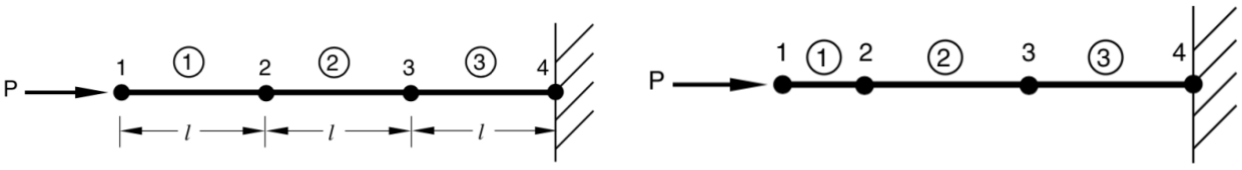

Figure 45 – Stress propagation

Source: Getting Started with Abaqus, 2011

In the left-hand image, there is the initial configuration of the rod, and in right-hand side is proposed the first increment in which the node 1 has an acceleration caused by the external force *P*. Deriving the acceleration is possible to obtain the node velocity and through this it's possible to calculate the strain rate and then deriving this value in the first-time increment, it's obtained the strain and consequently the element stress. All the passages are summarized by these equations:

$$\ddot{u}_1 = \frac{P}{M_1} \rightarrow \dot{u}_1 = \int \ddot{u}_1 \, dt \rightarrow \dot{\varepsilon}_{el1} = -\frac{\dot{u}_1}{l} \rightarrow \Delta\varepsilon_{el1} = \int \dot{\varepsilon}_{el1} \, dt \rightarrow$$
$$\varepsilon_{el1} = \dot{\varepsilon}_0 + \Delta\varepsilon_{el1} \rightarrow \sigma_{el1} = E\varepsilon_{el1} \tag{43}$$

where M_1 is the mass of element 1, $\ddot{u}_1$ and $\dot{u}_1$ are the acceleration and the velocity of node 1 respectively. Now in the second increment, the stress is propagated until the node 2 which produces a reaction force and it's possible to calculate the dynamic equilibrium between the node 1 and node 2 with the free body diagram presented in *Figure 46*.

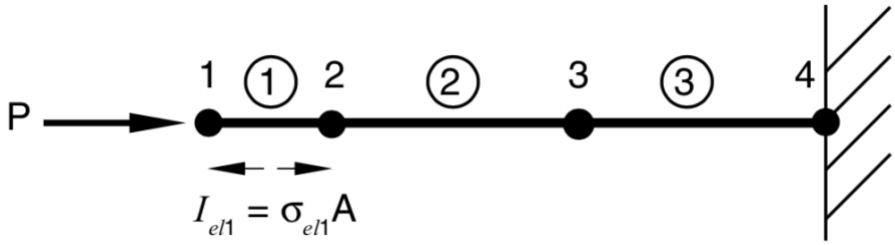

Figure 46 – Free body diagram 2° increment

Source: Getting Started with Abaqus, 2011

The same equations (43) with the introduction of internal reaction force I_{el1} are used to calculate the dynamic equilibrium between the node 1 and node 2 and then the stress propagation is applied to all the nodes. With this simple example it's clear that in the explicit method there was no need to calculate the stiffness matrix and so the solver don't have to invert the matrix to obtain a solution that require a high computational cost as it done in the implicit method.

In the explicit time integration, the software uses a central difference rule to integrate the equation in the time. In the first increment a dynamic equilibrium is solved:

$$M\ddot{u} = P - I \tag{44}$$

where *M* is mass matrix and *P* and *I* are again the external and the internal forces. Inverting the mass matrix that is usually a lumped matrix, it's easy to calculate the acceleration at the first increment. The formula to calculate the velocity, assuming a constant acceleration is the following:

$$\dot{u}_{\left(t+\frac{\Delta t}{2}\right)} = \dot{u}_{\left(t-\frac{\Delta t}{2}\right)} + \frac{\Delta t_{(t+\Delta t)} + \Delta t_{(t)}}{2}\ddot{u}_{(t)} \tag{45}$$

where $t + \frac{\Delta t}{2}$ is the velocity in the middle of the increment. After that, it is possible to calculate the displacement through a time integration with the equation:

$$u_{(t+\Delta t)} = u_{(t)} + \Delta t_{\,(t+\Delta t)}\dot{u}_{\left(t+\frac{\Delta t}{2}\right)} \tag{46}$$

The word explicit derives from the fact that the displacement after a time increment depends only on the acceleration, velocity and displacement on the previous increment. The problem of this method is that, for having a high resolution of the solution, the time increment must be small in order to guarantee a quite constant acceleration in every increment. This is the reason why usually for static analysis, in which there is not the effect of mass and dumping, it's used an implicit software to have a better solution and in the dynamic analysis can be used both method but increasing the velocity and so the effect of inertia, it's preferred to use an explicit solver (*Figure 47*). More is the velocity of the event, more convenient is the using of explicit methods because it's possible to have very small increment if the physical phenomenon is quick, like in explosion or a crash simulation.

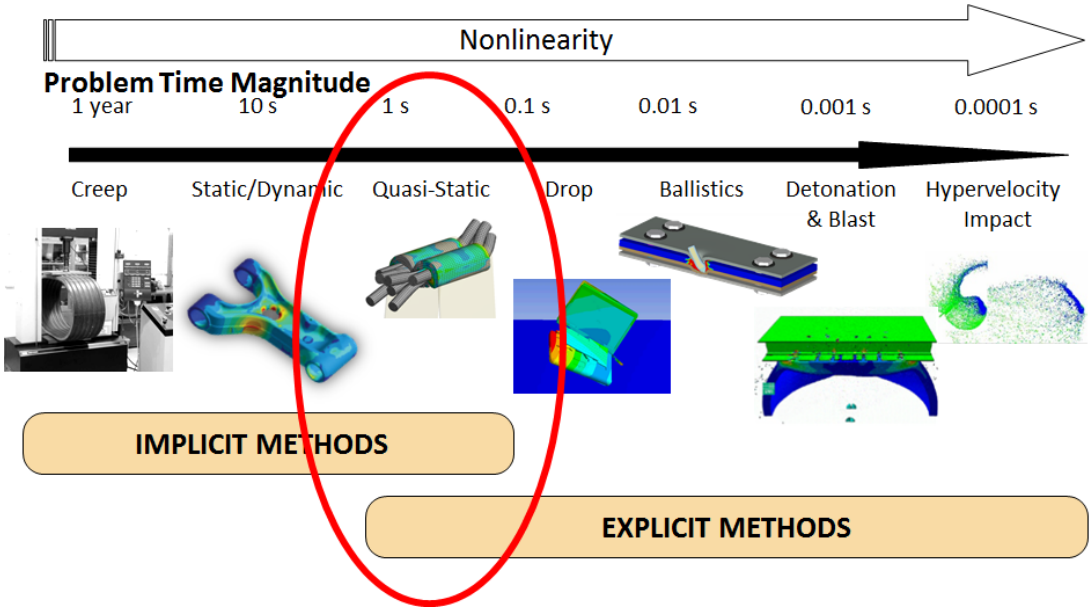

Figure 47 – Explicit vs Implicit application

Source: Davies, 2015

In the middle of the figure, there is a quasi-static analysis in which can be used both methods but with some effort it's better to use a faster explicit method. Another big difference of these two methods is that an implicit solver is unconditionally stable, while the explicit method has a stability limit. This limit is usually considered by the equation:

$$\Delta t_{stable} = \frac{L_{element}}{v_{wave}} \tag{47}$$

where $L_{element}$ is the minimum length element of the mesh and v_{wave} is the wave speed of the material that is calculated with:

$$v_{wave} = \sqrt{\frac{E}{\rho}} \tag{48}$$

where ρ is the mass density and E is the elasticity modulus and so this wave speed is a property of every material. In other word, the equation (47) states that the time increment of an explicit

method has to be lower than the time spent by the wave to cross the element length; this is the so called Courant stability.

4.1.4 Element formulation

After the description of the method used in this work, here are presented the shell elements used to simulate the various geometries. A shell is a three-dimensional structure with a value of the thickness much smaller than the other two dimensions. This element derives from a plate with the addition of a middle surface and a single or a double curved surface. A shell is approximate like a flat element and then a thickness value is entered as an input. The great advantage of these elements compared to the plate, is the ability to support normal and tangential external load acting on the mean surface. In *Figure 48* are presented the degree of freedom of a shell element.

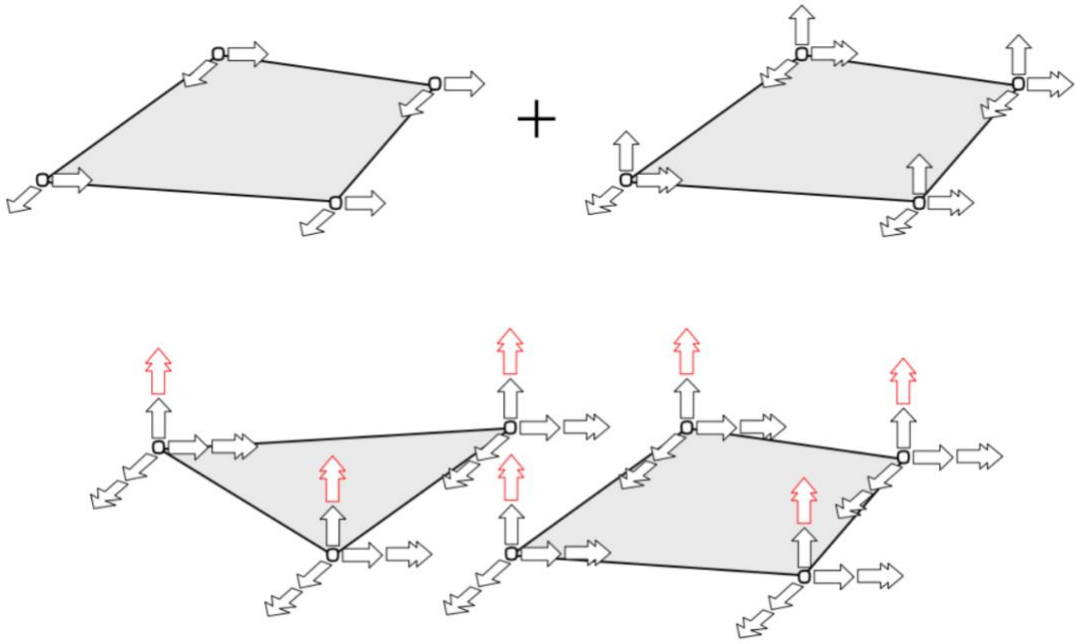

Figure 48 – DOF Shell element

Source: http://homepage.tudelft.nl/p3r3s/b17_handout_4.pdf

A shell element can be seen as a combination of a plane element that support plane stress like a membrane and a plate element that support bending and so every node has six degrees of freedom. The sixth DOF represented with the red arrow is used by the finite element program when two shell elements are perpendicular connected.

In the crash simulation, the most used element is 4-noded Belytschko and Tsay shell (ELFORM2 for LS-DYNA) because of the high computational efficiency. In *Figure 49*, are presented the number of integration point (NIP) on the element.

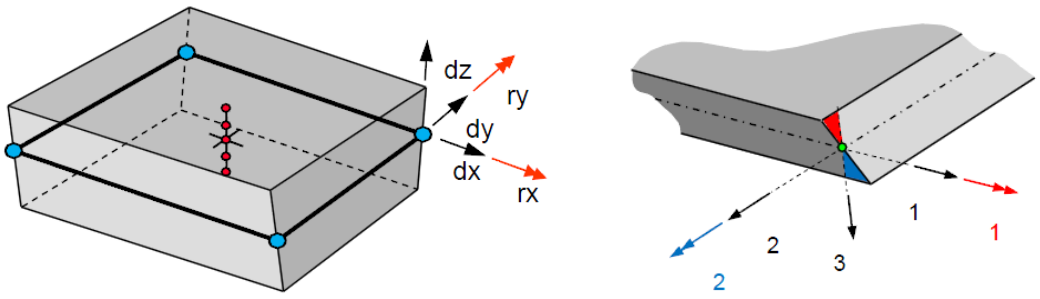

Figure 49 – NIP Belytschko and Tsay element

Source: Haufe1, Schweizerhof, DuBois, 2013

It is possible to see only a point on integration for efficiency reason in the plane and so there are five NIP through the thickness which they guarantee a good description of the physical problem when thickness deformation are present.

The element formulation used in this work is the ELFORM16 (*Figure 50*) which is derived from the element described before with some important differences.

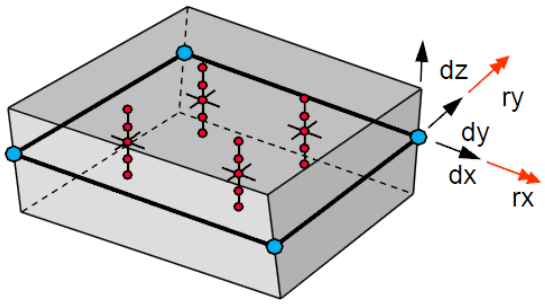

Figure 50 – ELFORM16

Source: Haufe1, Schweizerhof, DuBois, 2013

This formulation is more suitable for crash simulation because the element is fully integrated and has four integration points in the plane surface. This solution has the same kinematic assumption

based on Reissner-Mindlin of ELFORM2, but there is a variation that allow to decouples the DOF on the thickness between the elements. The computational cost is two or three times more expensive than the Belytschko and Tsay shell but is recommended in this kind of simulations.

4.1.5 Material model

The material utilized for the first crash box specimens is a dual phase (DP) steel because it's commonly used in the automotive industry thanks to its properties. The microstructure of the DP is made of hard martensite phase dispersed in a ferritic matrix and this guarantee a high strain hardenability, high drawability, good fatigue strength and high energy absorption. This is the reason why many structural parts, reinforcements and also crash boxes are made with this steel. After some manufacturing limitation, it's also used the FEE340 material for other simulations. In order to assign the material to the specimen, it's used the MAT24 that in LS-DYNA represent Piecewise linear isotropic plasticity. With this Material model it is possible to consider the effect of the strain rate. The software calculates the deviatoric stresses to guarantee the equation:

$$\emptyset = \frac{1}{2} s_{ij} s_{ij} - \frac{\sigma_y^2}{3} \leq 0 \tag{49}$$

where s_{ij} is the deviatoric stress that is needed to determine the yield function and:

$$\sigma_y = \beta\left[\sigma_0 + f_h\left(\varepsilon_{eff}^P\right)\right] \tag{50}$$

in which β is the parameter that take into account the strain rate effect and $f_h\left(\varepsilon_{eff}^P\right)$ is the hardening function in which ε_{eff}^P is the effective plastic strain. There are many option to take into account the strain rate with this material formulation, like using Cowper-Symonds model or defining the β coefficient but in this work have been imposed a true stress-strain curve for many strain rate obtaining a problem description as the *Figure 51*.

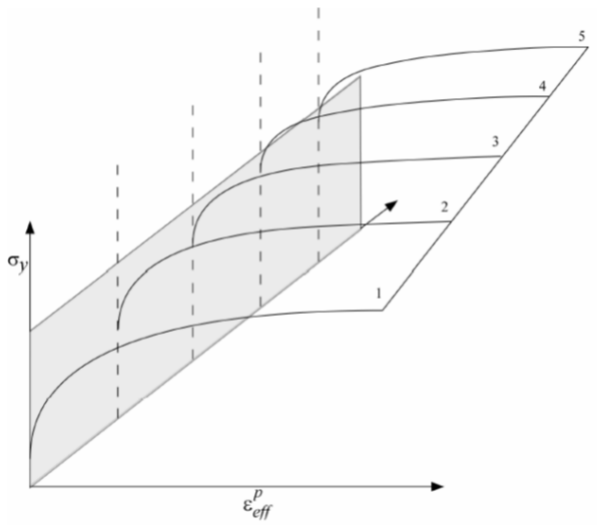

Figure 51 – Strain rate effect

Source: Hallquist, 2006

Specifying these curves like an input, it allows the software to calculate the plastic deformation. When the strain rate is an intermediate value, LS-DYNA, interpolates between the curves or if happened that there is a strain rate lower than those entered as input, it's used the lowest curve and the same is made for the highest curve. Have been also imposed the general property of this steel as it possible to see in the *Table 2*:

Material property	
Density [kg/m^3]	7800
Young's modulus [GPa]	210
Poisson's ratio	0,3

Table 2 – Dual Phase property

Source: Author's own work, 2017

The other material model applied is the MAT20 that simulates a rigid body as the plate used to deform the crash box. With this formulation there is no need to impose stress-strain curves because the software considered the part like infinite rigid without relative displacement and deformations. It is necessary, however, to enter constrain parameters and the same property

values of *Table 2* because the software uses Young's modulus and Poisson's ratio to calculate the sliding interface parameters when the rigid plate comes into contact with other elements.

4.1.6 Contact model

In a CAE software, it's necessary to have an accurate contact modeling in order to guarantee a trustworthy simulation of the physical problem. To do this, LS-DYNA allows to choose between many contact algorithms depending on the application to be studied. When two surfaces come into contact, there is the risk of nodes interpenetration among two elements and this can cause wrong results or numerical instabilities that could block the simulation. The software argues with a penalty method which avoids the interpenetration putting linear springs between every node that penetrate through the surface and the closest master surface like presented in *Figure 52*.

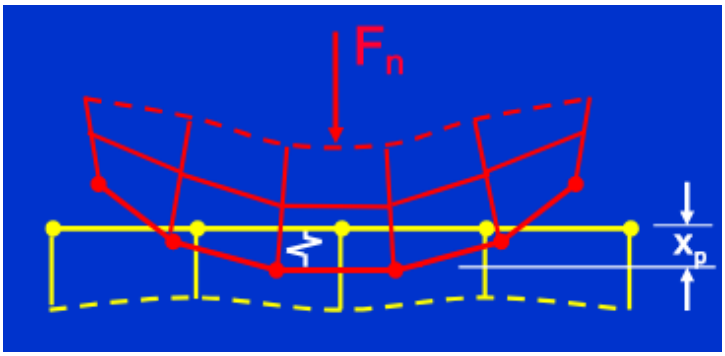

Figure 52 – Penalty method

Source: Ansys training manual, 2001

This method let to eliminate the penetration introducing a contact force to satisfy the equilibrium:

$$F_c = k_c x_p \tag{51}$$

where k_c is the contact or penalty stiffness and x_p is the value of penetration. The magnitude of the contact force has to be big enough to push back the surface avoiding interpenetration but cannot be too high to separate the surfaces because also this causes instabilities. It is not possible to obtain a zero value of penetration because the stiffness should be infinite but maintaining a low penetration distance, the simulations remain precise.

The contact type used in this work is the AUTOMATIC_SINGLE_SURFACE of LS-DYNA that it's recommended for crashworthiness simulations for many reasons. The first is that there is no need to specify the master and slave surfaces because the software decides automatically alone how to treat every surface. It is quite helpful to apply this contact method in the crash models because all the elements are included in one single set and LS-DYNA considers also when a part comes into contact with itself. There are many parameters to define well a contact problem and here there is a description of those that were used in this work. First of all are imposed the *FS* and *FD* that are static and dynamic friction coefficient respectively with a value of 0,2. Then it's imposed a *VDC* value of 20 that is the viscous damping coefficient; this parameter is expressed as a percentage of the critical damping and allows to reduce oscillation in the contact. *SFS* and *SFM* are respectively the scale factor on default slave and master penalty stiffness, but these parameters are not imposed because as written before the automatic single surface doesn't need the input of master and slave surfaces. Another important parameter is the soft constraint option that is imposed with the EQ.1. The *SOFT 1* is called soft constrain formulation and differs from the default penalty formulation (*SOFT 0*) only for the stiffness calculation. The soft formulation is more precisely when soft materials comes in contact with much more stiffer materials or when there is a high difference in the mesh densities. This option 1 in fact calculates the penalty contact stiffness considering the timestep and the nodal masses as:

$$k = SOFSCL\frac{m}{(\Delta t)^2} \tag{52}$$

where m is the nodal mass, Δt is the time increment or timestep and $SOFSCL$ is a scale factor that guarantee numerical stability. In this work the scale factor $SOFSCL$ is imposed by the value 0,1. The last parameter imposed is the *DEPTH* that in general it's set by the option 1 for most common crush application, but here is imposed with the value 2 that is more expensive but gives better accuracy because controls the surface penetrations for each node.

4.2 Numerical analysis

The first aim of this work is to improve the energy absorption of a crash box but this component, as seen in the paragraph 2.4, is designed in order to deform before the rail. To achieve the total deformation of the crash box before the plastic deformation of the rail a good idea is to compare the absorption of these two elements and establish some empirical rules. First of all, is analyzed a general rail proposed in *Figure 53* with a quasi-static test.

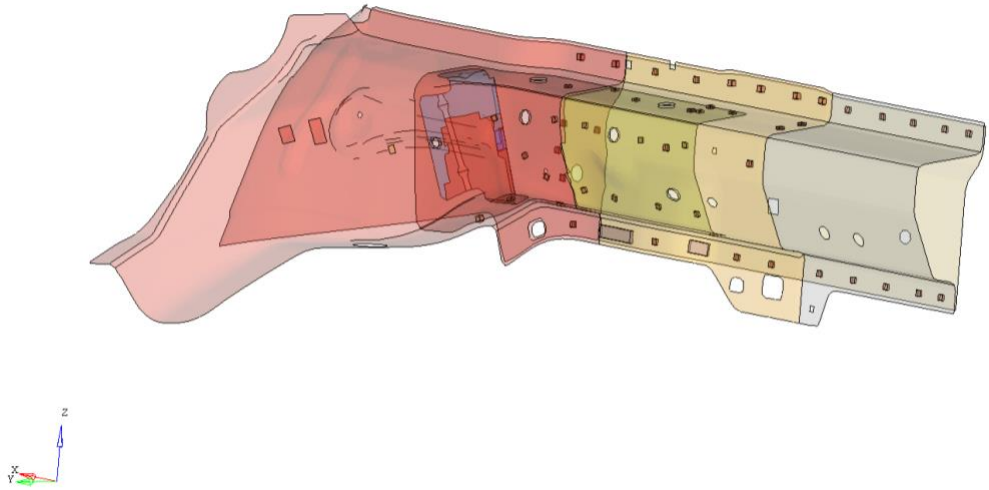

Figure 53 – General rail

Source: Author's own work, 2017

The rail made of a high strength low alloy is subjected to an axial impact with a rigid barrier that has a very low velocity, it's imposed 0,042 m/s that allow to understand the structural behavior characterized by the regular generation of plastic fold and to avoid dynamic phenomena. According to Jones [31], below 10 m/s the inertia effects can be ignored. The test is reproduced with the same boundaries condition of the barrier but using a tube with a straight geometry (*Figure 54*).

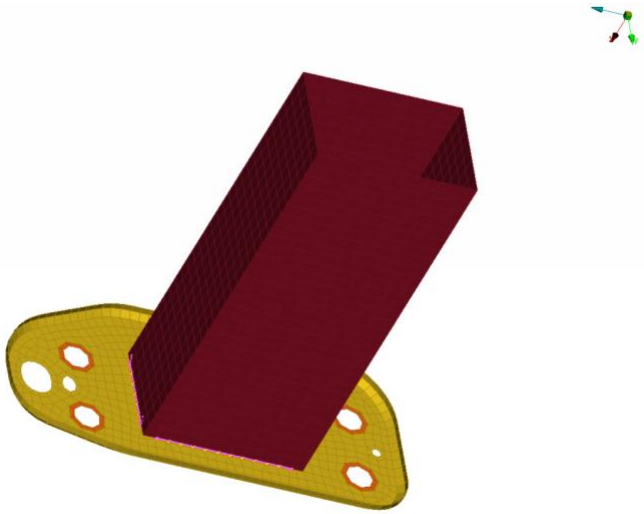

Figure 54 – Tube

Source: Author's own work, 2017

This tube has a height of 250 mm and a rectangular section with a smaller side of 68 mm, a larger side of 110 mm and a 1,6 mm of thickness. At the bottom of the specimen, there are the SeamLines in pink that represents the spot-welds that constrain the tube to a thick plate of 10mm in yellow. The result of these two tests are summarized in the graph of *Figure 55*.

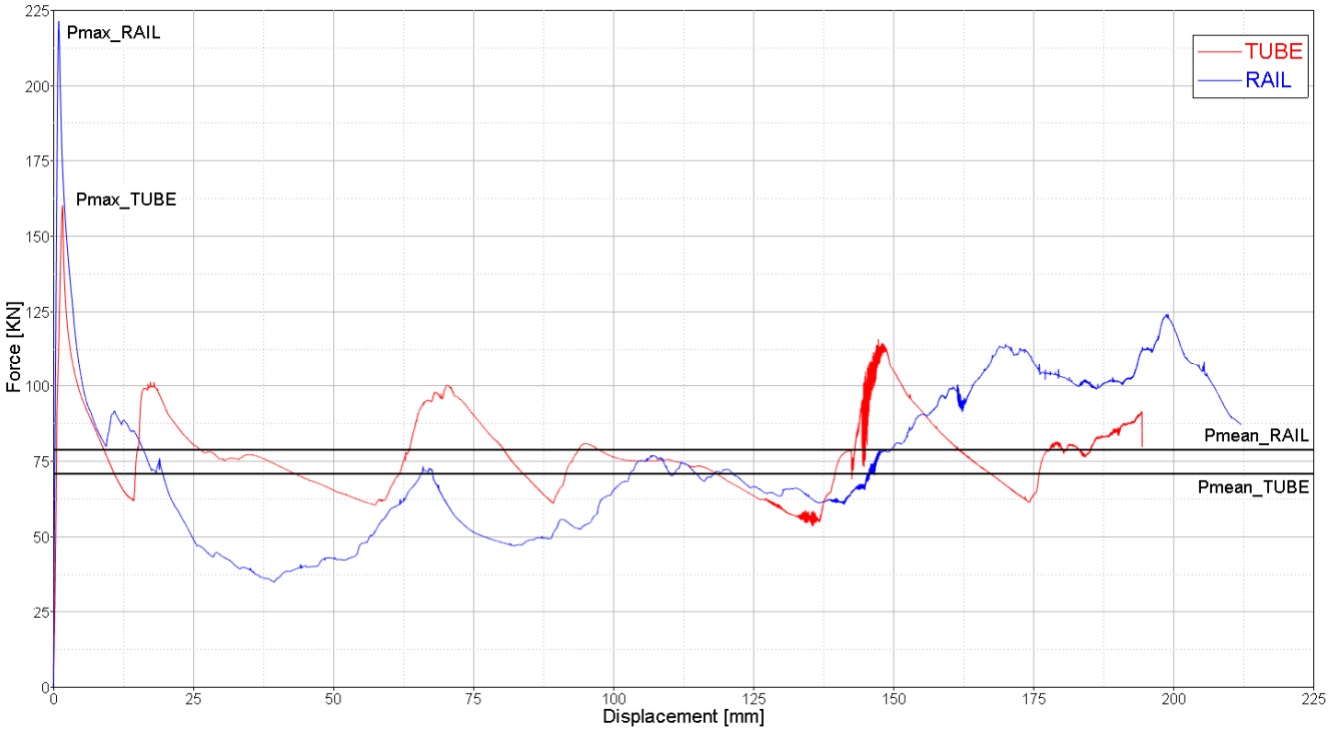

Figure 55 – Force-displacement comparison: rail vs tube

Source: Author's own work, 2017

As written before, in a force-displacement graph are easily definable some important points like the mean and the maximum crushing forces and the conditions that a crash box must be respect are related to those values. The maximum crush load of the crash box should be lower than the maximum crush load of the rail and also lower than the mean crush load of the rail; these empirical rules are summarized below.

$$P_{maxCrashBox} < P_{maxRAIL} \tag{53}$$

$$P_{maxCrashBox} \leq P_{meanRAIL} \tag{54}$$

Considering the rail and the tube's comparison of *Figure 55*, it is possible to see that the equation (53) is respected but the other condition is completely violet in fact the P_{max} of the tube is much higher than the $P_{meanRAIL}$. The test was then repeated changing the tube with a general crash box geometry with some initiators as it's possible to see in *Figure 56.*

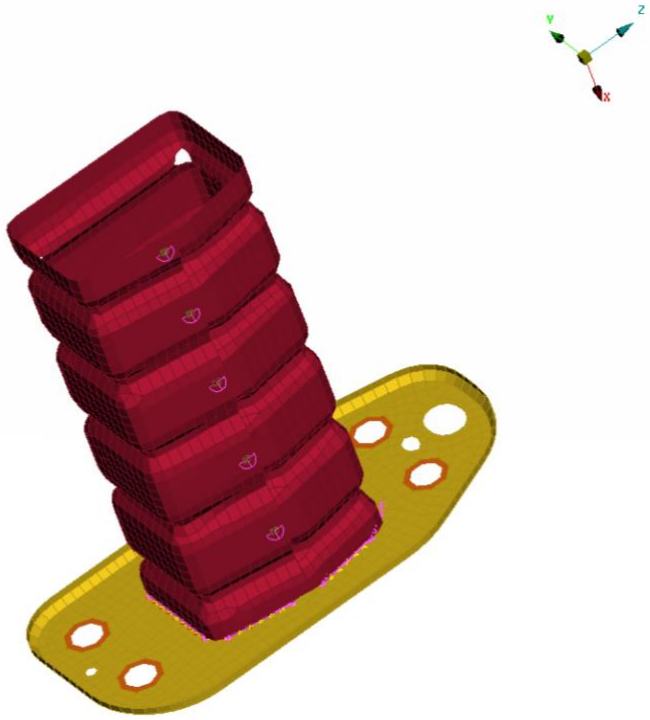

Figure 56 – General crash box

Source: Author's own work, 2017

This crash box has the same sizes of the tube like height, both sides, thickness and an identical constrain to a plate but, in addition, there are many corner holes and surface beads to decrease the peak force. In *Figure 57*, there is another force displacement graph in which is plotted again the rail curve and the curve of this crash box with initiators.

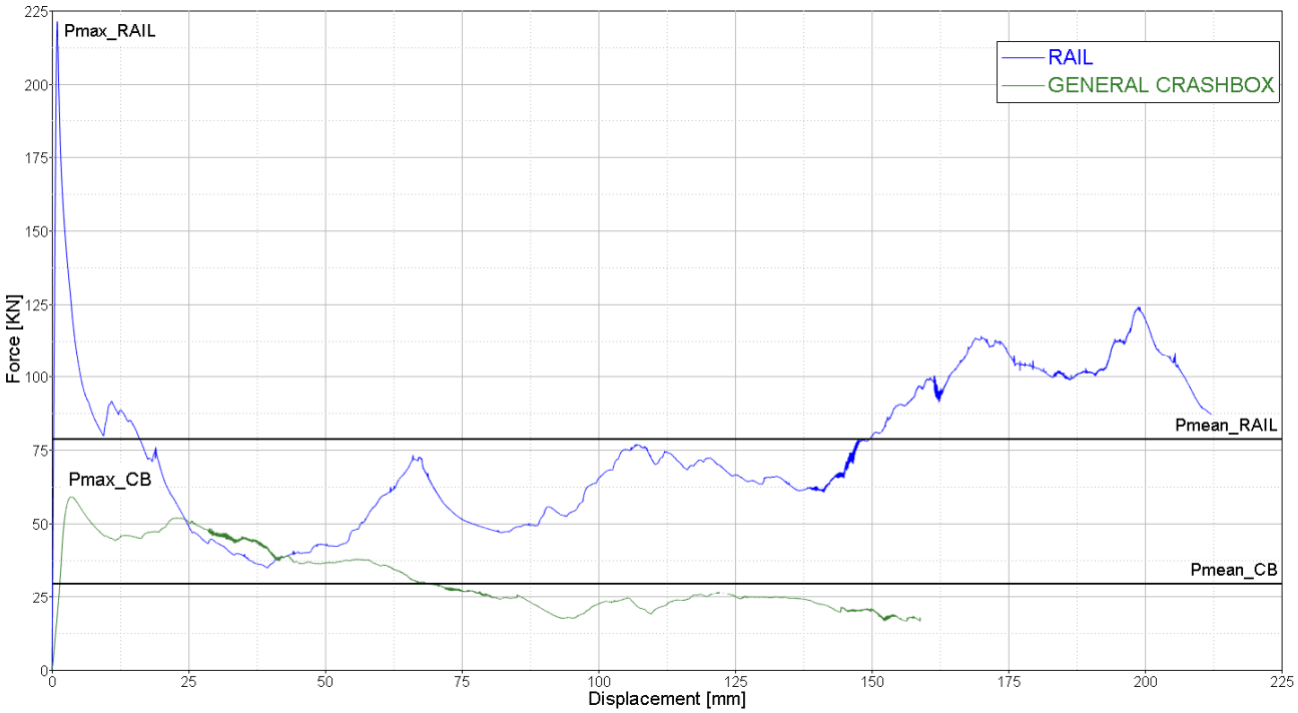

Figure 57 – Force-displacement comparison: rail vs general crash box

Source: Author's own work, 2017

Considering this general crash box, it is possible to see how the green line respect the two equations (53) and (54) and so in case of a low speed accident will be surely guaranteed a complete deformation of the crash can before the rail's deformation. This numerical analysis was useful to understand the limit forces so as to design a new crash box which guarantee these stringent conditions but increasing the energy absorption.

The specimen geometry studied in this work is the one proposed by Zhou et al. [59] with some corrections in order to adapt to the general crash box size. The *b* dimension was imposed with a 90 mm value so as to obtain the same perimeter of the general crash can and also the height was chosen to get as close as possible to the value 250 mm. All the parameters used to define this geometry are presented in the following table.

b [mm]	*l* [mm]	*c* [mm]	*2θ °*	*L* [mm]	*M*	*H* [mm]	*t* [mm]
90	90	45	156	88,05	3	264,1	1

Table 3 – Origami geometry

Source: Author's own work, 2017

Imposing the values of the lobe length *c* and the height of the flat module geometry *l*, is obtained the inclination angle with the following equation.

$$\cos\theta = \left(\sqrt{2} - 1\right)\frac{c}{l} \tag{55}$$

This angle is calculated doing the *arccos* and then in the table is proposed the double of the angle because also in *Figure 58* is easily represented the *2θ* angle. Using these parameter for the flat geometry, it's possible obtain a closed structure similar to a tube with a height of 88,05 mm because of the inclination angle.

$$L = l\sin\theta \tag{56}$$

The total height of this origami crash box is obtained reproducing the module three times, *M=3* in the table and so is reached a total height of 264,1 mm and a value of one millimeter for the thickness is imposed. The result of choosing these parameters is presented in the following NX draft.

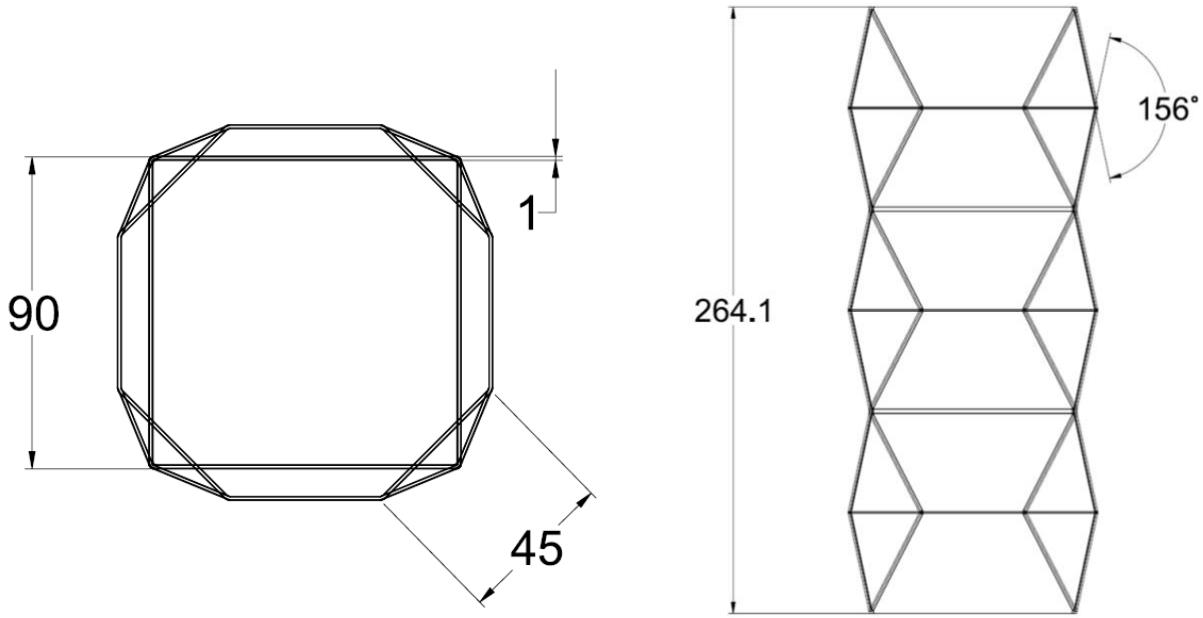

Figure 58 – Origami geometry draft

Source: Author's own work, 2017

The draft underlines all the geometric data explained before and summarized in the *Table 3* and in the left hand image is possible to see the bottom square section. After that, the CAD file is imported in ANSA, meshed with the element by the formulation 16 described in the paragraph 4.1.4 and in the *Table 4* is possible to see all the parameters set.

Criteria	**Calculation**	**Value**
Aspect ratio	NASTRAN	5
Skewness	PATRAN	45
Warping	I-DEAS	15
Jacobian	ANSA	0,6
Min length	I-DEAS	3,5
Max length	I-DEAS	8
Min angle quads	I-DEAS	45
Max angle quads	I-DEAS	135
Min angle trias	I-DEAS	20

Max angle trias	I-DEAS	120
Triangles %		5

Table 4 – Mesh parameters

Source: Author's own work, 2017

All these mesh criterias are imposed with different software logic and in the following images are presented some schematic drawings to understand the input values. The last criteria represents the percentaige of tria element contained in a mixed mesh.

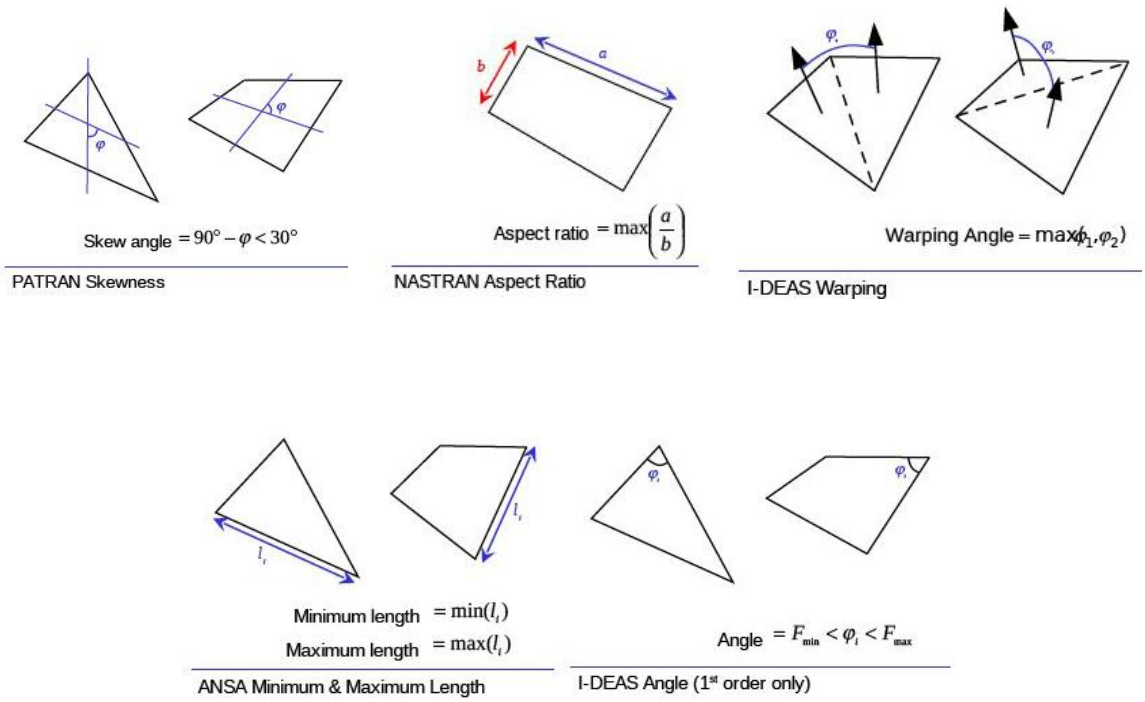

Figure 59 – Mesh criteria

Source: Author's own work, 2017

In the LS-DYNA control, furthermore, it is imposed the timestep for mass scaled solutions with the command DT2MS. The size of this timestep is set with the value -0,0007 and the *TSSFAC* that is the scale factor is imposed as 0,9. Considering the Courant stability limit, the equation (47) is satisfied because the value of $6{,}3*10^{-4}\ s$ for the timestep used is less than the smallest element's size divided by the wave speed in the DP or FEE340 material utilized. The result of this meshing procedure is presented in *Figure 60*.

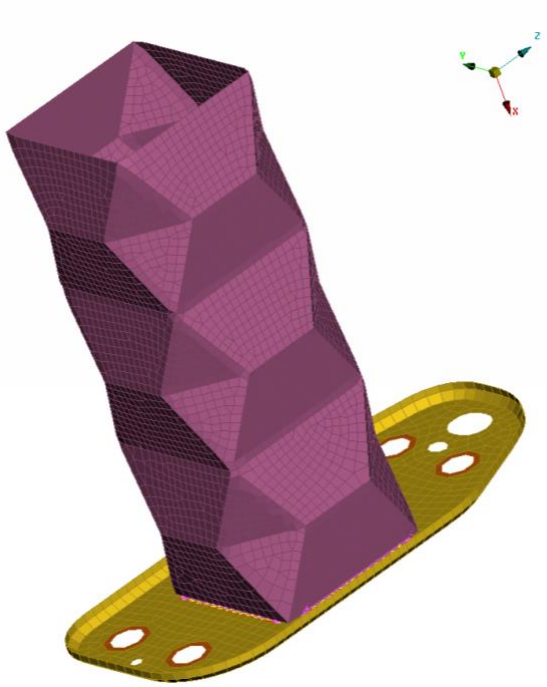

Figure 60 – Origami mesh

Source: Author's own work, 2017

As it shown in the picture, the external condition like the support plate or the spot-weld are equal to the previous simulation to maintain the same boundary conditions. After that, are made many simulations changing the specimen' thickness in order to compare the energy absorption varying only this important parameter. In *Figure 61*, there is the result of these simulations in a force-displacement graph.

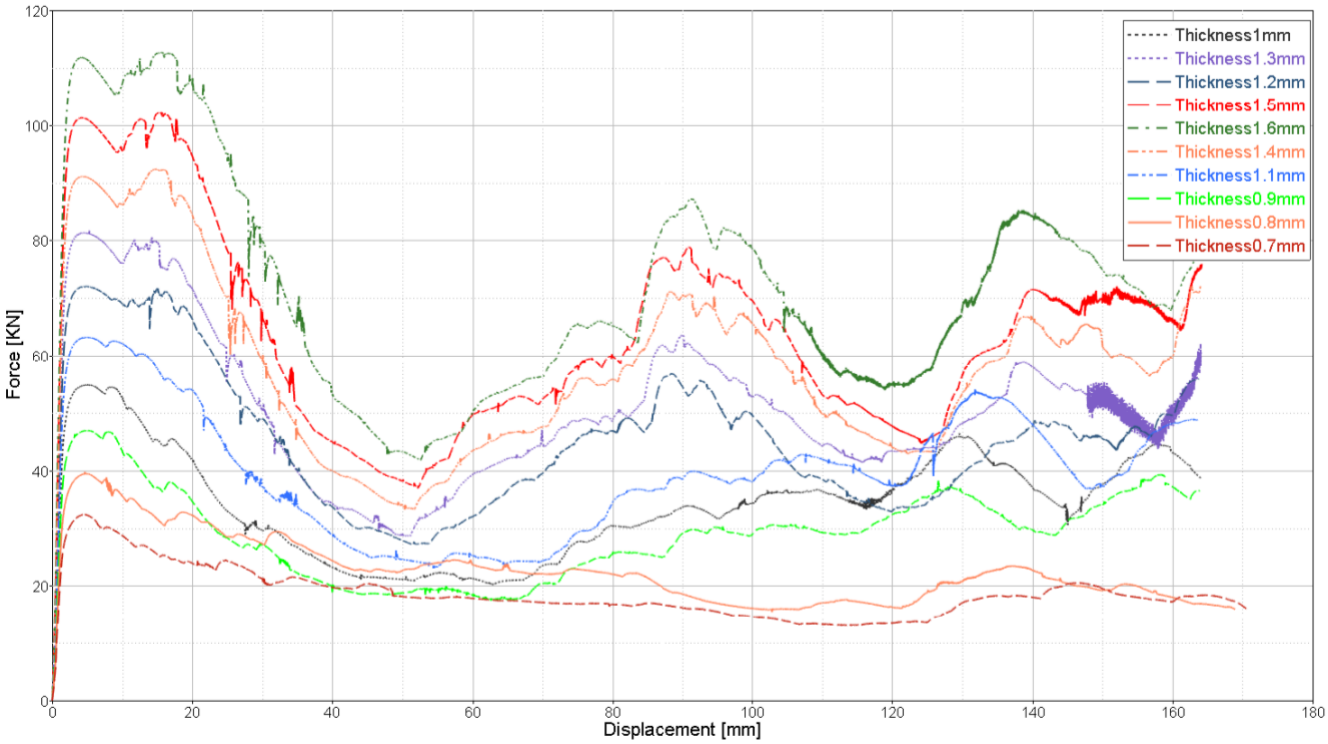

Figure 61 – Thickness comparison

Source: Author's own work, 2017

The range of thickness is done from 0,7 to 1,6 mm in order to understand if a thinner origami structure can guarantee the same characteristic of the general crash box. With this analysis, it was understood that below 0,8 mm of thickness the result is a buckling behavior without a good energy absorption, as can be seen in *Figure 62*.

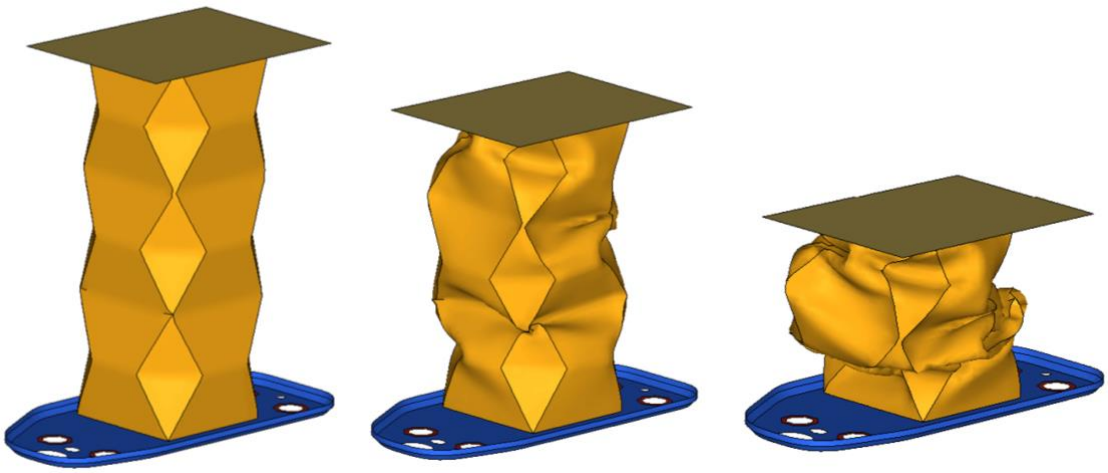

Figure 62 – Buckling behavior

Source: Author's own work, 2017

A very thin geometry can cause bending and so instability in the deformation and increasing the thickness instead is possible to see a correct collapse (*Figure 63*).

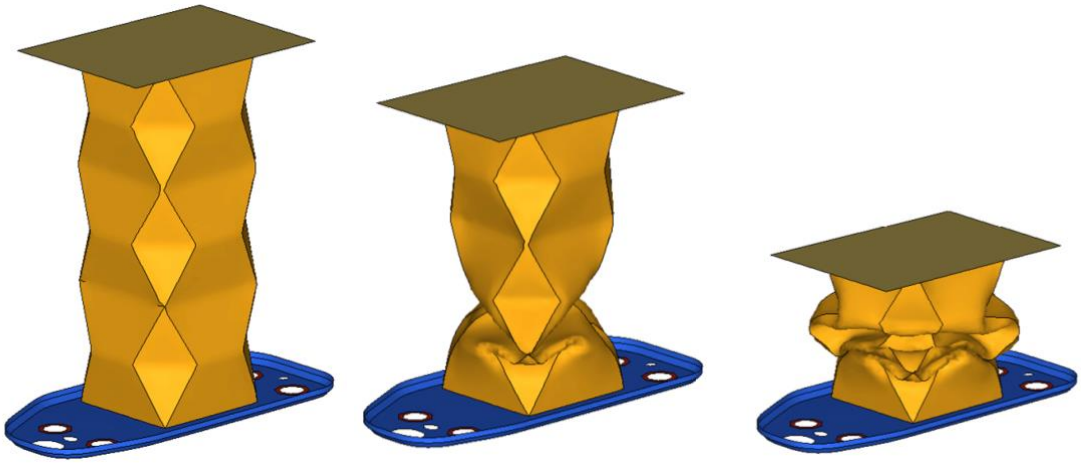

Figure 63 – Correct behavior (axialsymmetric)

Source: Author's own work, 2017

In this second serie of image, the thickness is 1.3 mm and it's easy to see that the lobes have a deformation in a perfectly axial way. Here in *Figure 64* is proposed another force-displacement diagram that underline the difference between the general crash box and the origami tube with the same thickness size.

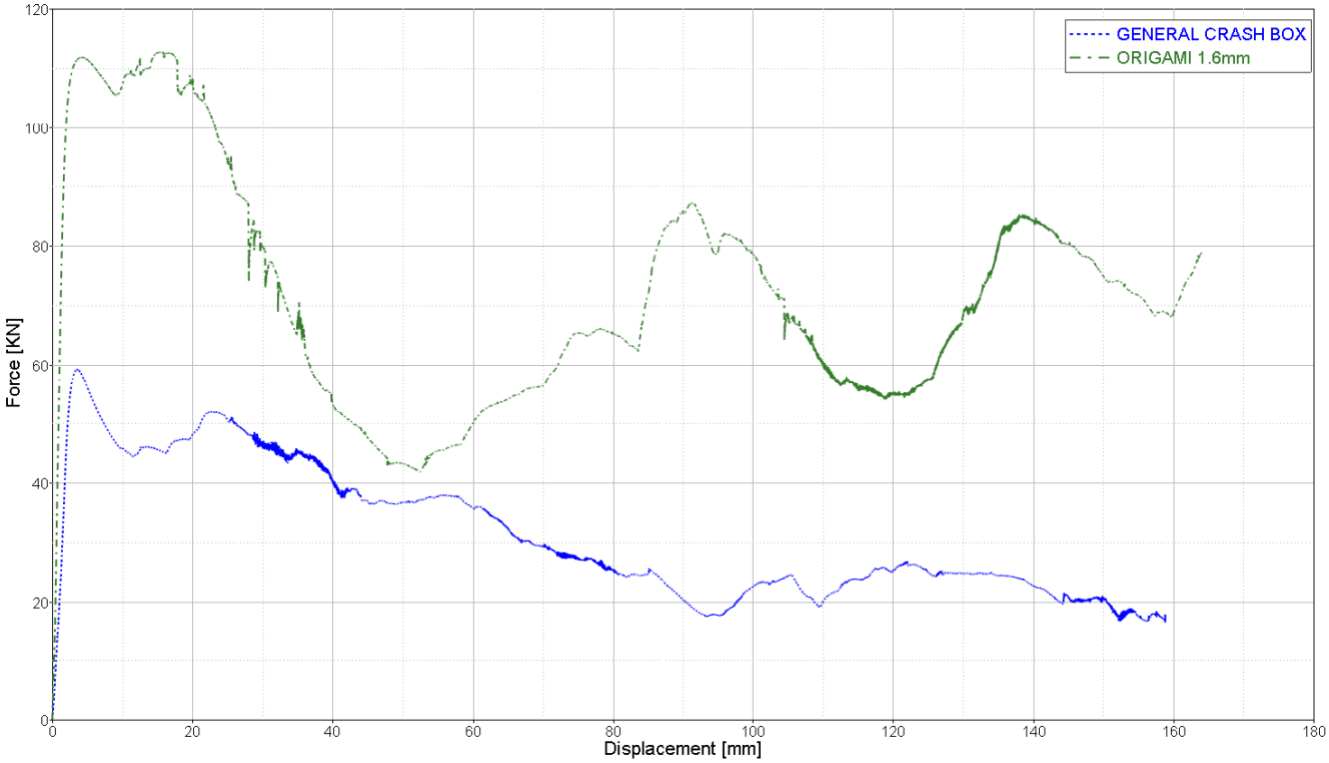

Figure 64 – General crash box vs origami tube

Source: Author's own work, 2017

Despite the greater energy absorption of this origami tube, it is clear from the graph above that the peak force is too high to satisfy the equation (54). So, it's used the origami tube with a lower thickness that guarantee the deformation before the rail and was analyzed the 1.3 mm thickness. With this size, the peak force is 81,3 KN as it's possible to see in the *Table 5* and so this crash box can be compared to the general crash box described before. The result is displayed in *Figure 65* in which are plotted the force-displacement graph and calculating the area under the curve is possible to obtain the energy absorption.

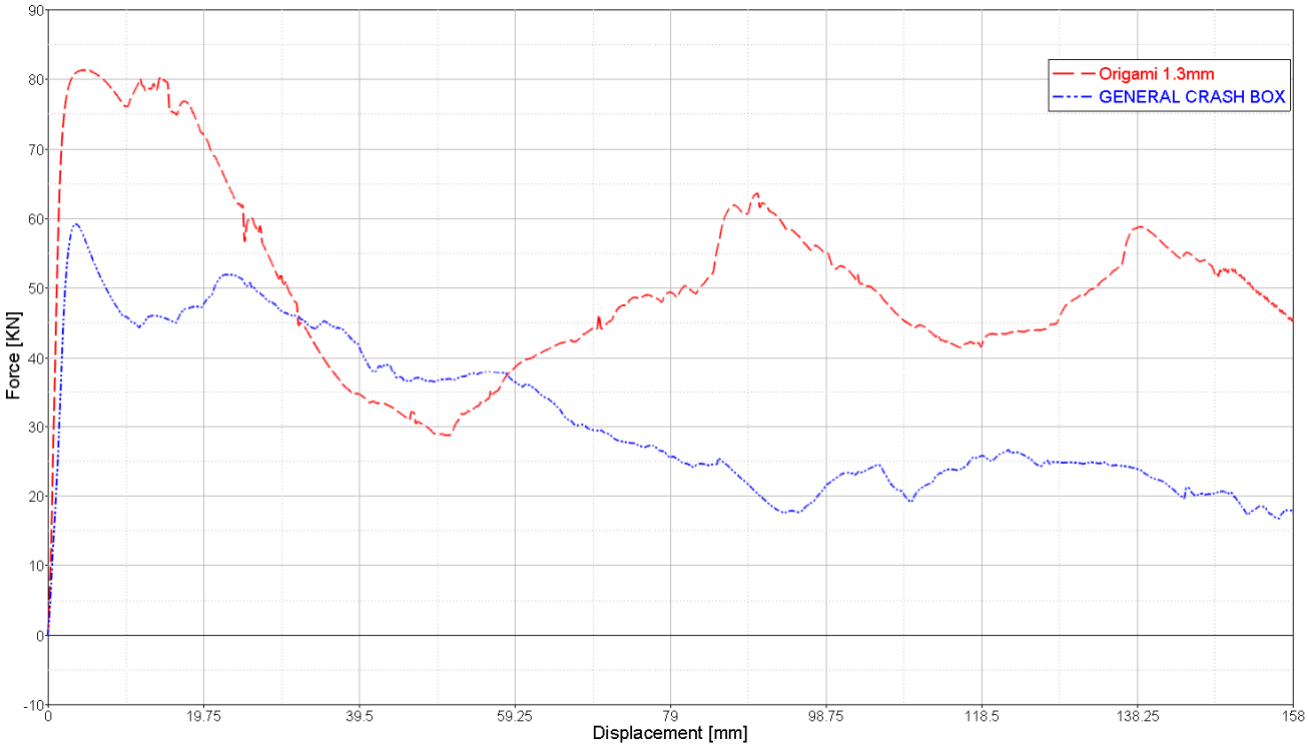

Figure 65 – General crash box vs origami tube with 1.3mm

Source: Author's own work, 2017

After this first analysis, due to manufacturing limitations, it had to change the material from DP600 to a FEE340 that is a high strength low alloy (HSLA) cold rolled steel. This steel is commonly used in the automotive industry especially for chassis or reinforcement components because of its good impact and fatigue strength.

The yield strength is equal to 338 MPa, the tensile strength is equal to 410 MPa and the other parameters like density, Young's modulus and Poisson's ratio are the same of *Table 2* for the dual phase material.

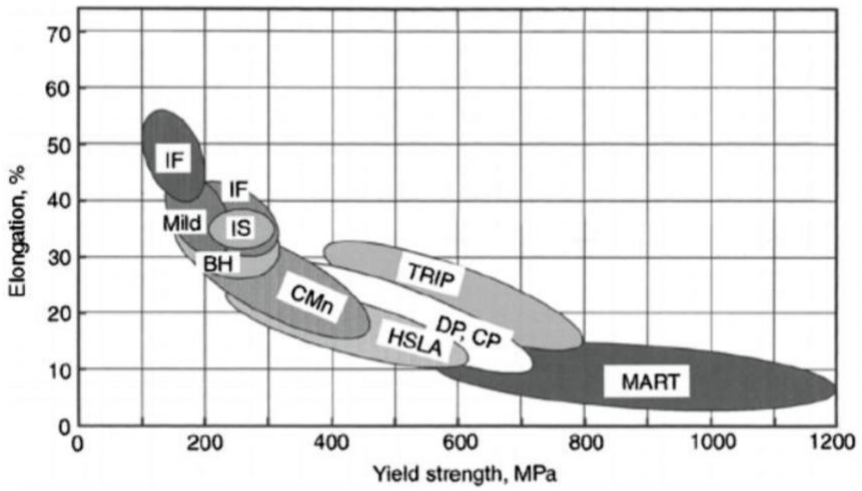

Figure 66 – Steel classification

Source: Matteis, 2017

As can be seen in the upper steel classification, HSLA is a less noble steel than the DP because the latter has higher work hardening rate, bigger ultimate strength and higher ratio of tensile strength over yield strength compared to a HSLA with a close value of yield strength. A dual phase steel has also a bake hardening effect which allows to increase the yield strength due to a high temperature of aging after a pre-strain induced.

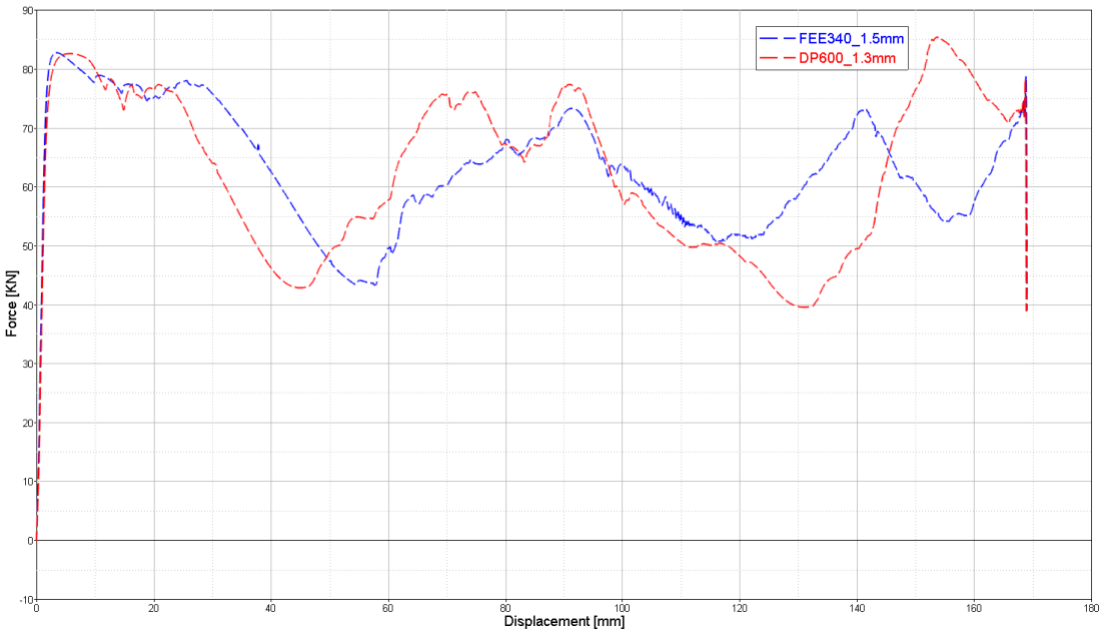

Figure 67 – DP600 and FEE340 comparison

Source: Author's own work, 2017

The *Figure 67* represents a comparison between the DP600 considered until now with 1,3 mm of thickness (red line) and the FEE 340 with 1,5 mm of thickness with a blue line. Fortunately, the curves are very similar and so is possible to study the same specimen with a 0,2 thickness bigger without major changes.

Another problem is encountered in the level of mesh accuracy. According to the Zhou et al. studies, there are basically three collapse mode. The first is the buckling behavior seen in *Figure 62*, the second is the symmetric mode (*Figure 63*) and the last one is the complete diamond mode. The first deformation mode is characterized by instability and guarantee the lowest results. The other two collapse modes are influenced by the ratio *l/t* as written in the chapter 2.5 and this is due to the fact that longer modules (*l/t*=60) are more sensitive to geometric imperfections and so the collapse doesn't guarantee the same energy absorption of the complete diamond mode [57]. This sensitivity has been found in two simulations with identical boundary condition and mesh size, just with a mesh reconstruction with particular attention in the lobe intersection and in the align of the elements across the mean surface as it underlined in the following images.

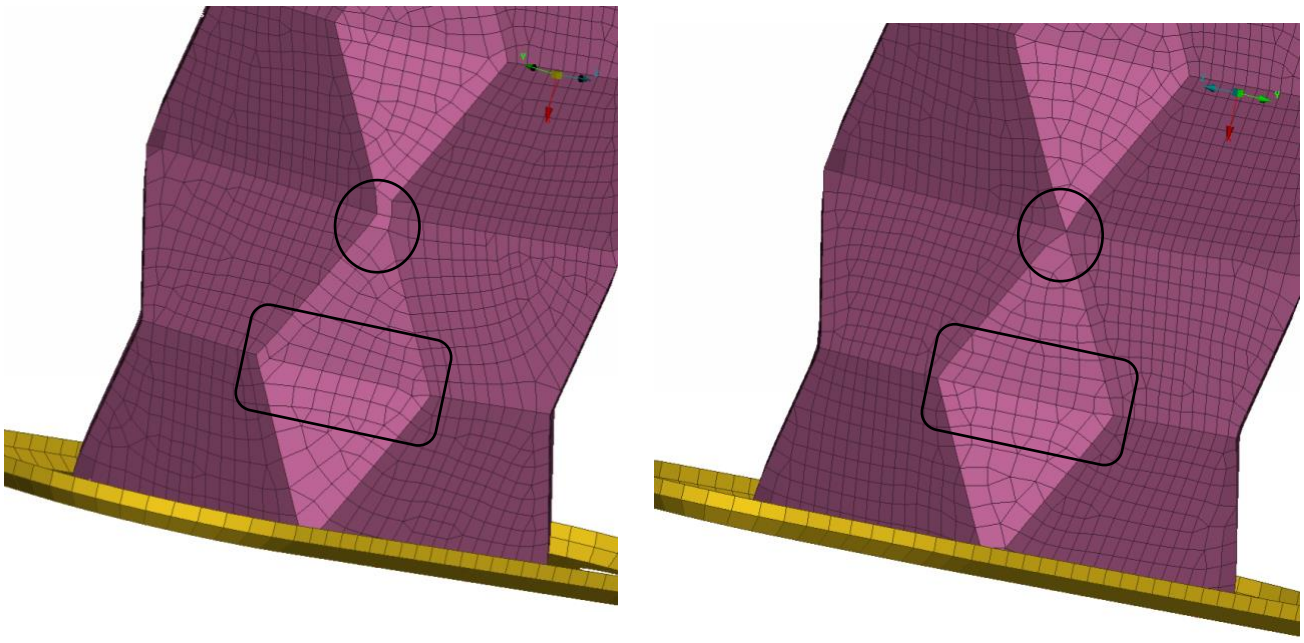

Figure 68 – Mesh improvement

Source: Author's own work, 2017

After the simulation of the two crash cans with different mesh, can be seen from the following series of images a completely different deformation.

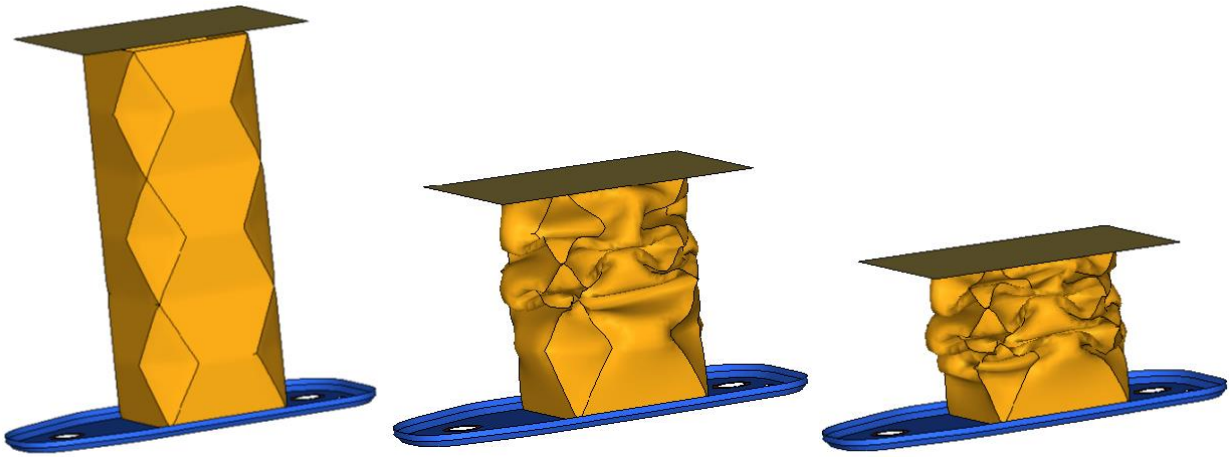

Figure 69 – Complete diamond mode

Source: Author's own work, 2017

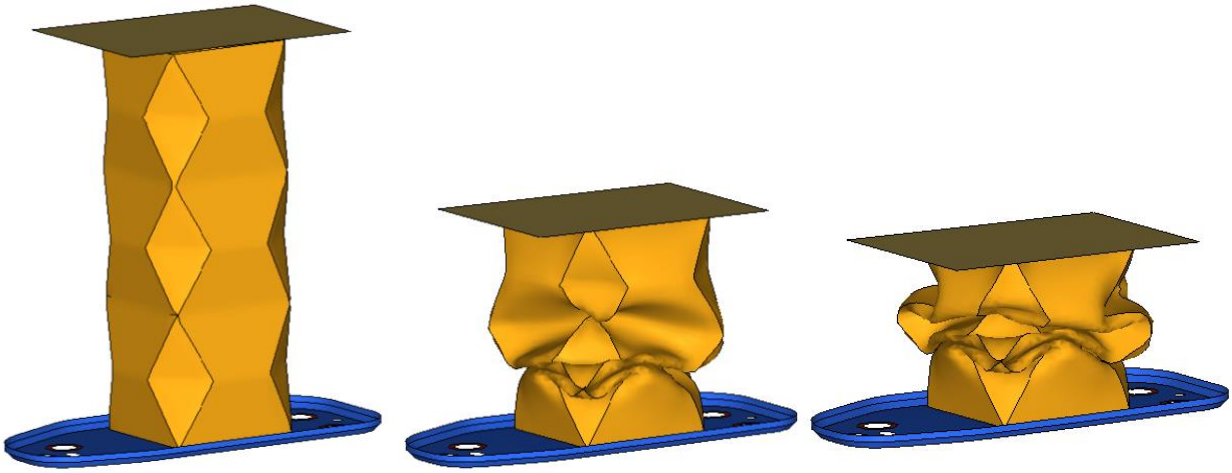

Figure 70 – Symmetric mode

Source: Author's own work, 2017

In the complete diamond mode all the lobes deform well and progressive in the collapse unlike the symmetric mode present only a half of lobes that develop in the right way.

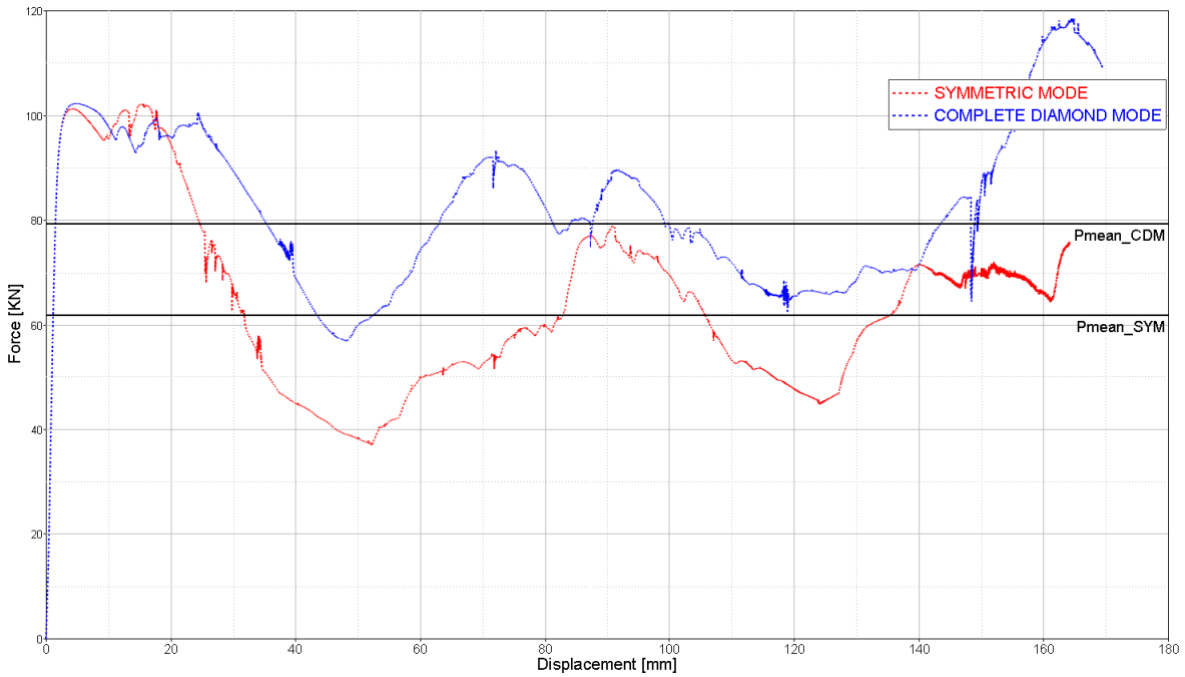

Figure 71 – Symmetric vs diamond mode comparison

Source: Author's own work, 2017

Comparing the area below the two curves, it was obtained that diamond mode absorbs 26% more energy than the symmetric one. The detailed analysis on the geometry parameters that influence the various collapse mode can be seen in the paper [57].

In the table are summarized the difference with respect to the thickness, the peak and the mean forces and also the energy absorbed by the origami type that is twice more compared to the traditional crash box. This preliminary result shows that it is possible to increase the energy absorption despite using a 0,3 mm lower thickness in the case of DP600 and so with this new technology is possible to obtain better result reducing also the raw material about 23 % or using a cheaper material as in the case of FEE340.

	GENERAL CRASH BOX DP600	ORIGAMI CRASH BOX DP600	ORIGAMI CRASH BOX FEE340
Thickness [mm]	1,6	1,3	1,5
Peak force [KN]	59,2	82,6	82,8
Mean force [KN]	29,5	60,6	61,5
CFE	2,0	1,36	1,34
Energy absorption [J]	4944	9806	9982

Table 5 – Numerical results

Source: Author's own work, 2017

4.3 Experimental methodology

4.3.1 General crash box

The first experimental test was made on the general crash box in order to understand the correlation between the simulation and the real quasi-static test. The experiment has been performed by a hydraulic testing machine with these characteristics:

- Maximum load 100 kN
- Maximum speed of actuator 1600 mm/s
- Maximum actuator stroke 300 mm

With this machine, it is possible to record the actuator displacement and the force during the deformation in order to obtain a load-stroke curve for each test. The analysis was carried out with a crosshead velocity of 2,5 m/min that is the same of the simulation in order to obtain a regular crushing of the folds.

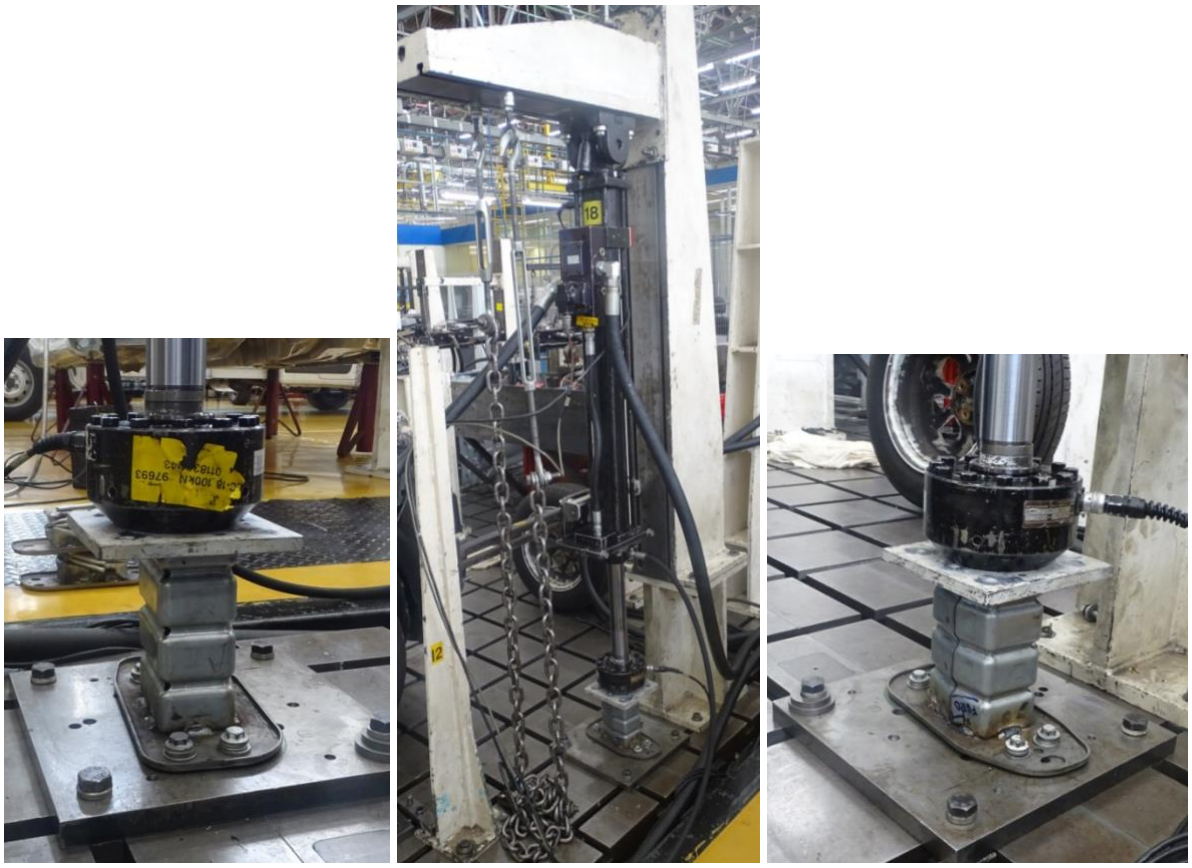

Figure 72 – Experimental setup

Source: Author's own work, 2018

In the figure above, it's shown a thick plate connected to the actuator that thanks to its movement compresses the crash box. The specimen is fixed with four bolts to the floor to maintain it in a stable position and avoid bending.

In a first test to set the machine, it has been found that reaching the 80% of the total height of the specimen, the actuator started to suffer by the force increase given by the approaching to a rigid wall. So, the total actuator stroke has been set 80 mm and no instability was encountered until this length.

4.3.2 Origami crash box

The manufacturing of the specimen, as always happens in the prototype construction, has a different process compared to the definitive manufacturing. The technique used in the building of these ten crash cans is the sheet metal stamping that is quite similar to the real mass production except for the cutting process and for the welding that isn't automated.

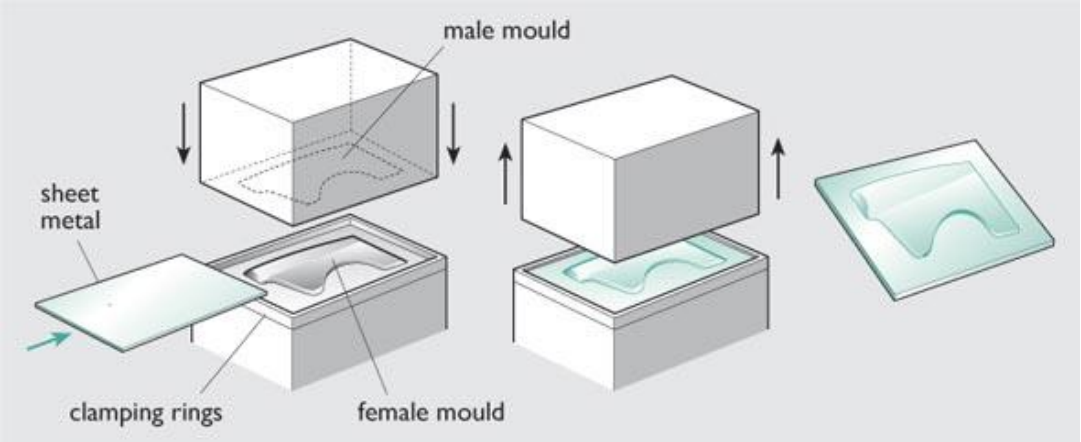

Figure 73 – Stamping process

Source: http://www.learneasy.info/MDME/MEMmods/MEM30007A/processing/processing.html

In *Figure 73* is presented a traditional stamping process that is often applied in the automotive companies to produce high volume of sheet metal components. The male mould that is also called punch is usually linked to the press that is the responsible to generate the right closing force. The male module, in addition to shape the blank, in an automatized process does the punching process that consist in the sheet metal cutting. The process consists in putting the sheet metal in the machine and when the male and the female moulds are in a close position, they form the blank according to the net shape. In a press are also present guide pins that allow to have an alignment between the male and the female part of the die. In the construction of origami specimens there was a single operation and so every press stroke produces a part but the stamping process could be also done in more steps.

Here are proposed the two halves of the mold that allowed to shape the specimen geometry with the parameters proposed in the *Table 3* except for the thickness. With this tool was possible to perform a cold forming of the 1,5 mm sheet metal with the FEE340 material.

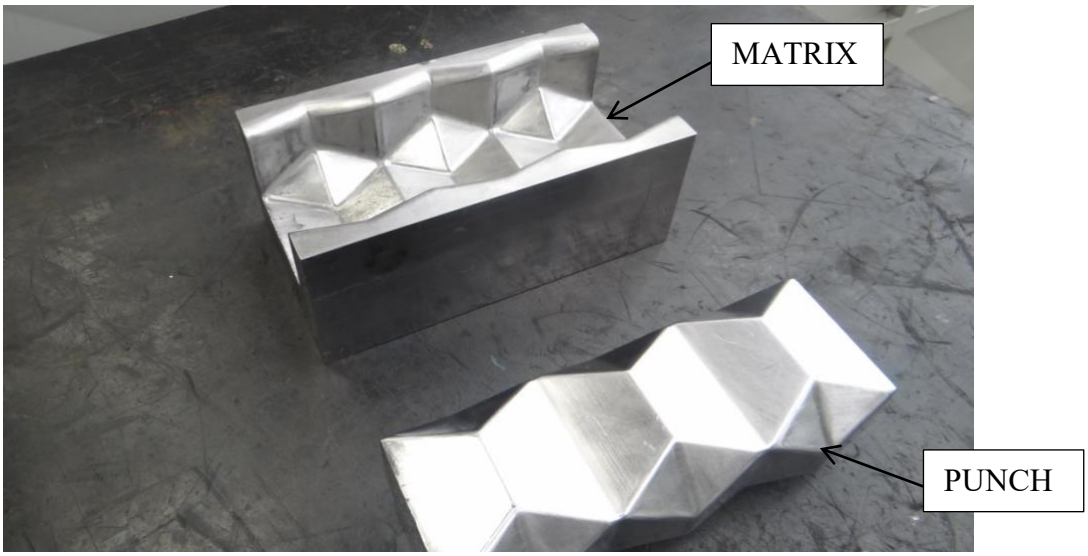

Figure 74 – Stamping tools

Source: Author's own work, 2018

After a stamping of the first half, the extra part of the sheet metal has been manually cut and since the geometry is symmetrical for the other half the same procedure was followed.

Before deciding the welding type, has been done also an experimental test in order to understand the bonding effect on the specimen deformation. The test simulates a weld bead of approximately 35 mm in each side of the module leaving a space in the mean surface both because is not possible to do a continue MIG welding and because this edge has to be free to deform.

The weld beads are simulated in two ways: the first with rigid element with the command seam line in Ansa (*Figure 75* left-hand side) and the other is to double up the thickness in the welding area changing the mesh properties but leaving the same material plasticity model, that is the MAT24 described in the chapter 4.1.5. This combined approach was carried out because the weld bead cannot be considered as a rigid body and also for the problem of different thickness between the MIG welding region and the 1,5 mm thickness of the specimen that cannot be neglected.

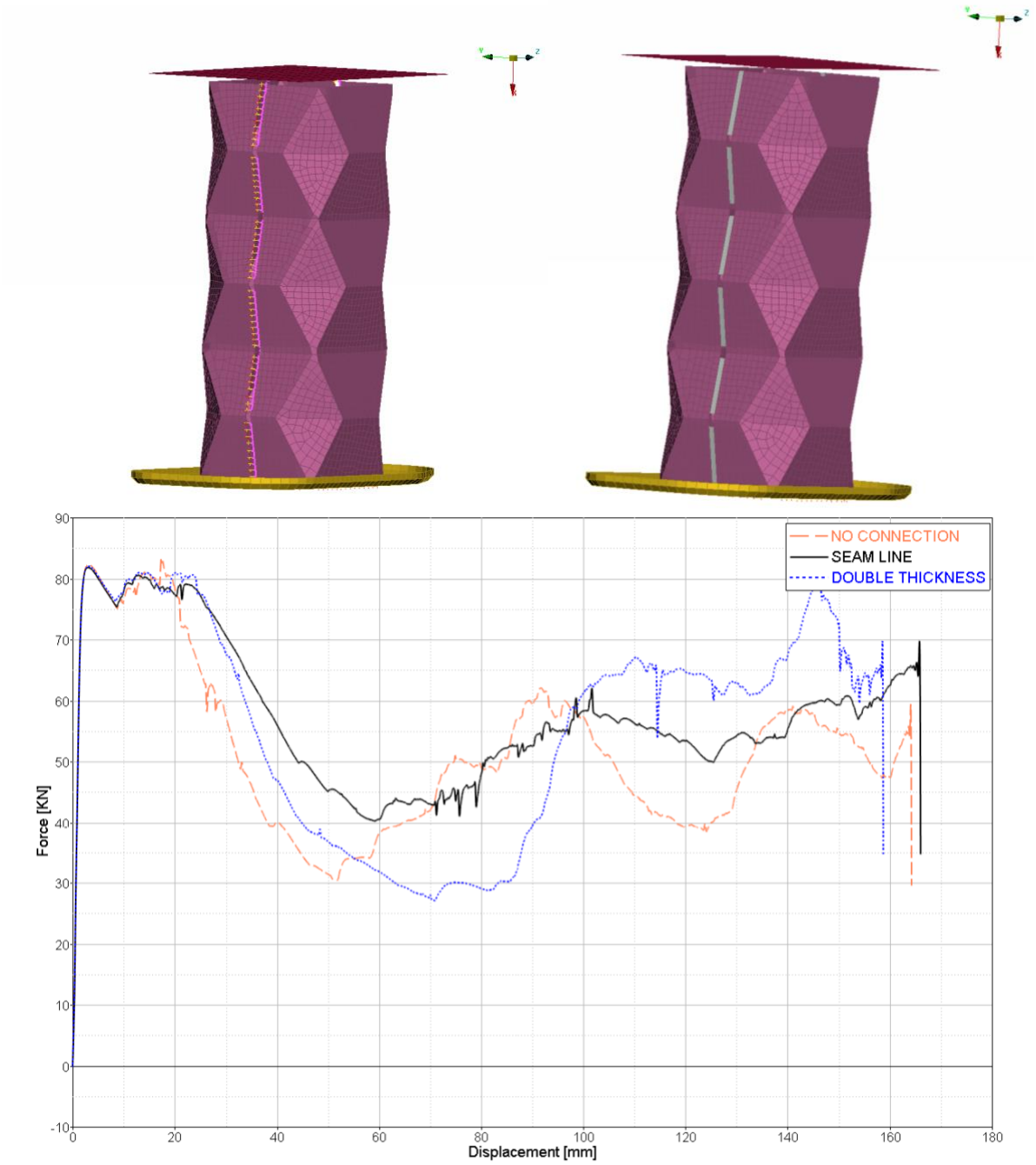

Figure 75 – Welding analysis

Source: Author's own work, 2018

The results of the two simulations allowed us to understand that MIG welding, even if not continuous, did not greatly influence the behavior during deformation. From the graph can be seen, however, that the curves with the welding simulation lose the wave pattern between

subsequent lobe typical of the origami geometry and therefore in comparison with the physical test it was preferred to use the model without welding.

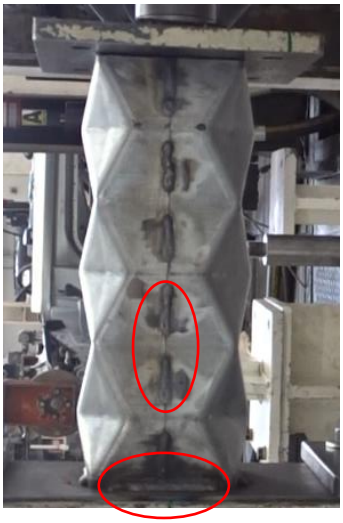

Figure 76 – Welded parts

Source: Author's own work, 2018

Finally, the two halves are connected with a MIG welding as shown in the figure above and also the crash can base is welded to a plate with a 3 mm of thickness to facilitate locking operations of the specimens. Here is proposed the final shape of a specimen.

Figure 77 – Final specimen

Source: Author's own work, 2018

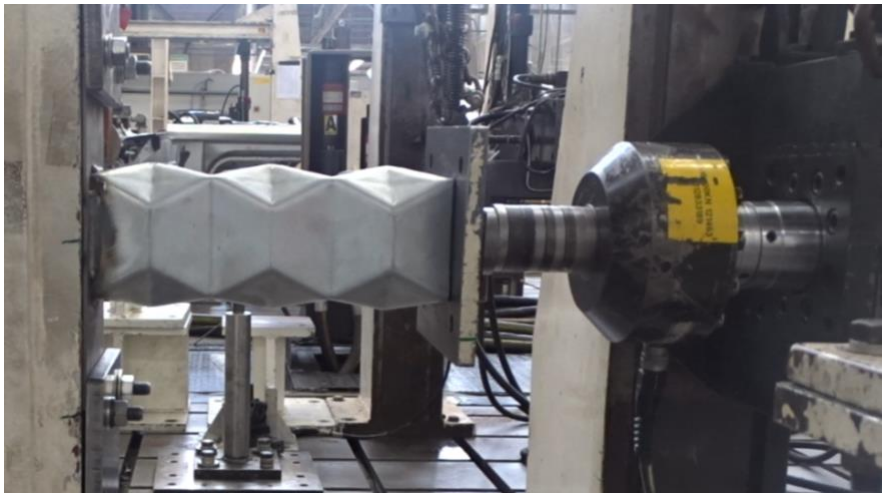

Figure 78 – Experimental setup of origami crash box

Source: Author's own work, 2018

In the figure above is proposed the machine that has the same characteristics of the one used for the general crash box test but, in this case, the actuator works horizontally and there is a more rigid structure in order to withstand the higher peak force of these specimens.

5 – RESULTS

5.1 General crash box

In the following image, there is the force-displacement comparison of the seven general crash box subjected to the test. The simulation is represented with a red line and has a peak force of 60 kN, a mean force of 55 kN and a 4413 J of energy absorption. Doing the average of the other seven curves of the real test, the peak force reaches the value of 53,9 kN that gives a 90% of correlation with the simulation, a mean force of 49,2 kN that is 89% of correlation and a 4037 J of energy absorption that is a correspondence of 91%. All the results divided by each test are proposed in the *Table 6*.

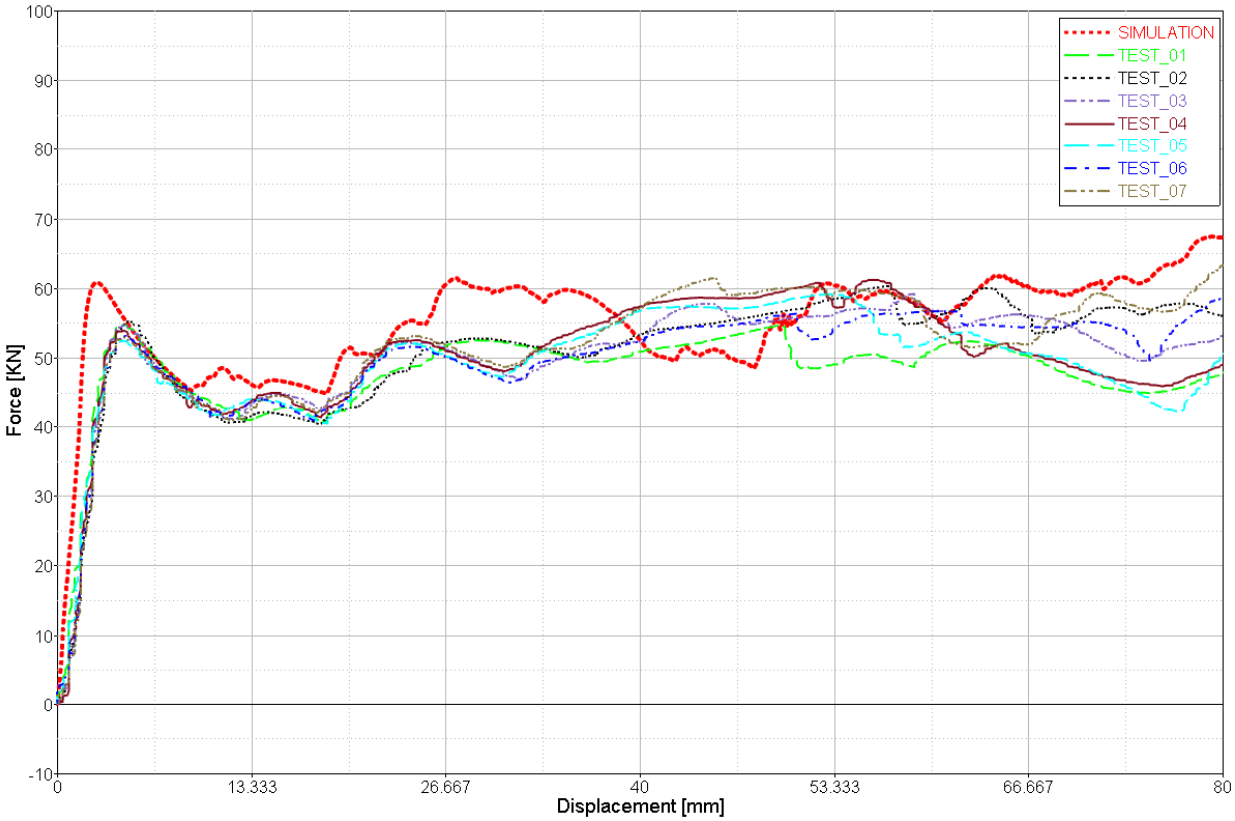

Figure 79 – Physical test results

Source: Author's own work, 2018

As can be seen from the graph, there isn't a high difference between the peak and the mean force and this is due to a low height (163 mm) of the specimen because there is a big influence caused by the proximity of a rigid wall.

The best correlation was found with the sixth physical test and here below are proposed the load-stroke curves between this test and the simulation and the image comparison in four different moments of time during the deformation.

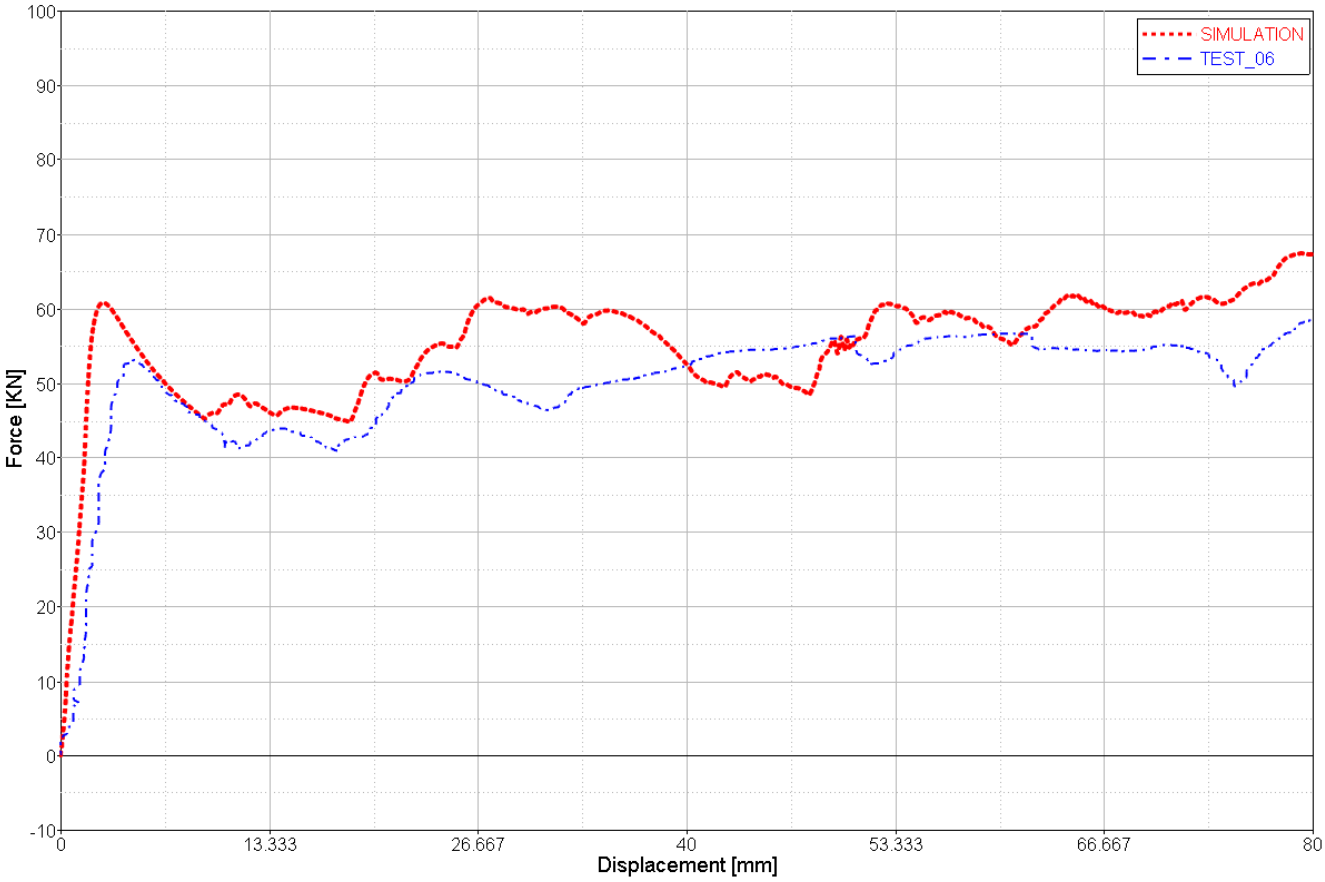

Figure 80 – Best curve correlation

Source: Author's own work, 2018

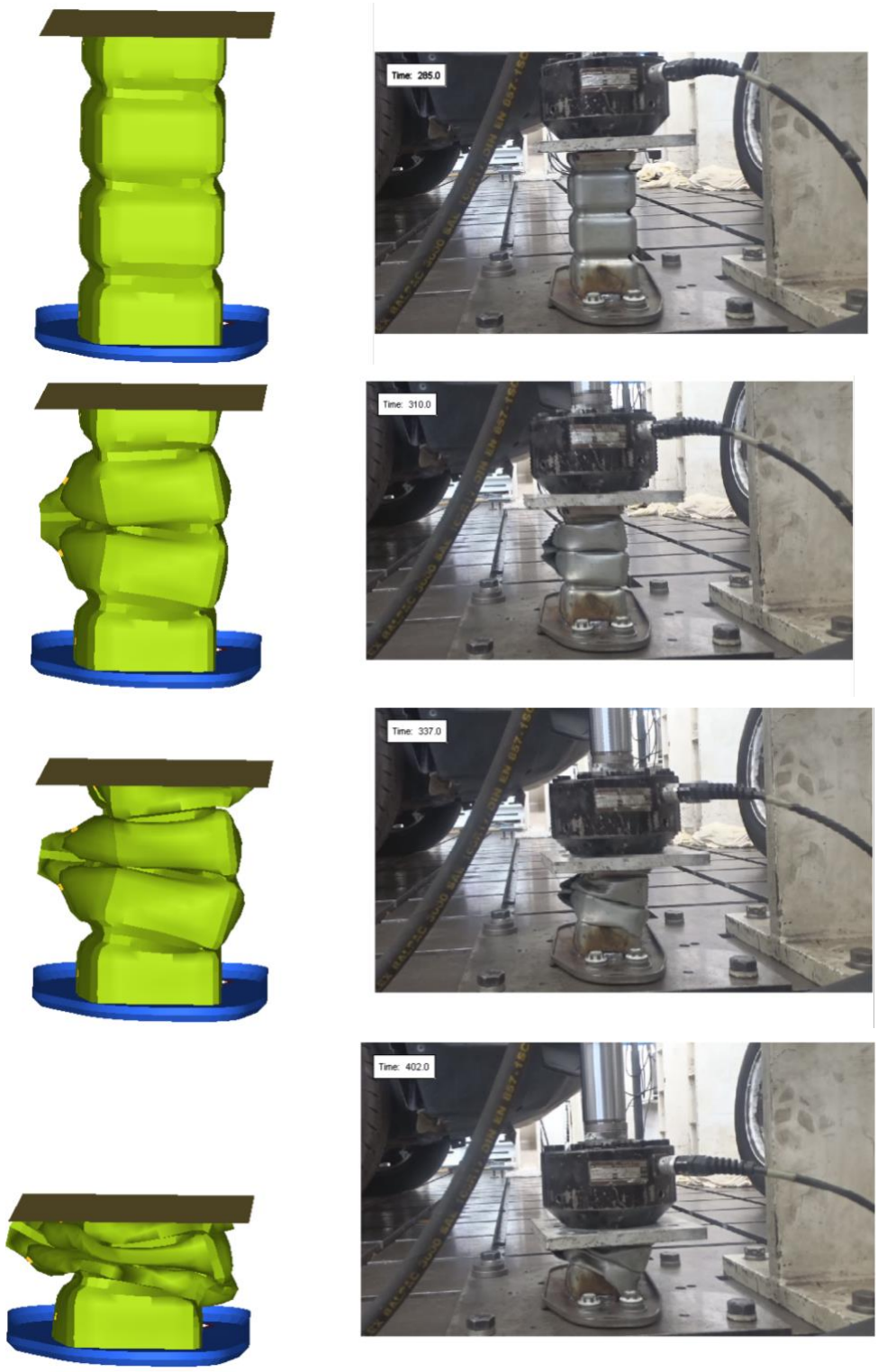

Figure 81 – Crushing sequence

Source: Author's own work, 2018

Here in the table, all the results between the various specimens are summarized and this confirms the great correlation seen during the compression test. Can be concluded that the simulation is reliable and all the consideration described in the chapter 4.1 like the choice of a certain element formulation, the material and the contact models have been confirmed.

	Pmean [KN]		**Pmax [KN]**		**Energy absorption [J]**	
Simulation	55		60		4413	
	Pmean [KN]	**Ratio**	**Pmax [KN]**	**Ratio**	**Energy absorption [J]**	**Ratio**
TEST_01	47,5	86%	54,7	91%	3833	87%
TEST_02	50,5	92%	55,4	92%	4092	93%
TEST_03	49,2	89%	54,7	91%	4046	92%
TEST_04	49,1	89%	53,9	90%	4037	91%
TEST_05	49,1	89%	52,4	87%	3958	90%
TEST_06	49,8	91%	52,3	87%	4018	91%
TEST_07	51	93%	52,9	88%	4168	94%
MEAN	49,2	89%	53,9	90%	4037	91%

Table 6 – General crash box results

Source: Author's own work, 2018

5.2 Origami crash box

Subjecting to a quasi-static test also here with a 2,5 m/min velocity the 10 origami specimens described in the chapter 4.3.2, are obtained these kinds of deformations plotted in the force-displacement curves.

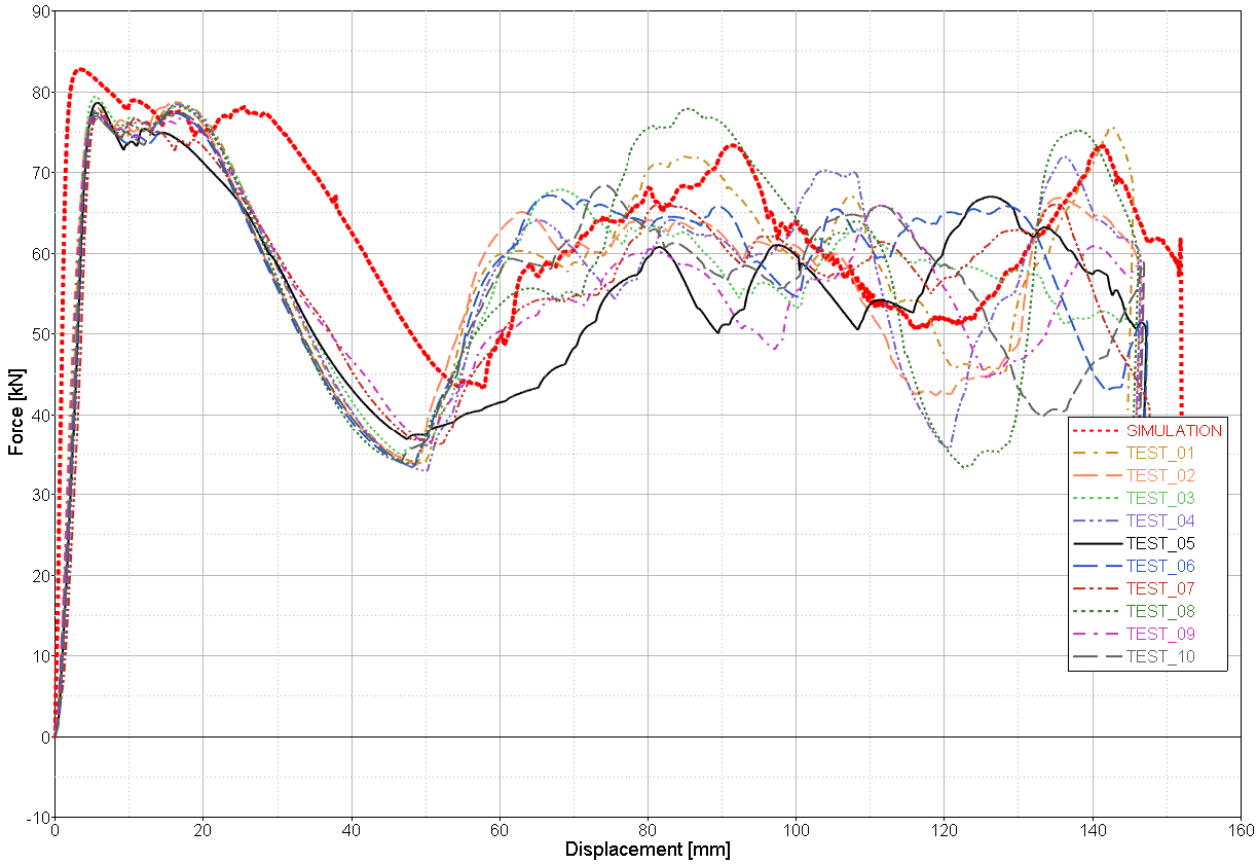

Figure 82 – Comparison during the origami test

Source: Author's own work, 2018

It's quite simple to identify three peaks in most of the curves and the distance between them represents more or less the height of each module. Some test like the third and the fifth, has a buckling deformation and this can be already seen in the graphs and then it's confirmed in the images presented further on.

The biggest difference between the simulation and the physical test is the first valley that is shifted to the left in every test and this can be caused by the lack of imperfection in the model simulation that is a single piece or, looking at the test video due to the high peak force the seal column moves a little; in fact only in the first lobe formation there is this alteration and then the curves return to be similar.

Figure 83 – Final deformation of all the specimens

Source: Author's own work, 2018

In this group of images are presented the final deformation of the ten specimens and, despite the values of energy absorption and the other characteristic point in the curves are quite similar, the way of collapse is very different. Starting from the two specimens that had a failure, it is clear

that the sample 3 and 5 had a buckling behavior. As it is written in the manufacturing description, the weld beads are made manually and surely there are some difference between the two sides. In these two experiments, it happened that a welding failed in one side and so the specimen collapse in that region.

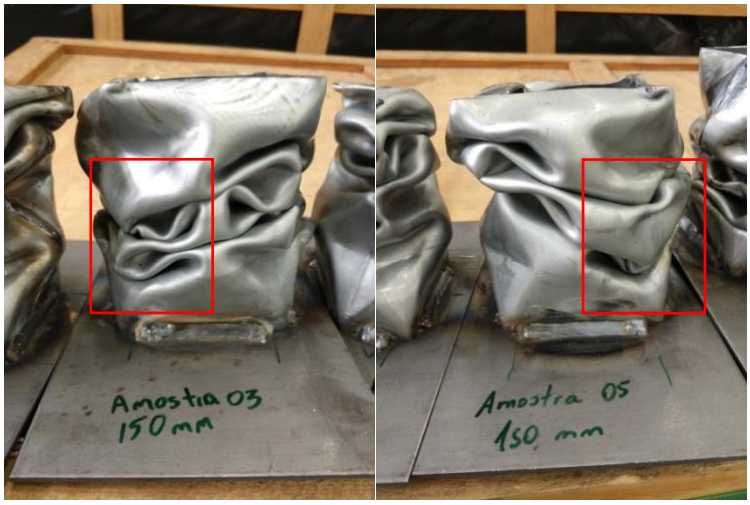

Figure 84 – Buckling behavior

Source: Author's own work, 2018

From the *Figure 84* can be noted that the specimen 3 had a failure in the left-hand side and the specimen 5 in the other side. Fortunately, these are the only two tests with this kind of problem and the positive point is that, despite this buckling deformation, there isn't a high difference about energy absorption, but it's only found a flatter curve without a distinction between peak and valley. Here are presented the specimens 2, 4, 6, 7 and 9 that have the nearest deformation according to the theoretical diamond mode found in the simulation.

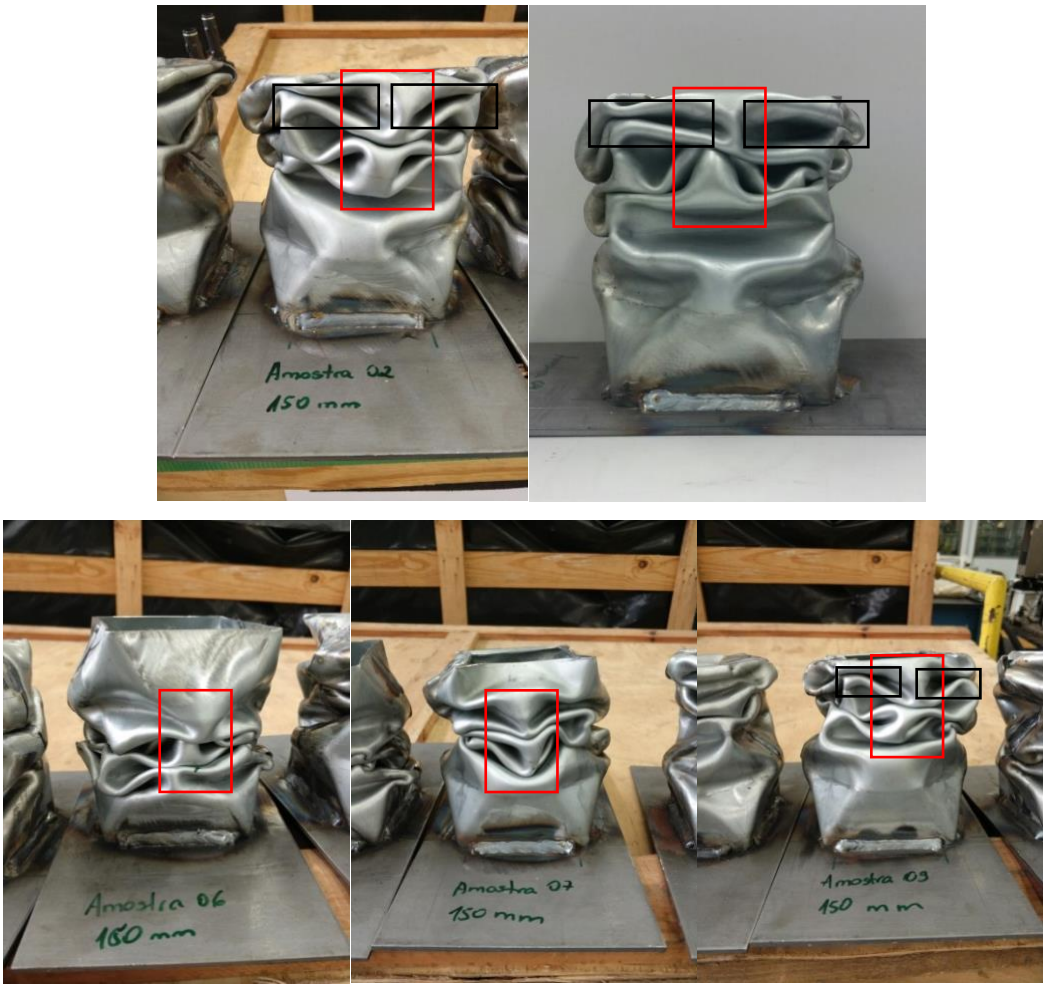

Figure 85 – Super folding elements

Source: Author's own work, 2018

In the images above, it is highlighted in red the presence of regions that non-deform and doesn't contribute to the plastic deformation ensuring solidity to the structure. The best result is obtained with the fourth specimen in the figure at the top right, in which can be seen the presence of two super folding elements next to each lobe. These plastic folds are already described in the chapter 2.2 here are underlined with black boxes and in addition it's possible to see that all the lobes deform well during the compression test.

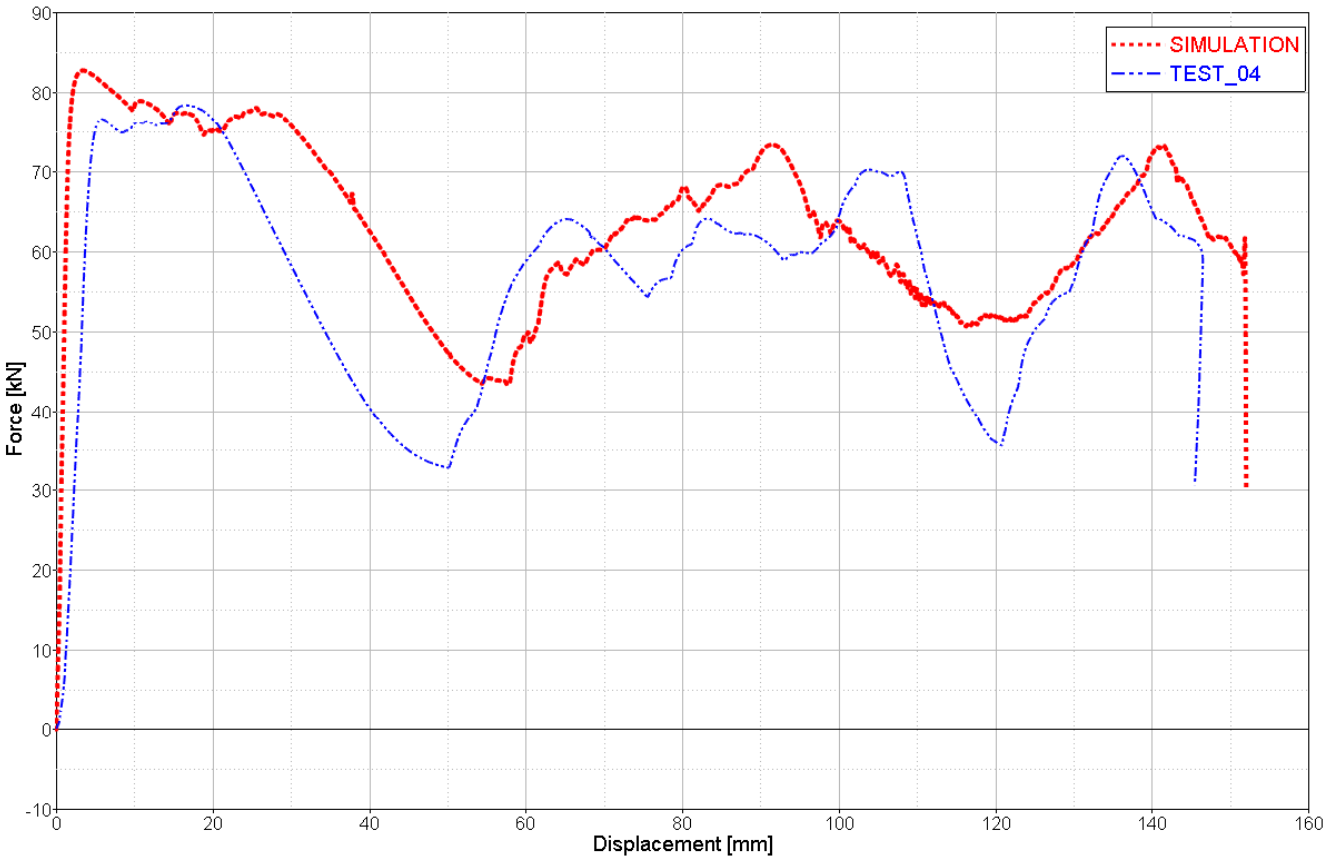

Figure 86 – Comparison TEST_04 vs simulation

Source: Author's own work, 2018

Here is plotted the comparison with the fourth specimen force-displacement curve with the simulation and the wave pattern is very similar just with a shift of the first valley to the left as it found in every test. In *Figure 87* the various views of the fourth specimen at the end of the compression test can be seen including the top view.

Figure 87 – TEST_04 results

Source: Author's own work, 2018

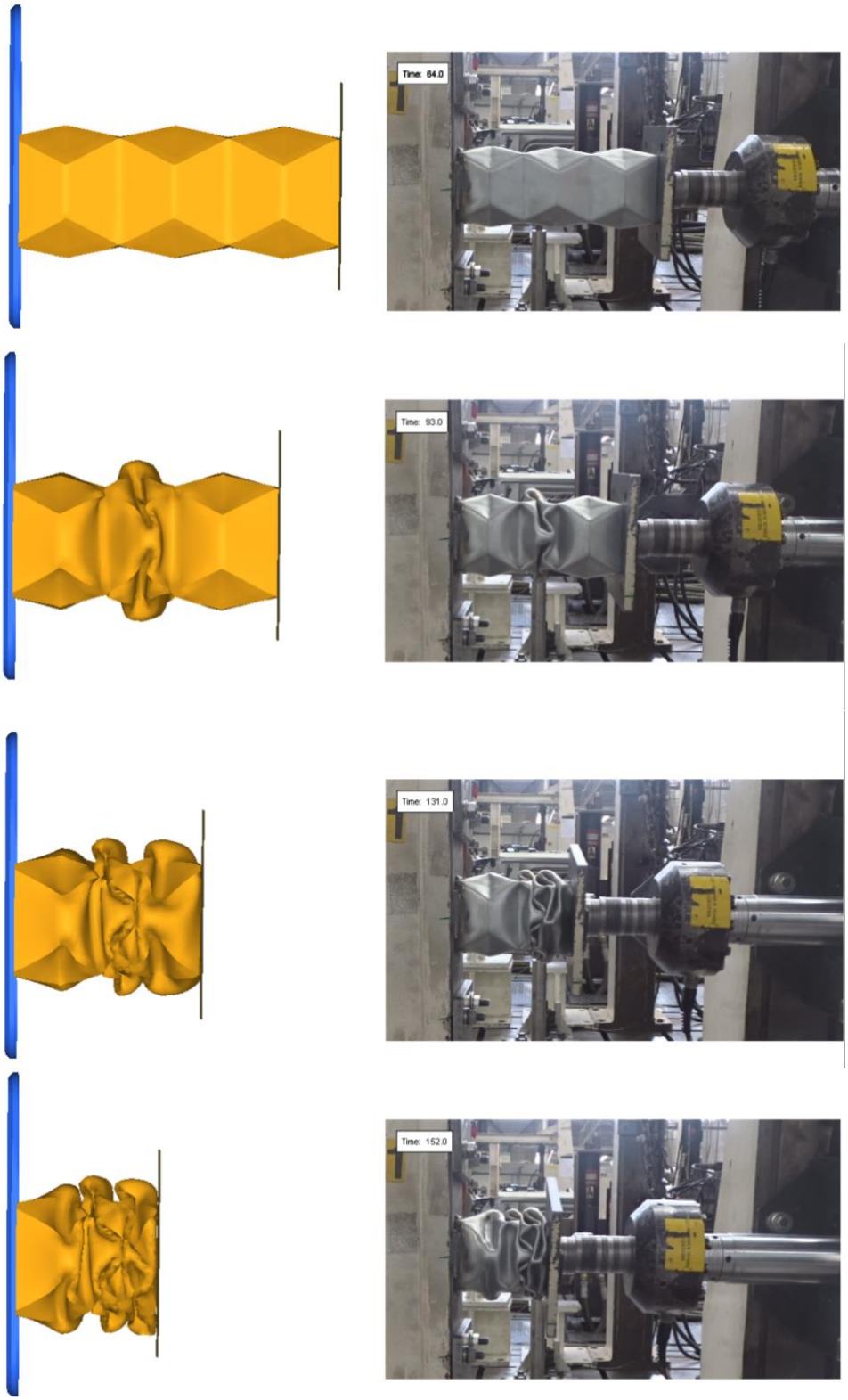

Figure 88 – Origami crushing sequence

Source: Author's own work, 2018

As can be seen from the series of pictures during the experimental test, the plate at the bottom of the actuator tend to rotate a little bit because, although the machine is made to move only in an axial direction, can be an influence of the superficial friction between the specimen and the rigid plate. The samples 1 and 10 suffered most from this phenomenon and so the regions that perform axially like in the other test are subjected to an additional torsion. This extra torsional deformation is another way of energy dissipation and so from the point of view of energy absorption guarantee better result, but it worsens the geometric behavior during the deformation compared to the complete diamond mode.

Finally, it's proposed a summary table with of all the test and the simulation data in which the various results are easy to compare.

	Pmean [KN]		**Pmax [KN]**		**Energy absorption [J]**	
Simulation	61,7		82,7		9150	
	Pmean [KN]	**Ratio**	**Pmax [KN]**	**Ratio**	**Energy absorption [J]**	**Ratio**
TEST_01	58,8	95%	78,6	95%	8540	93%
TEST_02	56,7	92%	78,5	95%	8257	90%
TEST_03	57,4	93%	79,3	96%	8360	91%
TEST_04	57,1	93%	78,4	95%	8293	91%
TEST_05	54,8	89%	78,6	95%	7971	87%
TEST_06	58,3	94%	77,4	94%	8476	93%
TEST_07	56,8	92%	77,5	94%	8281	91%
TEST_08	58,1	94%	78,1	94%	8408	92%
TEST_09	55,4	90%	77,6	94%	8071	88%
TEST_10	55,9	91%	77,4	94%	8127	89%
MEAN	56,95	92%	78,25	95%	8287	91%

Table 7 – Origami crash box results

Source: Author's own work, 2018

5.3 Numerical optimization

It was implemented an optimization algorithm to understand the influence of geometry changes on energy absorption. First of all, a surface moprh has been made with the software Ansa described in the numerical devices paragraph 4.1.1.

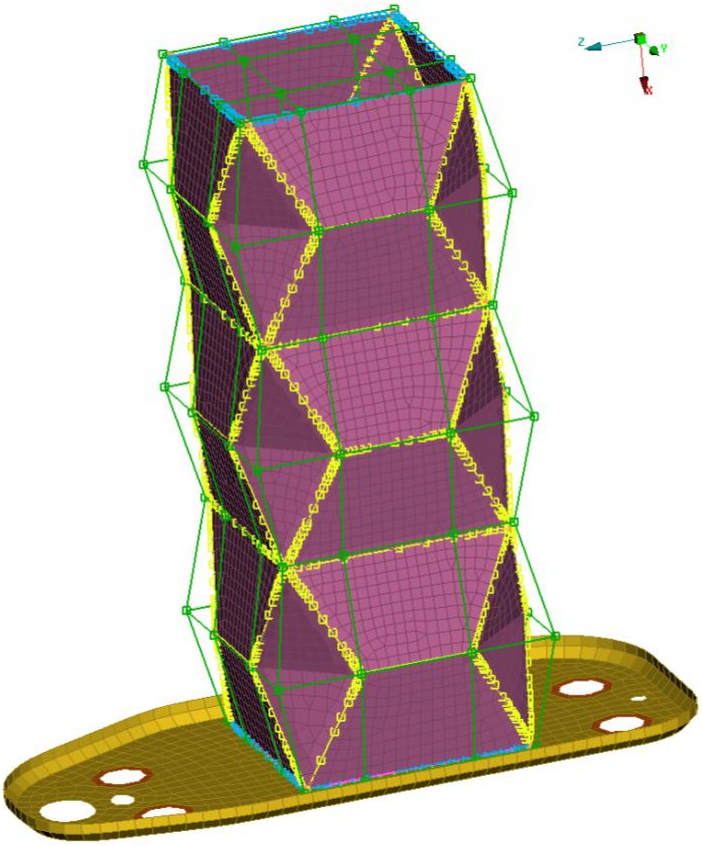

Figure 89 – Morph

Source: Author's own work, 2018

The parameters morphed are the height and the width where H morphs the height of each module and D parameter take into account the width dimension of the lobe and also the width of the module mean surface. The base width of the module remains constant and thereby also the base area does not change in value. Moreover, has been set a condition to link the change in width of the lobe and the height modification following the equation (55) in order to maintain the right inclination angle.

The software used to implement the optimization routine is Isight from the Dassault Systemes which can combines different disciplinary models and applications components together in a

unique simulation process cycle, can automate the process flow, give results in the 3D graph and find the optimal geometry imposing the desired constraints.

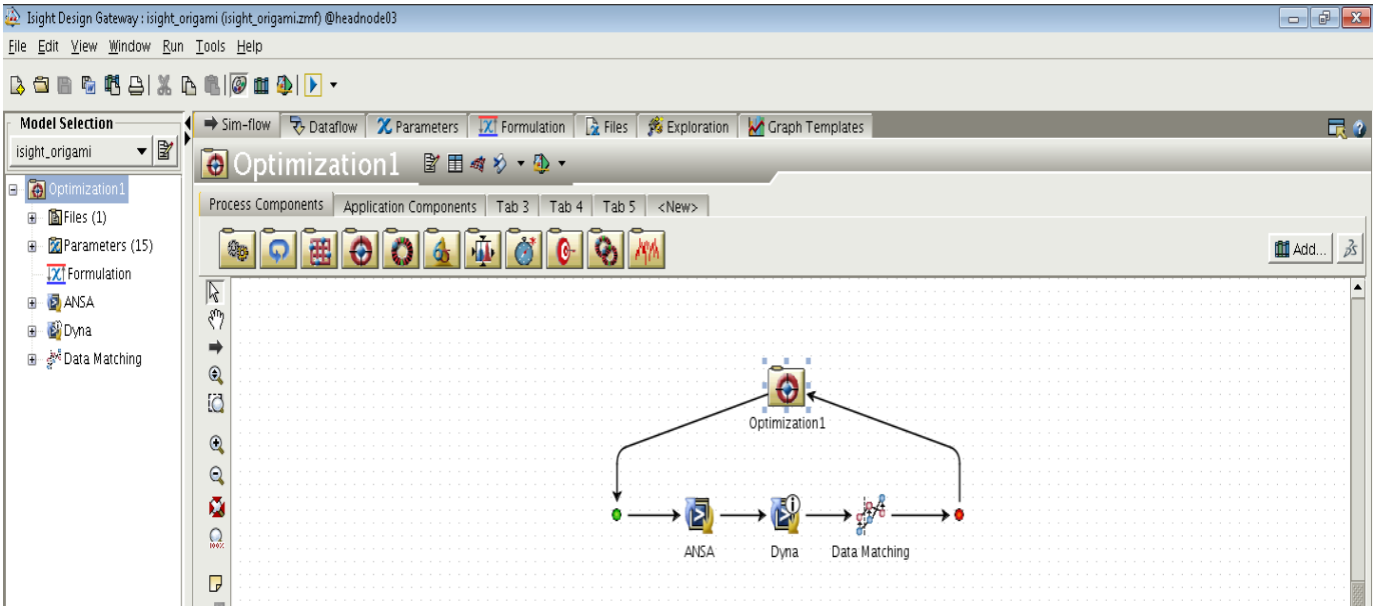

Figure 90 – Optimization cycle

Source: Author's own work, 2018

The optimization flow plotted in the image above consists in:

- Ansa morphing geometry with H and D parameters;
- LS-DYNA solver;
- Data Matching that compares the output of the *secforc* from the LS-DYNA software with a target curve.

In *Figure 91* the target curve is shown in black and the red line represents the force value during compression.

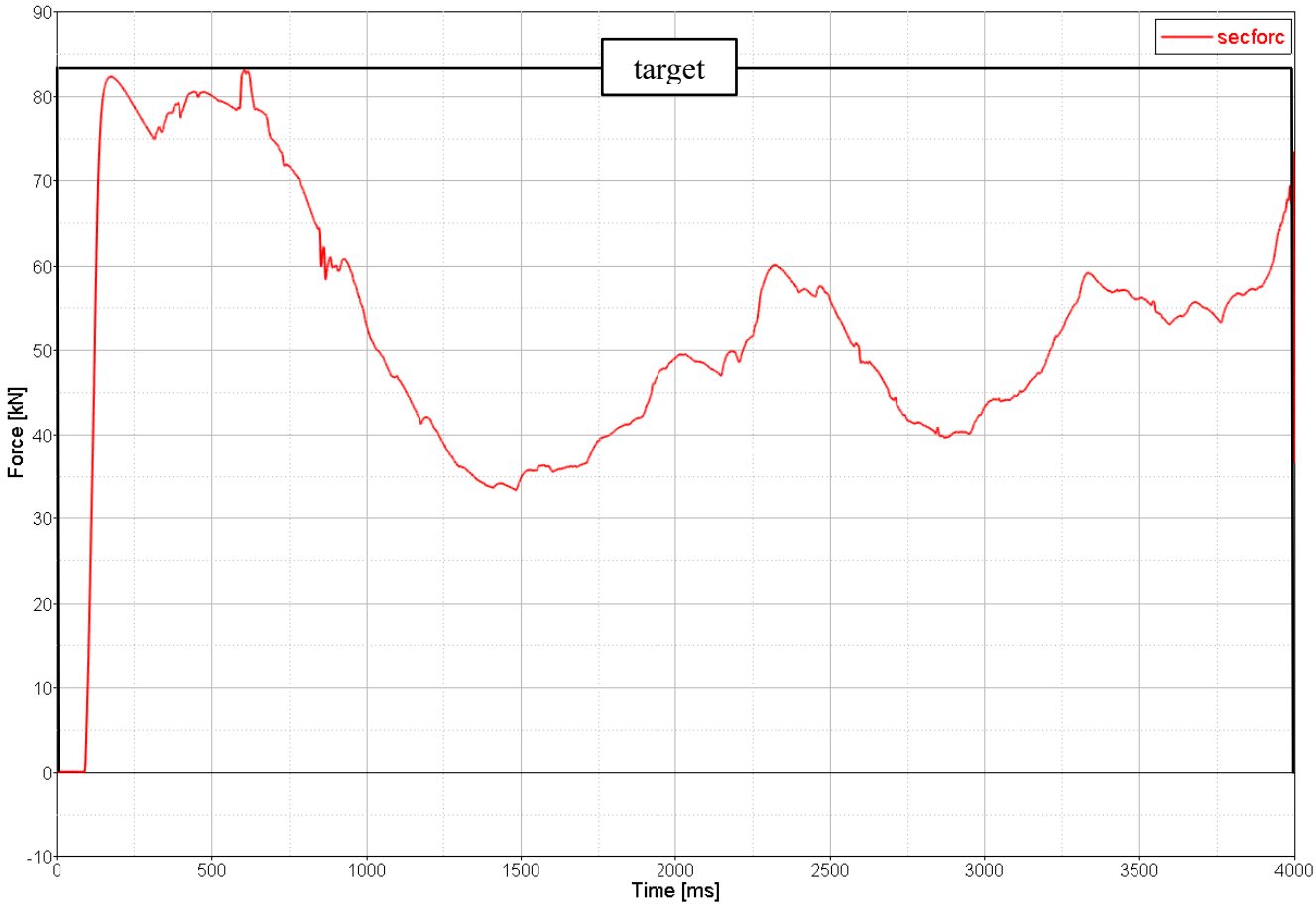

Figure 91 – Target function

Source: Author's own work, 2018

The optimization procedure tries to minimize the area between the *secforc* curve in red and the black line that is the ideal curve because it is the maximum energy absorption obtainable considering the first peak of the *secforc* curve.

The optimization algorithm is NLPQLP that stands for sequential quadratic programming and use a direct numerical technique, a gradient-based method called also steepest descent to find a minimum in a function. This algorithm is well-suited for non-linear design spaces as in this case study and it's also suitable for long-running simulations.

The most important features of this NLPQLP are:

- Uses the area around the initial design point;
- Finds quickly the local optimum point;
- It directly manages inequality and equality constraints.

Here are proposed the results of the optimization process for each running cycle in the form of table and history from the Isight output. The optimal result is quickly found only at the eighth cycle.

Run	D_Dimension	H_Dimension	Sum_DifUnderTarget_Simulation1_Target1	Design Feasibility
1	0	0	1750877,57	9
2	1	0	1725205,30	9
3	0	1	1868370,75	7
4	10	-10	2162698,48	7
5	4	-4	1900399,30	7
6	5	-4	1919333,92	7
7	4	-3	1877847,83	7
8	1	0	1725205,30	8

Table 8 – Optimization results

Source: Author's own work, 2018

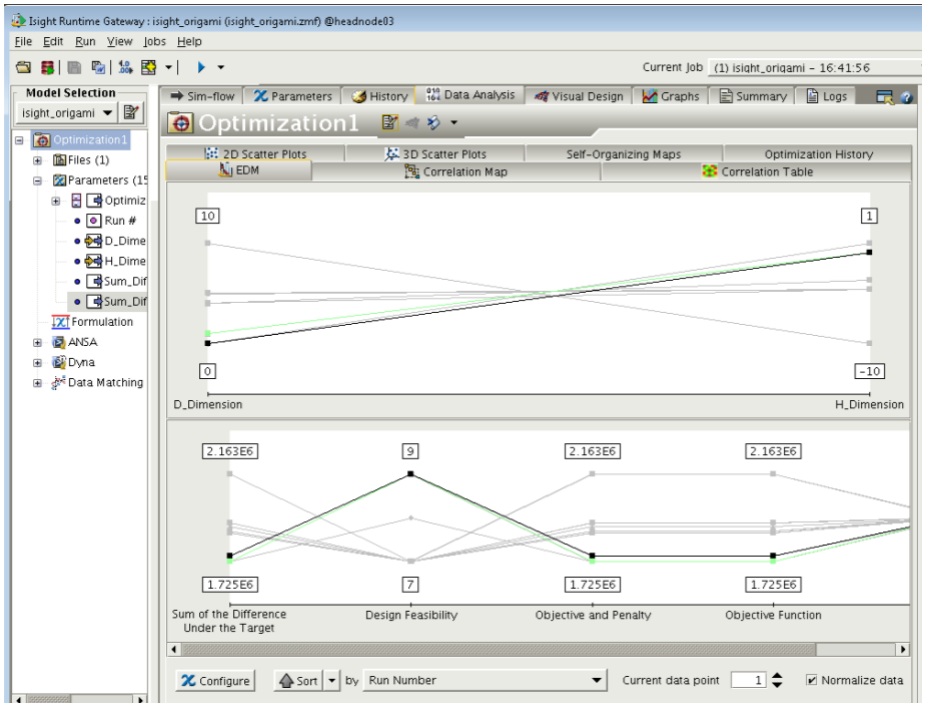

Figure 92 – Optimization history

Source: Author's own work, 2018

This optimization method starts from the local area around the initial design point, manages inequality and equality constraints independently, and allows to obtain a local optimum design in a fast way and staying within the limits imposed by the design feasibility.

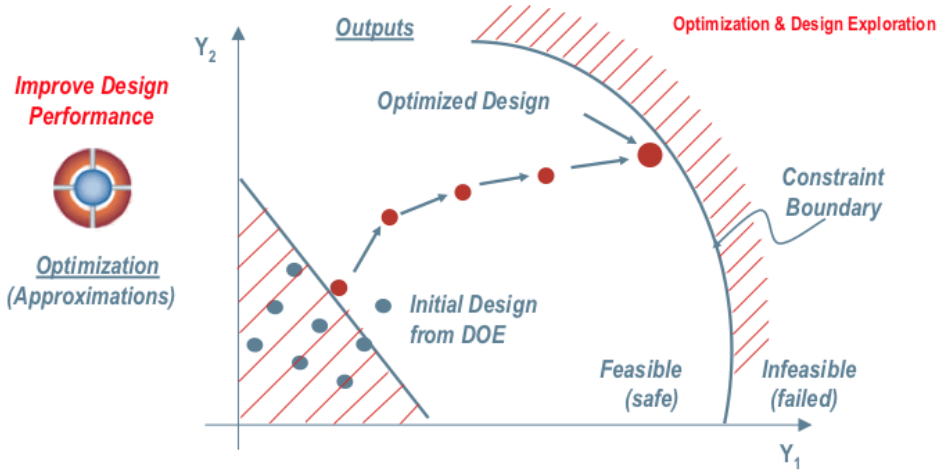

Figure 93 – Optimization method

Source: Author's own work, 2018

Finally, in *Figure 94* is possible to see the response surface of the area between the secforc and the target curve considering the variation of width (D) and height (H).

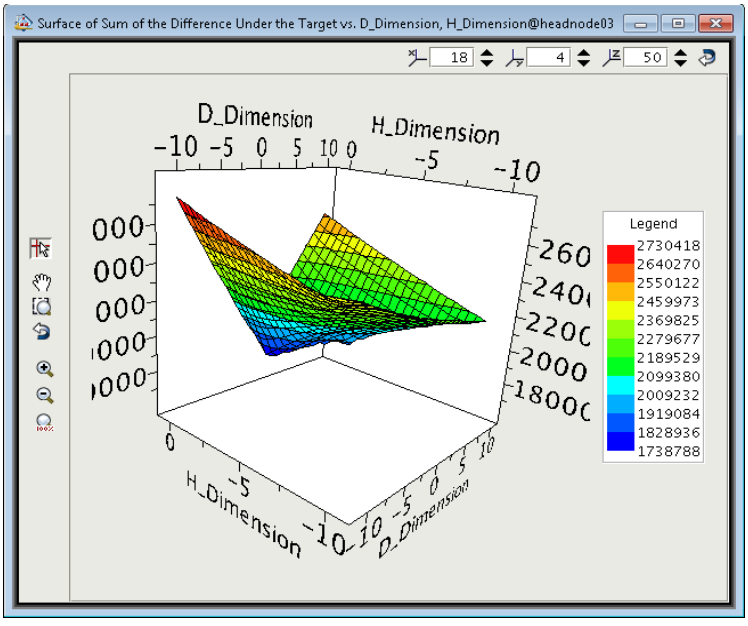

Figure 94 – Behavior of area difference depending on H and D variables

Source: Author's own work, 2018

Optimization Results

Started on Mon Mar 12 16:42:12 BRT 2018

Optimization Technique:	NLPQLP
Failed Run Objective Value	= 1.0E30
Failed Run Penalty Value	= 1.0E30
Gradient Points	= 1
Max Failed Runs	= 5
Max Iterations	= 2
Min Abs Step Size	= 1.0E-4
Rel Step Size	= 0.001
Save Technique Log	= false
Termination Accuracy	= 1.0E-6

Starting design point:

D_Dimension = 0.0 [-10.0;-9.0;-8.0;-7.0;-6.0;-5.0;-4.0;-3.0;-2.0;-1.0;0.0;1.0;2.0;3.0;4.0;5.0;6.0;7.0;8.0;9.0;10.0]
H_Dimension = 0.0 [-10.0;-9.0;-8.0;-7.0;-6.0;-5.0;-4.0;-3.0;-2.0;-1.0;0.0;1.0;2.0;3.0;4.0;5.0;6.0;7.0;8.0;9.0;10.0]

Completed on Tue Mar 13 01:20:42 BRT 2018

Total design evaluations:	8
Number of feasible designs:	8

Optimum design point:

Run #	= 2
Objective	= 1725205.298738411
Penalty	= 0.0
ObjectiveAndPenalty	= 1725205.298738411
D_Dimension	= 1.0
H_Dimension	= 0.0
Sum_DifUnderTarget_Simulation1_Target1	= 1725205.298738411

Figure 95 – Optimization summary

Source: Author's own work, 2018

In the figure above is proposed the summary of the optimization analysis. The result of an optimal geometry is with *c* value of 41mm instead of 45 mm and so the angle 2θ change from 156º to 158º and in conclusion the total height grows by 1 mm.

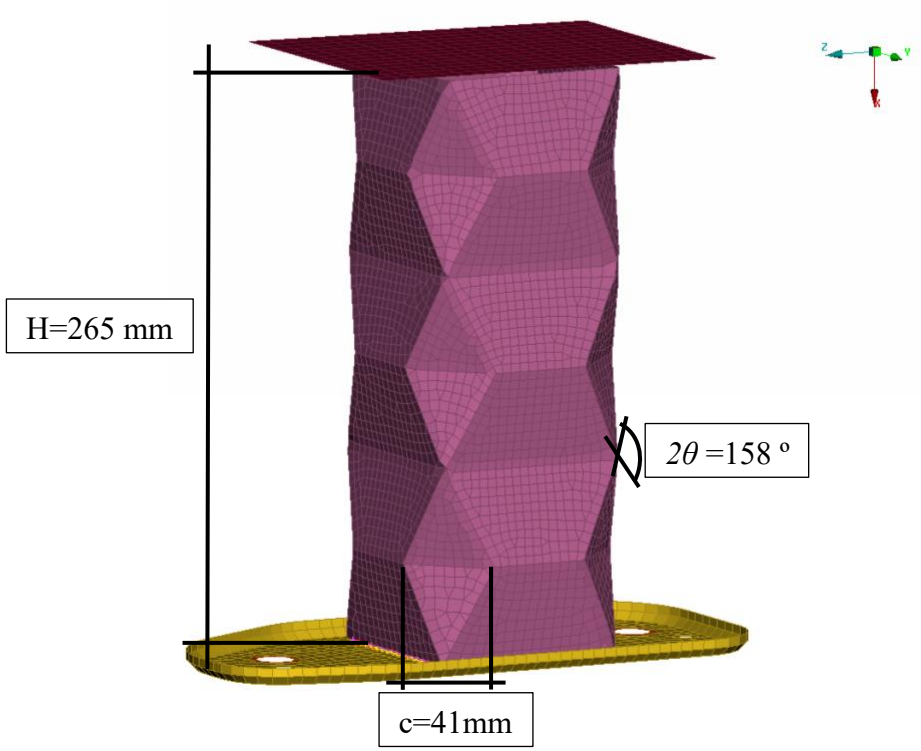

Figure 96 – Optimal geometry

Source: Author's own work, 2018

The *Figure 97* shows the curve comparison between the optimal geometry presented above and the first geometry with the parameters presented in the *Table 3*. It's easy to see that there is a larger part of the area under the blue curve compared to the red curve which represents the first geometry studied.

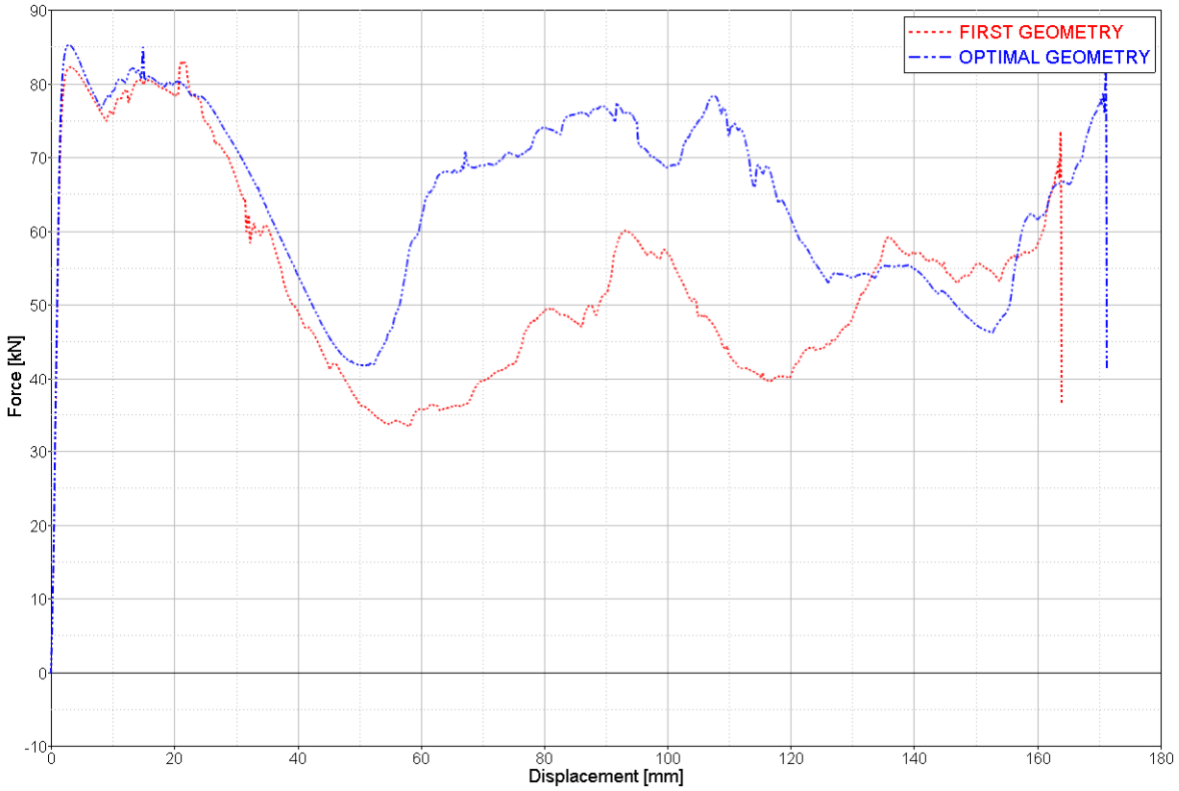

Figure 97 – Curve comparison with the optimal geometry

Source: Author's own work, 2018

	Pmean [KN]	Pmax [KN]	Energy absorption [J]
FIRST GEOMETRY	52	83	8655
OPTIMAL GEOMETRY	63,3	85	10489
	21,7% MORE		21,2% MORE

Table 9 – Comparison with the optimal geometry

Source: Author's own work, 2018

The results displayed in *Table 9* are in agreement with the curves and with a little increment of the P_{max} that is acceptable, reducing the lobe with until 41 mm it involves a high increase in the mean force and in the energy absorbed by the crash can.

This optimal geometry wasn't used in the experimental test because the implementation of the optimization procedure took a lot of time and also the prototype construction is a long process and therefore it was chosen the best geometry according to the other studies [57], [59].

6 – CONCLUSION

After this work, the great potential of this origami geometry has been proven and the results obtained allow to reduce the thickness or using a cheaper material as the FEE340, achieving also an increase in absorbed energy up to twice time compared with a general crash box that can be found on the market. The weight and the material reduction are an important piece in the component optimization because first of all allow to save money by using less raw material and then, limiting the crash box's size, the designers can have more freedom in making bumper or in creating even smaller and compact front frames. In this work was studied first the comparison of energy absorption between a general crash box and an origami one with more or less the same geometry property and then going down with the thickness of origami crash can has been found a solution which respects the same constraints.

Subsequently an experimental analysis with quasi-static crushing test was carried out first on the general crash box just to validate the numerical model and then on the origami crash box. Except for two specimens that collapsed probably due to a non-uniform welding in the both sides, the other results are quite close to the simulation especially regarding absorbed energy. With respect to the behavior during the compression, the deformation of five specimens is the diamond mode in which each lobe performs well; there was only a slight extra torsional deformation due to the superficial friction between the crash box and the plate connected to the compression machine actuator.

This experimental analysis was performed considering the best origami geometry according to the studies done so far, but after that was implemented an optimization algorithm in order to find an optimal solution. The procedure modifies the crash box geometry changing the fundamental parameters like the height l and the lobe width c and as a consequence of these factors the inclination angle θ. The optimal result allows to obtain a more constant curve shifting upward the valley in the force-displacement diagram and so increasing the crush force efficiency due to a better deformation mode during the crushing.

The future job suggestion in this field of study are many, for example increase the number of sides and, doing this, the cross section will be more similar to a circular tube. The idea behind

this development is that a circular crash box has a better symmetric collapse and can absorb more energy than a square tube. Remaining at this square geometry that is easier to implement on a physical specimen, it should be first verified with an experimental test if the optimal geometry obtained is really the best and then it should be improved the optimization process in particular if there is a need to change the number of modules. The geometry morph can change the height and the width of each module but with this procedure the crash box remains necessarily made up of three modules. For an automotive company, the best solution would be to set a certain height available to install the crash box as a constraint and then find the optimal geometry which can be with three modules but also in greater or smaller number.

Finally, another important step before this new origami technology can actually be used is a dynamic impact test with a drop tower in order to understand if the specimen deforms in a regular way with a folding pattern comparable with the one found in the quasi-static tests and also if the welded bonds don't fail when subjected to a high impact force.

REFERENCES

[1] Abramowicz A. S. 2016. **Design for axial crushing.** Impact Design Europe.

[2] Abramowicz W., Jones N. 1984. **Dynamic axial crushing of square tubes.** International Journal of Impact Engineering; 2(2): 179–208.

[3] Abramowicz W., Jones N. 1986. **Dynamic progressive buckling of circular and square tubes.** International Journal of Impact Engineering;4(4): 243–70.

[4] Abramowicz W. 1983. **Effective crushing distance in axially compressed thin-walled metal columns.** International Journal of Impact Engineering.

[5] **Advanced contact & bolt pretension 6.0.** Ansys training manual, 2001.

[6] Abramowicz W., Wierzbicki T. 1988. **Axial crushing of foam-filled columns.** International Journal of Mechanical Sciences, 30(3-4), 263-271.

[7] Al Galib D., Limam A. 2004. **Experimental and numerical investigation of static and dynamic axial crushing of circular aluminum tubes.** Thin-Walled Structures.

[8] ArcelorMittal. 2017. **High strength low alloy (HSLA) steels for cold forming.**

[9] ASM International. 2004. **Tensile Testing, Second Edition.** www.asminternational.org.

[10] Attia M. S., Meguid S. A., Nouraei H. 2012. **Nonlinear finite element analysis of the crush behaviour of functionally graded foam-filled columns.** Finite Elements in Analysis and Design.

[11] Avalle M., Chiandussi G., Belingardi G. 2002. **Design optimization by response surface methodology: application to crashworthiness design of vehicle structures.** Struct Multidisc Optim 24, 325–332. Springer-Verlag.

[12] Belingardi G., Avalle M. 2004. **Advanced materials for automotive applications.** Mobility and Vehicle Mechanics. Politecnico di Torino.

[13] Belingardi G., Goglio L., Rossetto M. 2005. **Impact behavior of bonded built-up beams: experimental results.** International Journal of Adhesion & Adhesives 25 173–180.

[14] Belingardi G., Avalle M., Vadori R., Drazetic P., Markiewicz E. 1994. **Analysis of the collapse modes in the axial crushing of multi-cell prismatic tubes.** Politecnico di Torino and Université de Valenciennes.

[15] Callister W.D. 2001. **Fundamentals of Materials Science and Engineering.** The University of Utah. John Wiley & Sons, Inc.

[16] Chen W. W., Song B. 2010. **Split Hopkinson (Kolsky) bar: design, testing and applications.** Springer Science.

[17] Cowper G. R., Symonds P. S. 1957. **Strain hardening and strain-rate effects in the impact loading of cantilever beams.** Brown University Division of Applied Mathematics Report No. 28.

[18] **Creating a global market for vehicle safety. Activity of New Car Assessment Programmes and how they operate in different countries and regions.** http://www.globalncap.org/.

[19] Dassault Systèmes. 2009. **Isight getting started guide.**

[20] Dassault Systèmes. 2011. **Abaqus 6.11 Getting started with Abaqus: Interactive edition.**

[21] Davies A. 2015. **Using Explicit Simulations to Go Further.** http://www.ansys-blog.com/using-explicit-simulations-to-go-further/.

[22] Deiter E. G. 1988. **Mechanical metallurgy.** University of Maryland. McGraw-Hill Book Company (UK) Limited.

[23] DiPaolo, B. P., TOM, J. G. 2006. **A study on an axial crush configuration response of thin-wall, steel box components: The quasi-static experiments.** International journal of solids and structures.

[24] Du Bois P., Chou C., Fileta B. F., Khalil T., Mahmood H. F., Mertz H., Wismans J. 2000. **Vehicle crashworthiness and occupant protection.** American Iron and Steel Institute Southfield, Michigan.

[25] Hallquist J. O. 2006. **LS-DYNA Theory manual.** Livermore software technology corporation.

[26] Hanssen A. G. 1999. **Static crushing of square aluminium extrusions with aluminium foam filler.** International Journal of Mechanical Sciences.

[27] Haufe1 A., Schweizerhof k., DuBois P. 2013. **Properties & Limits: Review of Shell Element Formulations.** Developer forum.

[28] Hesami F. 2001. **First vehicle Platform project on 2001.** LinkedIn SlideShare.

[29] Hosford W. F. 2005. **Mechanical Behavior of Materials.** University of Michigan. Cambridge

[30] Jiayao Ma, Zhong You. 2013. **Energy absorption of thin-walled beams with a pre-folded origami pattern.** Department of Engineering Science, University of Oxford.

[31] Jones N. 1989. **Structural impact.** Cambridge University.

[32] Krabbenhøft K. 2002. **Basic computational plasticity.** Department of Civil Engineering. Technical University of Denmark.

[33] Kumar S. 2008. **A numerical study on the axial crush characteristics of thin walled rectangular tubes subjected to dynamic impact.** SAE international.

[34] Kuribayashi K., Tsuchiya K., You Z., Tomusb D., Umemotob M., Ito T., Sasaki M. 2006. **Self-deployable origami stent grafts as a biomedical application of Ni-rich TiNi shape memory alloy foil.** Materials Science and Engineering A 419 131–137.

[35] Langseth M. 1999. **Crashworthiness of aluminium extrusions: validation of numerical simulation, effect of mass ratio and impact velocity.** International Journal of Impact Engineering.

[36] **LS-DYNA Keyword user's manual Volume I. LS-DYNA Keyword user's manual Volume II.** Livermore software technology corporation (LSTC), 2015.

[37] Mamalis A.G. 2008. **The effect of the implementation of circular holes as crush initiators to the crushing characteristics of mild steel square tubes: experimental and numerical simulation.** National Technical University of Athens.

[38] Marko Vrh. 2016. **Isight – parametric optimization and automation.** SIMULIA seminar.

[39] Matteis P. 2017. Dispense del corso di "**Materiali per l'industria meccanica**". Corso di Laurea magistrale in Ingegneria Meccanica. Politecnico di Torino.

[40] Morello L., Rossini L., Pia G., Tonoli A. 2011. **The Automotive Body. Volume I: Components Design** and **The Automotive Body. Volume II: System Design.** Springer.

[41] Optibody project 2012. **Guideline on optimal architectures for crashworthiness and compatibility improvement.** Politecnico di Torino.

[42] Peroni L., Avalle M., Belingardi G. 2006. **Experimental investigation of the energy absorption capability of continuous joined crash boxes.** Paper Number 07-0350. Politecnico di Torino.

[43] Rcar.org. 2011. **RCAR Low-speed structural crash test protocol**.

[44] Redhe M., Nilsson L., Bergman F., Stander N. 2005. **Shape Optimization of a Vehicle Crash-box using LS-OPT.** 5th European LS-DYNA Users Conference**.**

[45] Reid S. R., Reddy T. Y. 1986. **Axial crushing of foam-filled tapered sheet metal tubes.** Int. J. Mech.Sci.28,643-656.

[46] Rossi A. 2005. **Numerical simulation of the axial collapse of thin-walled polygonal section tubes.** Thin-Walled Structures.

[47] Singace A.A., El-Sobky H. 1997. **Behaviour of axially crushed corrugated tubes.** International Journal of Mechanical Sciences.

[48] Song J., Chen Y., Lu G. 2012. **Axial crushing of thin-walled structures with origami patterns.** Thin-walled structures.

[49] Tarlochan F. 2013. **Design of thin wall structures for energy absorption applications: Enhancement of crashworthiness due to axial and oblique impact forces.** Thin-Walled Structures.

[50] Tarnai T. 1994. **Folding of uniform plane tesselations.** Origami Science & Art, Proceedings of the Second International Meeting of Origami Science and Scientific Origami.

[51] Tasdemirci A. 2008. **The effect of tube end constraining on the axial crushing behavior of an aluminum tube.** Izmir Institute of Technology.

[52] Tolman S.S., Delimont I., Howell L.L., Fullwood D.T. 2014. **Material selection for elastic energy absorption in origami-inspired compliant corrugations.** Smart Materials and Structures.

[53] Van der Velden A., Koch P. **Isight Design Optimization Methodologies.** SIMULIA *www.asminternational.org*

[54] Wu W., You Z. 2011. **A solution for folding rigid tall shopping bags.** Proceedings of the royal society.

[55] www.dynasupport.com/

[56] Zhang X., Cheng G., You Z., Zhang H. 2007. **Energy absorption of axially compressed thin-walled square tubes with patterns.** Thin-Walled Struct. 45 737–746.

[57] Zhang X., Hoon H. 2009. "**Energy absorption of longitudinally grooved square tubes under axial Compression.** Korea Advanced Institute of Science and Technology.

[58] Zhao X., Hu Y., Hagiwara I. 2011. **Shape optimization to improve energy absorption ability of cylindrical thin-walled origami structure.** Journal of Computational Science and Technology.

[59] Zhou C., Wang B., Ma J., You Z. 2016. **Dynamic axial crushing of origami crash boxes.** International Journal of Mechanical Sciences.

[60] Zhou C., Zhou Y, Wang B. 2017. **Crashworthiness design for trapezoid origami crash boxes.** Thin-Walled Structures 117 257–267. University press.

[61] Zhou C. H., Wang B., Luo H. Z., Chen Y. W., Zeng Q. H., Zhu S. Y. 2017. **Quasi-Static Axial Compression of Origami Crash Boxes.** International Journal of Applied Mechanics.